

UNIVERSITY OF CALIFORNIA

Los Angeles

Design of a Highly Dynamic Humanoid Robot

A dissertation submitted in partial satisfaction
of the requirements for the degree

Doctor of Philosophy in Mechanical Engineering

by

Taoyuanmin Zhu

2023

© Copyright by
Taoyuanmin Zhu
2023

ABSTRACT OF THE DISSERTATION

Design of a Highly Dynamic Humanoid Robot

by

Taoyuanmin Zhu

Doctor of Philosophy in Mechanical Engineering

University of California, Los Angeles, 2023

Professor Dennis W. Hong, Chair

For the past decades, humanoid robots have demonstrated increasingly impressive capabilities. However, the limitations of current generation of robots became painfully clear during the DARPA Robotics Challenge. They struggled with even basic locomotion under real-world conditions, a far cry from what was expected from the public. This study attempts to design a brand-new humanoid platform from ground up.

Custom-designed proprioceptive actuators paired with liquid cooling are designed to maximize the torque density of the robot. The kinematics chain and structural parts of the robot are optimized for fast walking and running. Purpose-built sensors and electronics aim to provide robust feedback under impact load.

Combined with new control architecture, the robot achieved untethered running as well as walking at over 2m/s. We demonstrated highly dynamic behaviors that are beyond the state-of-art and pushed locomotion capabilities one step closer to their human counterpart.

The dissertation of Taoyuanmin Zhu is approved.

Tsu-Chin Tsao

Veronica Santos

Jun Chen

Dennis W. Hong, Committee Chair

University of California, Los Angeles

2023

TABLE OF CONTENTS

List of Figures	vi
List of Tables	ix
Acknowledgments	x
Curriculum Vitae	xi
1 Introduction	1
1.1 Motivation	1
1.2 Background	2
1.2.1 Actuator Design for Legged Robots	2
1.2.2 Cooling	5
1.2.3 Humanoid Design	7
1.3 Research Objectives	9
2 Actuator Design	11
2.1 Rotor and Stator Design	11
2.2 Gearbox and Packaging	15
2.3 Driver Electronics Design	17
2.4 Embedded Control Structure	19
2.5 Actuator Cooling	20
2.6 Actuator Variants	26
3 Mechanical Design	27

3.1	Lower Body Kinematics and Structure	27
3.2	Torso Structure	38
3.3	Arm Design	41
3.4	Head Design	44
4	System Design	46
4.1	Sensors	46
4.1.1	Cameras	47
4.1.2	Inertial Measurement Unit	47
4.1.3	Foot Sensor	50
4.2	Computer	53
4.3	Electronics	54
4.3.1	Battery	54
4.3.2	Wireless E-Stop	57
4.3.3	DC-DC Converter	59
4.3.4	USB to RS-485 Adapter	59
5	Testing and Results	62
5.1	Parts Manufacturing	62
5.2	Assembly and Robot Bring-up	65
5.3	Results	66
6	Conclusion and Future Work	74
6.1	Conclusions	74
6.2	Limitations and Future Research	76
	Bibliography	79

LIST OF FIGURES

1.1	Strain wave gears and force torque sensor.	3
1.2	Actuation methods compared.	5
1.3	Cooling methods illustrated.	6
1.4	A library of humanoid robots.[40, 8, 3, 19, 15, 17, 36, 25, 28, 9, 13, 44]	10
2.1	Peak torque density comparison.	13
2.2	Prototype actuator rotor and stator.	14
2.3	Prototype actuator rotor and stator.	14
2.4	Prototype actuator torque test result.	15
2.5	Drive and back-driven torque comparison.	16
2.6	Prototype actuator gearbox.	17
2.7	Custom motor driver PCB.	18
2.8	Motor driver functional diagram.	19
2.9	Motor driver control loop diagram.	20
2.10	Compensated cogging torque compared to uncompensated cogging torque.	20
2.11	Early prototype actuator with liquid cooling.	21
2.12	Lumped mass model of liquid cooling system.	22
2.13	Actuator torque density with respect to duration.	23
2.14	Section view of prototype immersion cooling.	24
2.15	Different cooling method actuator torque density comparison.	25
3.1	Human lower body joints and spring-loaded inverted pendulum model.	27
3.2	Lower body joints.	28

3.3	Lower body joints and actuator locations.	29
3.4	Hip pitch range of motion.	30
3.5	Lower body range of motion in different poses.	31
3.6	Mass distribution of the lower body.	32
3.7	Knee linkage within the femur structure.	33
3.8	Linkage force with varying knee joint position.	34
3.9	Linkage buckling condition.	34
3.10	THOR RD with dynamixel actuator modules.	36
3.11	Lower body structures.	37
3.12	Structure topology optimization procedure.	38
3.13	Torso structure and components.	39
3.14	Torso internal cooling air flow.	40
3.15	Battery cage within the torso structure.	41
3.16	Torso to pelvis mating features.	42
3.17	upper body joints and actuator locations.	43
3.18	Cross section of arm structures.	44
3.19	Head joints and actuator locations.	45
4.1	Cameras used on ARTEMIS.	47
4.2	Camera field of view.	49
4.3	Microstrain IMUs.	49
4.4	IMU data comparison.	51
4.5	Foot with custom sensor.	52
4.6	Foot sensor analysis and assembly.	52
4.7	Alternative computer options.	53

4.8	Custom RB56100 lithium battery.	55
4.9	Custom SMBus compliant battery charger.	56
4.10	Battery charging current based on SoC and temperature.	57
4.11	Wireless E-Stop system.	58
4.12	DC-DC Converter.	59
4.13	Custom USB to RS-485 converter.	60
4.14	USB round trip latency comparison.	61
5.1	Machining equipment used for manufacturing.	62
5.2	Parts being machined in CNC mill.	63
5.3	Femur structure machining sequence.	64
5.4	Machined parts for lower body structure.	65
5.5	Assembled actuators.	66
5.6	ARTEMIS lower body on gantry.	67
5.7	ARTEMIS with padding fitted.	67
5.8	ARTEMIS walking sequence.	68
5.9	Joint position, velocity and torque during walking.	69
5.10	Foot contact sensor reading during walking.	70
5.11	Center of Mass Height, velocity and joint torque during running.	71
5.12	ARTEMIS kicked and recovery sequence.	71
5.13	ARTEMIS walking on Engineering IV 3rd floor.	72
5.14	ARTEMIS untethered outdoor walking.	73
5.15	ARTEMIS untethered walking on grass.	73
6.1	Depth data extracted from stereo image reconstructing the environment.	77
6.2	ARTEMIS in soccer kicking pose.	78

LIST OF TABLES

1.1	Comparison of Actuator Designs	4
2.1	Custom Motor Specification	13
2.2	Notations for liquid cooling thermal model.	22
2.3	Torque density with the different cooling approaches.	25
2.4	Actuator Specifications	26
3.1	Lower Body Joints Specifications	29
3.2	Robot weight distribution comparison	32
3.3	Knee linkage buckling analysis	35
3.4	Arm Joints Specifications	43
4.1	ARTEMIS Robot Specification	46
4.2	Stereolabs ZED 2 camera specifications	48
4.3	Intel RealSense D435i camera specifications	48
4.4	IMU Specification Comparison	50
4.5	Computer Specification Comparison	54
4.6	Battery module Specification	56

ACKNOWLEDGMENTS

I would like to express my sincere gratitude to all those who have supported me throughout my PhD journey.

First and foremost, I am deeply grateful to my advisor, Dr. Dennis Hong, for his invaluable guidance, mentorship, and unwavering support. Research project as ambitious as such would not have been possible in literally any other laboratory.

I would also like to extend my heartfelt appreciation to my committee members, Prof. Tsu-Chin Tsao, Prof. Veronica Santos and Prof. Jun Chen, for their valuable input and feedback throughout the course of my research. Their insights and suggestions have been invaluable in shaping my research.

I am also grateful to all my colleagues and friends at Robotics and Mechanisms Laboratory. This project has been truly a team effort, and it has been my honor and pleasure to work alongside some of the most brilliant and genuine people I have ever met.

Finally, I would like to acknowledge my family and friends for their love, encouragement, and sacrifices throughout my academic journey, and especially during the pandemic.

Thank you all for your support, encouragement, and guidance along the way.

CURRICULUM VITAE

2011 – 2015	B.E. in Mechanical Engineering, Tsinghua University, Beijing, China.
2015 – 2018	M.S. in Mechanical Engineering, University of California, Los Angeles (UCLA).
2018 – Present	Ph.D. student in Mechanical Engineering, University of California, Los Angeles (UCLA).

PUBLICATIONS

Xuan Lin, Gabriel I. Fernandez, Yeting Liu, Taoyuanmin Zhu, Yuki Shirai, and Dennis Hong, “Multi-Modal Multi-Agent Optimization for LIMMS, A Modular Robotics Approach to Delivery Automation,” In *2022 IEEE/RSJ International Conference on Intelligent Robots and Systems (IROS)*, 2022.

Taoyuanmin Zhu, Gabriel I. Fernandez, Colin Togashi, Yeting Liu, and Dennis Hong, “Feasibility study of limms, a multi-agent modular robotic delivery system with various locomotion and manipulation modes,” In *2022 19th International Conference on Ubiquitous Robots (UR)*, 2022.

Yeting Liu, Junjie Shen, Jingwen Zhang, Xiaoguang Zhang, Taoyuanmin Zhu, and Dennis Hong, “Design and control of a miniature bipedal robot with proprioceptive actuation for dynamic behaviors,” In *2022 39th IEEE International Conference on Robotics and Automation (ICRA)*, 2022.

Taoyuanmin Zhu, Min Sung Ahn, and Dennis Hong, “Design and experimental study of

bldc motor immersion cooling for legged robots,” In *2021 20th International Conference on Advanced Robotics (ICAR)*, pages 1137–1143, 2021.

Joshua Hooks, Min Sung Ahn, Jeffrey Yu, Xiaoguang Zhang, Taoyuanmin Zhu, Hosik Chae, and Dennis Hong, “Alphred: A multi-modal operations quadruped robot for package delivery applications,” *IEEE Robotics and Automation Letters*, 5(4):5409–5416, 2020.

Xiaoguang Zhang, Taoyuanmin Zhu, Itsui Yamayoshi, and Dennis Hong, “Dexterity, sensitivity and versatility: An under actuated robotic hand with mechanical intelligence and proprioceptive actuation,” *International Journal of Humanoid Robotics*, 17(02):2050006, 2020.

Donghun Noh, Yeting Liu, Fadi Rafeedi, Hyunwoo Nam, Kyle Gillespie, June-sup Yi, Taoyuanmin Zhu, Qing Xu, and Dennis Hong, “Minimal degree of freedom dual-arm manipulation platform with coupling body joint for diverse cooking tasks,” In *2020 17th International Conference on Ubiquitous Robots (UR)*, pages 225–232, 2020.

Taoyuanmin Zhu, Joshua Hooks, and Dennis Hong, “Design, modeling, and analysis of a liquid cooled proprioceptive actuator for legged robots,” In *2019 IEEE/ASME International Conference on Advanced Intelligent Mechatronics (AIM)*, pages 36–43, 2019.

Xiaoguang Zhang, Taoyuanmin Zhu, Itsui Yamayoshi, and Dennis Hong, “A force controlled under actuated robotic hand with mechanical intelligence and proprioceptive compliant actuation,” In *2018 IEEE-RAS 18th International Conference on Humanoid Robots (Humanoids)*, pages 1–8, 2018.

CHAPTER 1

Introduction

1.1 Motivation

People have long dreamed of having robots as a ubiquitous part of the modern society. A general-purpose robot that alleviates human from the dull, dirty, and dangerous, it is seen to some as the ultimate goal for the field of Robotics. From robotic arms on the assembly line to the delivery drones that roam the sky, for the past decades, purpose-built robots have revolutionized industries and brought tremendous amount of convenience to our lives. Yet a robot that is multi-purpose and can aid our day-to-day lives is still absent.

What form would a robot take to best serve our daily lives? One would argue that since the infrastructures around us are all built for human, it is conceivable that a helper robot should be in a humanoid form. That appears to be the strategy taken by most teams during the DARPA Robotics Challenge, which was a competition held in the wake of the 2011 Fukushima nuclear power plant disaster [26, 43]. During the competition, the robots are asked to complete a series of tasks that are typical for disaster relief situation such as driving a vehicle, opening a door, climbing stairs, connecting fire hose and turning on a valve. Being a humanoid allows the robots to be able to traverse environment that are designed for human and operate equipment and tools effectively.

DARPA Robotics Challenge showed the world the potential of humanoid robots. However, at the same time, it demonstrated the shortcomings of what was considered to be the state-of-art of Robotics [11, 6]. The robots were struggling with seemingly trivial tasks such as walking without constantly falling over. The robots were painfully slow, taking a few steps forward would take minutes to complete. The robots were fragile, falling over would

often mean the end of the run and required thousands of dollars in repair. It became clear that the robots were far from ready to be part of our daily lives.

Dissecting the challenges of developing a humanoid robot, locomotion, manipulation, as well as higher level perception and planning are all far from its human counterpart. Through millions of years of evolution, we make walking and running seem trivial, whereas in fact, they are of enormous challenge to the robots. Take biological muscles as an example, they exceed the best robotic actuator ever conceived. They have incredible force density while being extremely compliant when necessary. They have embedded force sensing capability and are incredibly resilient. On top of that, the pressure sensing from the feet and motion sensing from inner ear vestibular system make walking seem effortless.

For the motivation, we seek to develop a robotic platform that is one step closer to us human in terms of locomotion capabilities. Naturally, hardware platform needs to be developed in conjunction with corresponding control strategies, which will be addressed in concurrent work. It is the author's hope that this work will serve as a first step towards the next generation of humanoid robot.

1.2 Background

1.2.1 Actuator Design for Legged Robots

As described in previous section, having adequate actuation is a critical first step to building a successful robot platform. This is true not just for humanoid robots, but legged robots in general. In this section, different actuation paradigms are introduced and discussed.

1.2.1.1 High gear reduction + force torque sensor actuators

Following traditional robotic arms, an obvious way of improving the torque density of the actuator is to use higher gear reduction ratio. Strain wave gears, like harmonic drives are used extensively for its compactness and the unique benefit of no backlash. As more and

more sophisticated control algorithms are being implemented, force and torque controllability became critical to the actuators. Once again, the direct approach is to integrate torque sensors to the actuators and put force torque sensor (F/T sensor) at the end of each limb of the robot.

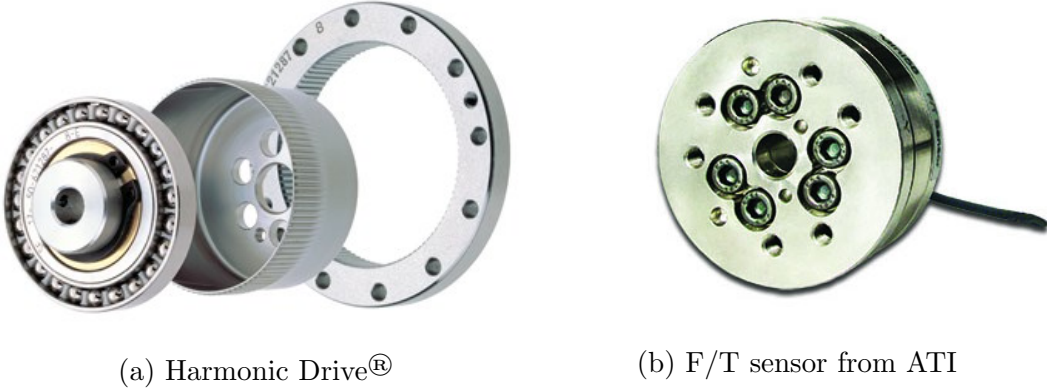


Figure 1.1: Strain wave gears and force torque sensor.

This approach has proven to be successful for a wide range of robots such as ASIMO[40], HRP series[18, 20, 19], HUBO series[33, 17], JAXON[24], SCHAFT[15]. With few exceptions, robots with high gear reduction can only achieve very slow and relatively static locomotion. This is due to the fact that harmonic drives and F/T sensors are fragile and highly susceptible to impacts. Adding to that, the high reflective inertia and low efficiency of the gearbox makes it impossible to absorb impact load, which happens every time the foot hit the ground.

1.2.1.2 Series elastic actuators

In an effort to reduce the impact load on the gearbox and drawing inspiration from biological muscle, series elastic actuator(SEA) puts an elastic element in between the gearbox and the load[34]. By measuring the deflection in the elastic element, force can be evaluated as a result. Such actuator gained popularity by solving the two major downside of the prior approach, i.e., force control and impact mitigation.

Robotic platforms with SEA can demonstrate natural, dynamic and energy efficient gait including ATRIAS[14], THOR[13], WALK-MAN[44]. However, SEA comes with a signifi-

cant tradeoff; the elastic spring affects the system dynamics and as a result, lower spring stiffness means low control bandwidth whereas higher spring stiffness results in poor impact mitigation [39]. Therefore, the spring stiffness often needs to be tailored to the joint being used. Additionally, it is known that in biology, effective leg stiffness actually changes with locomotion speed[5], making variable stiffness a potential requirement for dynamic locomotion.

1.2.1.3 Proprioceptive actuators

An alternative to achieving force control is to use motor current to estimate the torque output of the actuator. Current-based torque control cannot work with high reduction actuator due to the friction loss and other non-linearities of the gearbox, whereas direct drive motors would work exceptionally well. This is commonly referred to as the transmission transparency[22]. However, without the torque amplification, the torque density would suffer. Thus, it is proposed to use high-torque motor paired with high-efficiency low-reduction-ratio gearbox to produce reasonable torque density while maintaining transmission transparency[42]. An additional benefit of such design is that due to the low reflected inertia, the actuator can handle much higher impact and allow highly dynamic behaviors. Due to the current-based torque control nature of such direct drive and quasi-direct drive actuators, they are commonly referred to as proprioceptive actuators. This design approach was popularized in legged robots by MIT cheetah[41, 7] and mini cheetah[21].

Table 1.1: Comparison of Actuator Designs

	High reduction F/T sensor	SEA low stiffness	SEA high stiffness	Proprio- ceptive
Torque density	+++	++	++	+
Impact mitigation	-	+++	+	+++
Bandwidth	+++	+	++	+++
Torque control	+++	+++	+++	++

Hydraulic actuation is another effective method for humanoids, popularized by MIT leg lab and later Boston Dynamics[38, 37]. Hydraulic actuators have the unique benefit of extremely high force density at the actuator as well as direct force control via hydraulic pressure. However, the added system complexity of hydraulic pump, valve and hose, making it hard to scale up. A comparison of all previously mentioned approaches is shown in table 1.1.

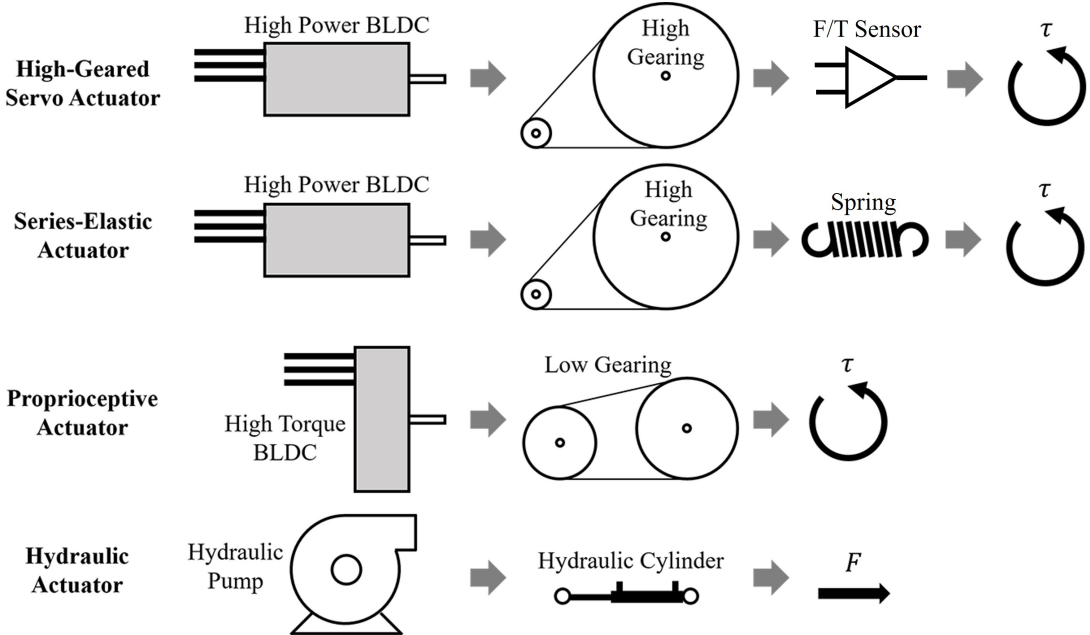


Figure 1.2: Actuation methods compared.

1.2.2 Cooling

Thermal management system is of great importance to legged platforms. In order to deliver high torque density, it is common to push motor way beyond the nominal operating conditions. The most common way of dissipating excessive has been forced air cooling. DRC-HUBO+, who won the DARPA Robotics Challenge made extensive comparison between still air, forced air cooling and liquid cooling. It settled with heatsink fin with blowing fan for its setup simplicity as opposed to liquid cooling, which was found to have 15% higher efficiency [17]. On the contrary, SCHAFT utilized liquid cooling for its hip and knee joints, which

required the highest average load [16, 45]. Similar liquid cooling approach have been taken by robots like JAXON and DRACO [24, 4, 23, 32]. In all cases, it is found that liquid cooling improves the torque output of the actuator and in turn allows lighter weight actuator to be used.

When considering cooling for proprioceptive actuators, it is accepted that due to the low reduction ratio, they generate more Joule heating when compared to other actuation approaches. This makes thermal management an even more important challenge.

A less common cooling method is to use evaporative cooling in much of the same way as us human. Robot Kengoro was designed with skeletal microstructure such that coolant can flow through and slowly evaporate [25]. It was found to have higher efficiency when compared to a liquid cooling system.

Another cooling approach, known as immersion cooling, lets the electrically non-conductive working fluid come in direct contact with the winding [35, 46]. Such design can be implemented as a wet stator design where sleeves or molded coolant passages are utilized to guide the coolant while keeping the rest of the motor dry [10, 27, 2].

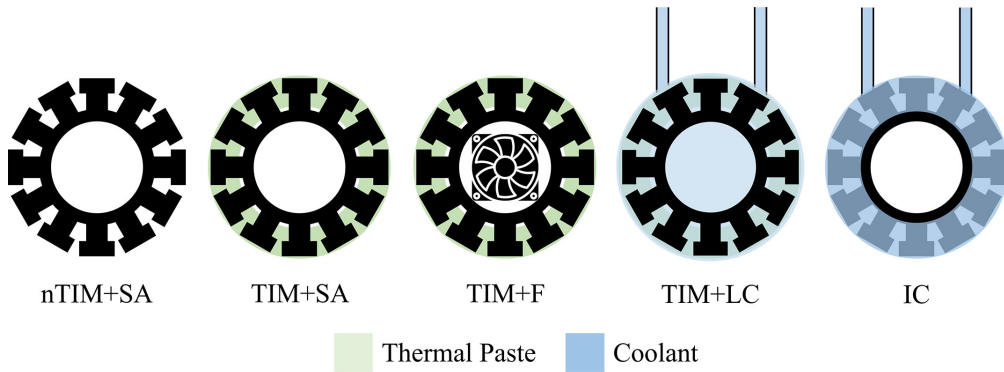


Figure 1.3: Cooling methods illustrated.

nTIM+SA: no thermal interface material, natural convection. TIM+SA: potting thermal compound, natural convection. TIM+F: potting thermal compound, forced air cooling. TIM+LC: potting thermal compound, liquid cooling. IC: immersion cooling.

1.2.3 Humanoid Design

1.2.3.1 Lower Body Kinematics Design

For humanoid robot design that is focused on locomotion, lower body becomes the main focus. To mimic human hip spherical joint, it is common to design a humanoid robot hip with three intersecting rotary joints [40, 17]. A typical configuration is to have the hip yaw as the proximal first joint. The benefit for such design is being able to package hip yaw motor up into the pelvis section of the robot. Tilted yaw joint have been explored for robot LOLA, which has its hip yaw joint inclined 15deg to the vertical axis for better power consumption [28]. Hip roll joint is often the middle joint, while hip pitch being the last joint of the three. As the last joint of the hip, which is also the joint typically requiring the most amount power, hip pitch actuator can be often packaged into the thigh and femur [15, 17, 19, 47].

The knee joint almost always has the highest power requirement of a given humanoid robot, since knee joint always have to fight gravity when standing. Designs incorporating parallel spring elements have been explored for better energy efficiency [29, 12]. While most robot knee joint uses single revolute joint, designs mirroring the human rolling contact knee have been explored for better knee range of motion.

For the ankle joint, a two degrees of freedom universal joint is often used to control the pitch and roll of the foot. The ankle joint provides the necessary range of motion for the foot to adapt to uneven terrain, as well as applying the necessary moment to maintain balance.

While different actuated and unactuated toe designs have been explored for more natural walking gait [28, 30], most existing humanoid robot uses rigid flat feet that are often rectangular in shape.

For the pelvis and torso joint, it ranges from no torso actuation to full three degrees of freedom. When there is no torso actuation, hip joints are used to control the body orientation. This comes at the cost where body motion will always have to be coupled with leg movements. It is a common practice to include torso yaw degree of freedom since it greatly expands the workspace of the arms, making manipulation task easier [17]. Torso

pitch actuation is typically done when the hip pitch joint does not have enough range of motion for the robot to squat down [47]. This is especially important if picking up objects from the ground is a required motion for the robot. Torso roll helps when it is required to keep robot in balance by shifting the upper body laterally. It can also help the swing foot to gain more ground clearance [31].

While directly mounting rotary actuators at the respective joint positions can be done, it is common for humanoid robot design to move actuators away from the joints due to various reasons. Typically, when three joints are designed to intersect, it is not possible to package all actuators without interference issue. Actuators also are often moved proximally towards the hip, reducing the leg inertia. This is beneficial for higher speed walking as well as energy efficiency.

One way of packaging actuators tightly together is to separate the motor rotor and stator with the reduction gearbox. Timing belts are used to transfer rotation from the motor rotor to the gearbox, which can be packaged right against the adjacent actuator, thus greatly improve the range of motion [15, 17, 19, 47].

Common types of transmission used to connect rotary actuator output to rotary joints are linkages, belts, chains and cables. Parallel four bar linkages are used often when the target range of motion is less than 180 degrees [13, 44]. When joint angles approaches singularity, linkage force rapidly increases as well as the backlash, making it infeasible. Belts are often used when range of motion of more than 180 degrees is required. Due to the relative low stiffness of the belts, it is uncommon to use belt after the gear reduction, chains are used instead for its higher stiffness. Cable driven actuators are used as high efficiency light weight alternative to gearbox but come at the cost of difficult cable routing and tensioning [29, 12].

In certain situations, linear actuators are preferred because they offer superior packaging options, and ball screws are both high-efficiency and easily accessible [13, 28, 36]. To transfer linear actuator stroke to joint rotation, four bar or six bar mechanism can be used. The change in transmission ratio at varying angle needs to be taken into account. Slider crank mechanism can be used if relative movement between the actuator and the structure is

undesirable.

Parallel mechanisms for the hip and knee actuation have been considered in an attempt to optimize leg mass[14]. However, the antagonistic work by the opposing actuators drastically decreased the efficiency compared to regular serial chain hip knee[1].

1.3 Research Objectives

In this work, It is my hope to develop a humanoid robot platform that is capable of dynamic locomotion behavior such as running and jumping. To accomplish this goal, the robot needs to be designed from ground up. High torque density, highly compliant actuators are developed to replace the traditional stiff, position-controlled actuators. Actuators are also required to have high overload capability as well as impact resistance. In addition, the lower-body kinematics chain and structure are optimized to minimize weight and minimize inertia of moving links when running. Furthermore, robust foot sensors are designed to withstand the repeated impact of running and jumping. In all, a holistic approach needs to be taken to designing the next-generation humanoid robot, and to be one step closer to the ultimate goal of a general-purpose humanoid robot that matches or exceeds human capabilities.



Figure 1.4: A library of humanoid robots.[40, 8, 3, 19, 15, 17, 36, 25, 28, 9, 13, 44]

CHAPTER 2

Actuator Design

Actuator is the most critical part of achieving dynamic motions. Proprioceptive actuators are designed from the ground up to provide the power and torque density that is critical to legged locomotion. The low reflected inertia and high transmission transparency enables the robot to utilize proprioceptive force control and be resilient to impact when running and jumping.

In this chapter, the actuator design is described starting from the rotor and stator geometry design. Depending on the reduction ratio required, appropriate gear train is designed. To enable modular actuator design, custom driver electronics is designed to be integrated as part of the actuator module and the low-level embedded controller is explained.

2.1 Rotor and Stator Design

For most commercially available motors, emphasis has been put on high efficiency at speed. This is valid for electric vehicles or even traditional pick-and-place robotic arms. However, for legged robots, the motor operates mostly in low-speed region and often needs peak torque that is over 4 times the average torque. When analyzing off-the-shelf motors, stator magnetic saturation often limits the instantaneous torque output of the motor. As a result, custom rotor and stator needs to be designed and optimized for its peak torque capability.

As often pointed out in literature, motor torque τ is proportional to the air gap radius r_g^2 and is linearly proportional to the length of the motor stack l_s . Whereas the weight of the motor M linearly scales with both air gap radius and stack length.

$$\tau \propto r_g^2 \quad (2.1)$$

$$\tau \propto l_s \quad (2.2)$$

$$M \propto r_g \quad (2.3)$$

$$M \propto l_s \quad (2.4)$$

A critical part of the analysis that is often ignored is that in order for motor weight to scale linearly with air gap radius, the radial thickness of the motor needs to stay constant. As a result, the number of magnet poles N_m needs to scale with the motor size as well. This became obvious when we consider the relationship between motor torque and air gap magnetic shear force.

$$\tau = 2N_m N B_g l_s r_g i \quad (2.5)$$

Where, N is the number of turns and i is current. B_g is the air gap flux density.

The torque production efficiency in terms of motor constant K_m can be expressed as follows.

$$K_m = \frac{\tau}{\sqrt{i^2 N_m R_{slot}}} = B_g r_g \sqrt{l_s N_m A_{wb} / \rho} \quad (2.6)$$

A_{wb} is the bare wire cross-sectional area. ρ is the resistivity of the winding.

Another part of the actuator design analysis is to determine the desired reduction ratio. Suppose a hypothetical actuator with a traditional motor and a gear reduction of 128:1. By increasing the air gap radius 4 times, the required gear reduction is reduced to 8:1. The resulting actuator would have identical peak torque and reflected inertia, however, a gearbox with reduction ratio of 8:1 would have much higher efficiency and transparency compared to a gearbox of 128:1.

To conclude, for designing proprioceptive actuators that maximizes peak torque production, air gap radius should be set as large as permissible. To maintain torque density, pole

count should be increased accordingly. With this design philosophy, a motor with an air gap radius of 90mm has been designed for the hip pitch and knee pitch actuation. The motor has an outer-runner design to maximize air gap radius and has 40 pole pairs.

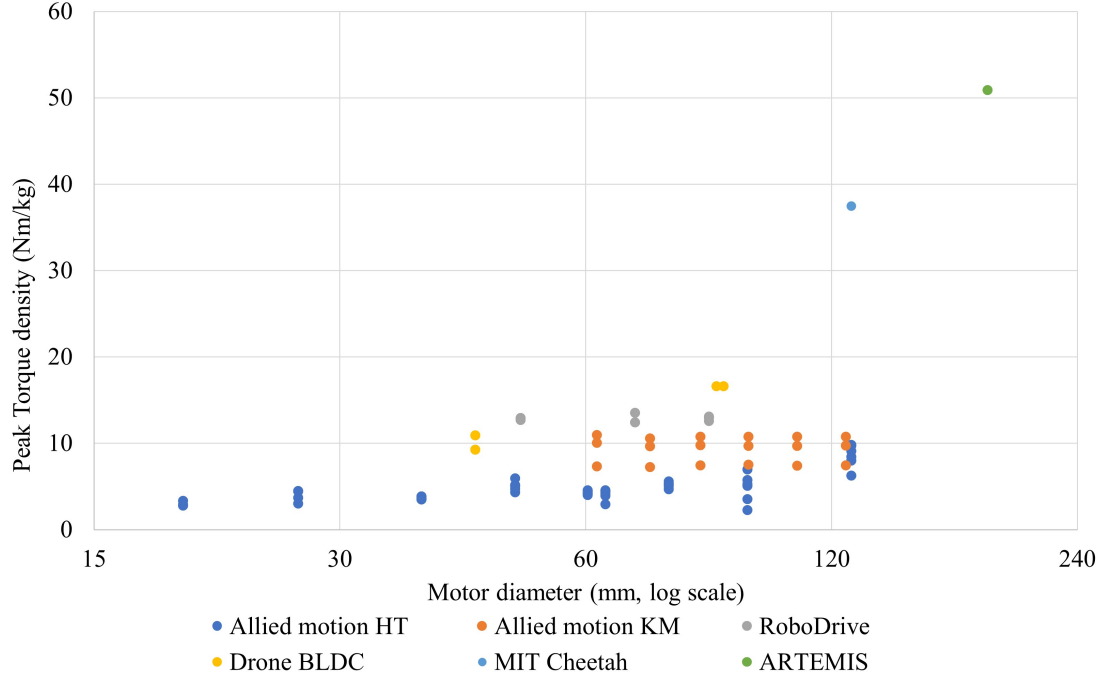


Figure 2.1: Peak torque density comparison.

Table 2.1: Custom Motor Specification

Weight	890g
Pole Pairs	40
Air Gap Diameter	180mm
Stack Height	18mm
Stall Torque	45Nm
Torque Constant	0.28Nm/A
Motor Constant	1.08Nm/ \sqrt{W}

Table 2.1 lists all design parameters for the knee motor while fig. 2.1 compares the peak torque density to commercially of the shelf motors as well as motors from other legged robot

research.

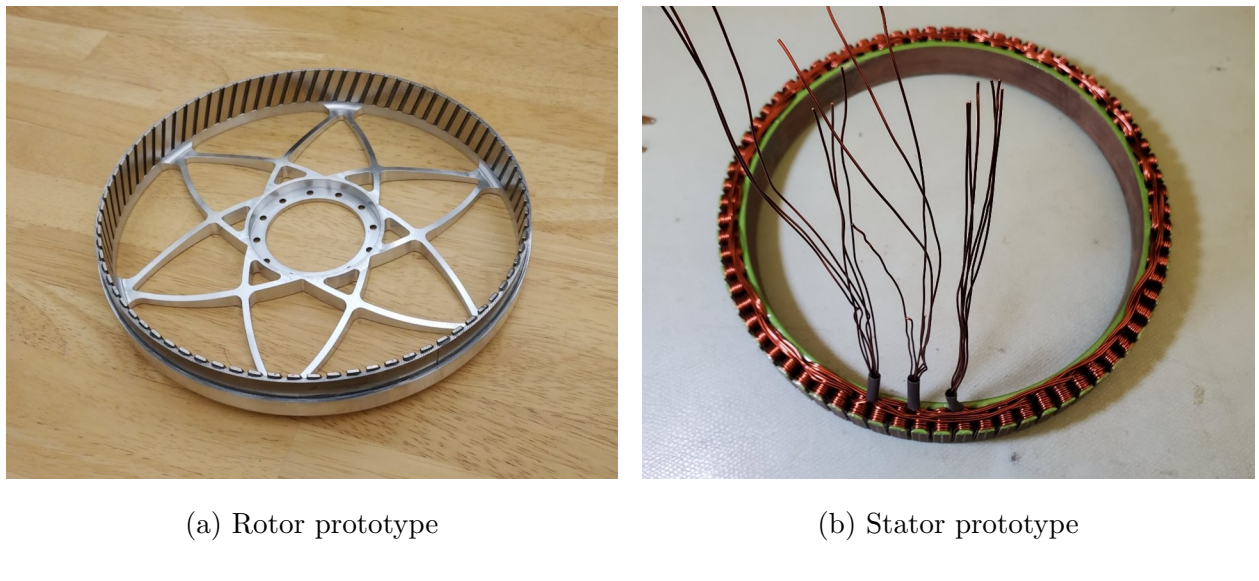


Figure 2.2: Prototype actuator rotor and stator.

The prototype motor was mounted on a custom testing rig to confirm its torque and thermal performance. Torque non-linearity at high current was also verified.

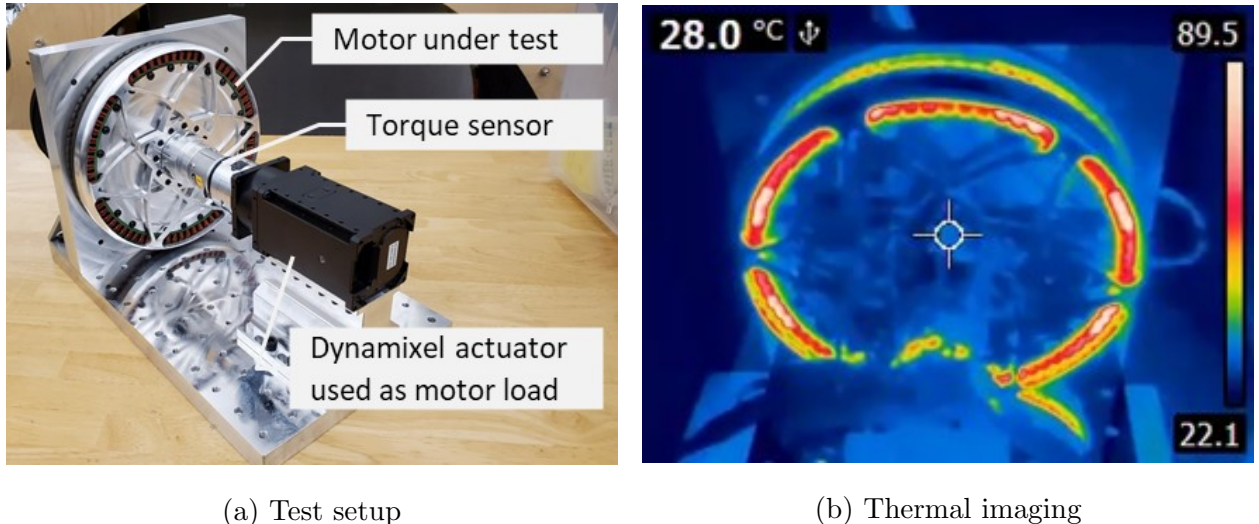


Figure 2.3: Prototype actuator rotor and stator.

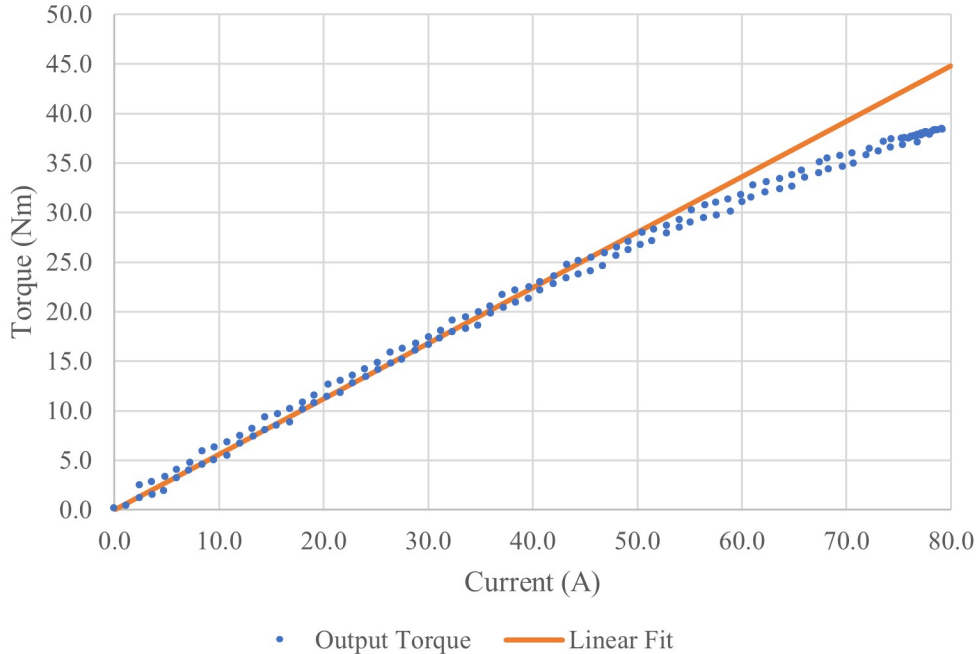
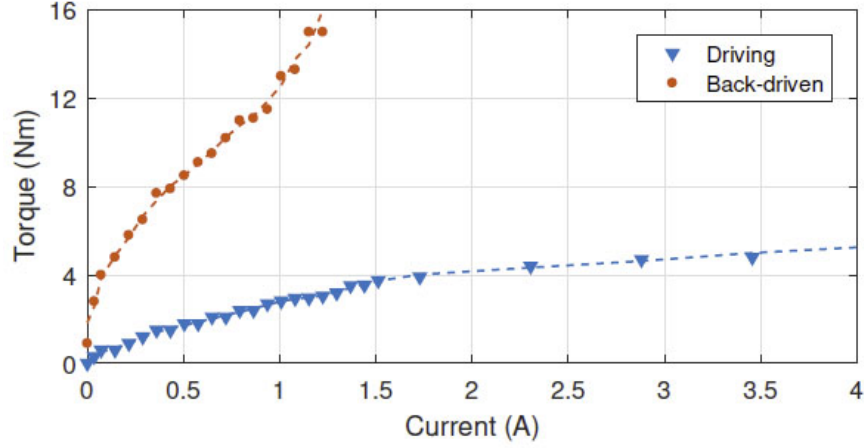


Figure 2.4: Prototype actuator torque test result.

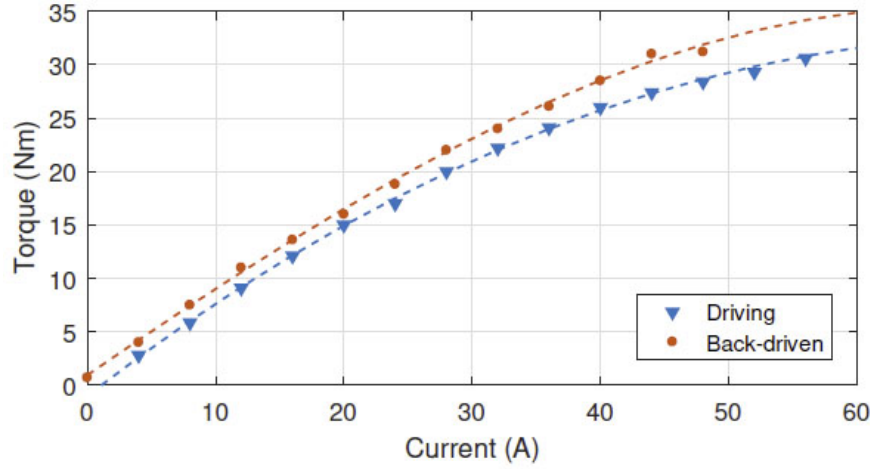
2.2 Gearbox and Packaging

Most traditional actuator design have a gearbox with large gear reduction to increase the torque density of the actuator. However, this is at the detriment of the transmission transparency. The transparency describes how easy it is for external load to transmit through the gearbox to the motor. Unlike for traditional robotic arms, high gear reduction to decouple motor dynamics from external disturbances is in fact favored. For better transparency, non-linear terms for the gearbox such as friction and backlash need to be minimized.

The benefit of such design is shown in figure where the driving and back-driven torque of the actuators are compared. Figure 2.5a shows the torque profile of Dynamixel MX-106 actuator with reduction ratio of 225:1. When the actuator is driving external load, the torque follows the expected linear curve with some friction loss at high torque. However, when trying to back-drive the actuator with external load, the resultant torque increases rapidly. The torque quickly reached the limit of the gearbox and the gears are permanently deformed. Contrasting the results from MX-106, fig. 2.5b shows the results of a large air



(a) Off-the-shelf Dynamixel MX-106



(b) Custom actuator

Figure 2.5: Drive and back-driven torque comparison.

gap motor coupled with a single stage planetary gearbox. The curve stayed linear until the drop off due to magnetic flux saturation at high current. The small gap between driving and back-driven torque can be modelled by the friction loss from the gearbox.

The favorable back-driving behavior is the direct reason that the actuator will be able to perform current based proprioceptive torque sensing. Another benefit that is not shown from the figure is that due to the friction and reflected inertia, traditional actuators will be easily damaged due to impact load. While the low reduction ratio design can withstand and transfer the impact force back through to the motor without destroying the gear train.

An added benefit of having large air gap radius motor is that it creates large empty space in the middle, which is a perfect spot to fit the gearbox inside. The radially nested rotor, stator and gearbox design makes highly space-efficient actuator packaging.



(a) custom planetary gearbox

(b) assembled rotor and gearbox

Figure 2.6: Prototype actuator gearbox.

2.3 Driver Electronics Design

In an effort to make actuators more modular, custom motor driver and controller board is developed to better fit the packaging of the actuator. When using separate off-the-shelf motor drivers, motor windings as well as encoders and thermistor need to be wired individually from the motor to the driver. Motor winding tend to have the highest current in the system, which in turn requires thick gauge wire and consequently add up to the weight of the system. When the electronics are integrated with the actuator, the only cables going between the actuators are the bus voltage and communication cable. This simplifies the system architecture and reduce the weight of the overall system.

With the advancement of modern electronics, brushless DC motor can be designed with drastically reduced system complexity. The driver is designed with a STM32F446 (ST Microelectronics) MCU, running at 180MHz. A triple half-bridge smart driver IC (DRV8320,

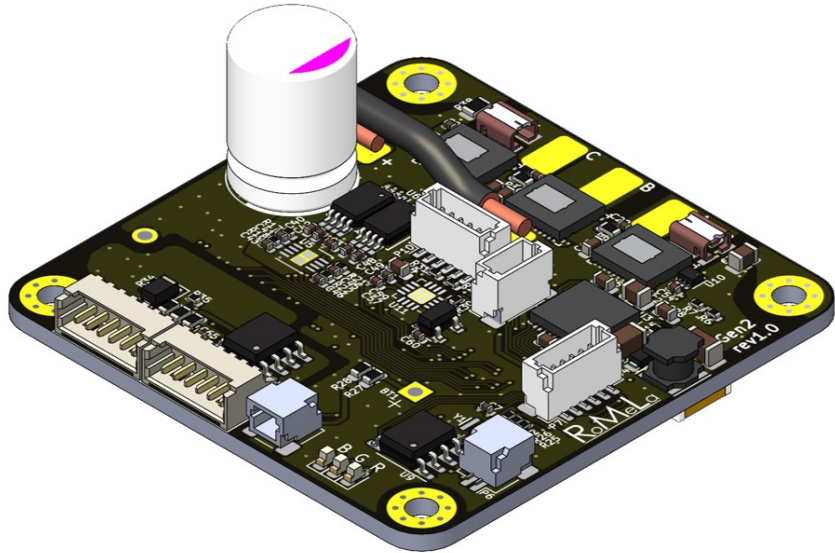


Figure 2.7: Custom motor driver PCB.

Texas Instruments) is used to both drive the MOSFETs and monitor the system for any fault condition.

Due to increased pole counts, higher resolution rotor position feedback is especially important. Onboard 14-bit magnetic absolute encoder (iC-MHM, iC-Haus) is used to provide rotor position feedback. For joint absolute positions, battery-buffered encoder (iC-PV, iC-Haus) has been used to keep count of the rotor rotations. Lithium primary battery can provide up to 10 years of rotation data retention when the robot is powered down.

A high-common-mode-voltage current sensing amplifier (INA240, Texas Instruments) measures the voltage drop across the shunt resistor and feeds into the analog to digital converter (ADC). Compared to the integrated 12-bit ADC of STM32, a standalone 16-bit ADC is used and subsequently increases the current sensing resolution by a factor of 16, resulting in more precise current control. Motor winding temperature is monitored by thermocouple in between the windings and converted using dedicated IC (MAX31855, Maxim Integrated).

For better signal integrity, the MCU communicates with the computer through an isolated RS-485 bus at 8 Mbps. A number of actuators assigned with different motor ID, would

be connected to the same multi-drop communication bus. The computer can individually address each motor or alternatively send command to all motors simultaneously.

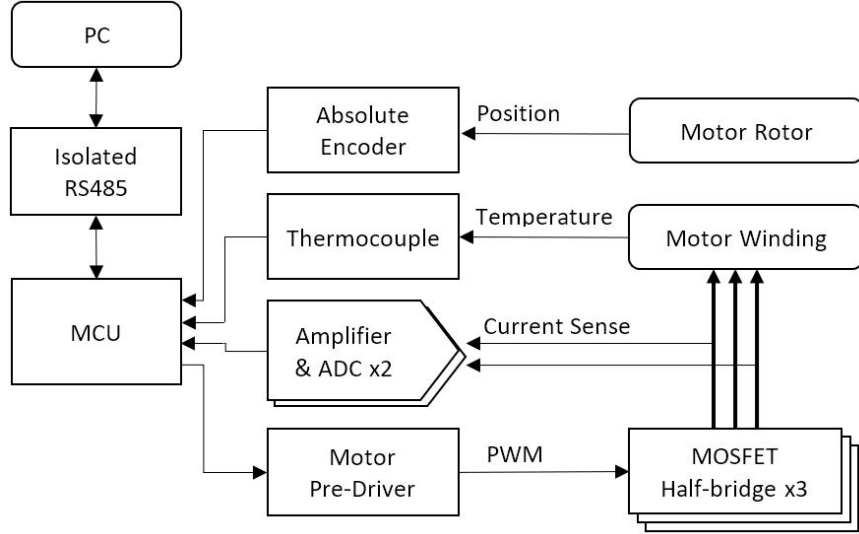


Figure 2.8: Motor driver functional diagram.

2.4 Embedded Control Structure

The onboard microcontroller of the motor driver handles the current control as well as the velocity and position loop in the respective modes. The field oriented control (FOC) algorithm running at 22 kHz handles the low level current control related to 3-phase brushless DC motor. This ensures a linear and smooth mapping between stator winding current and output torque, which is a critical part of achieving proprioceptive torque control.

The interaction between the strong permanent magnets of the rotor and the iron core of the stator causes cogging torque, which degrades the proprioceptive torque control ability of the actuator. A cogging torque compensator was used to introduce feedforward torque and thus cancel out the torque ripple. A calibration routine was used to measure the feedforward torque required for each rotor position, which then are stored in a lookup table to be used in run-time.

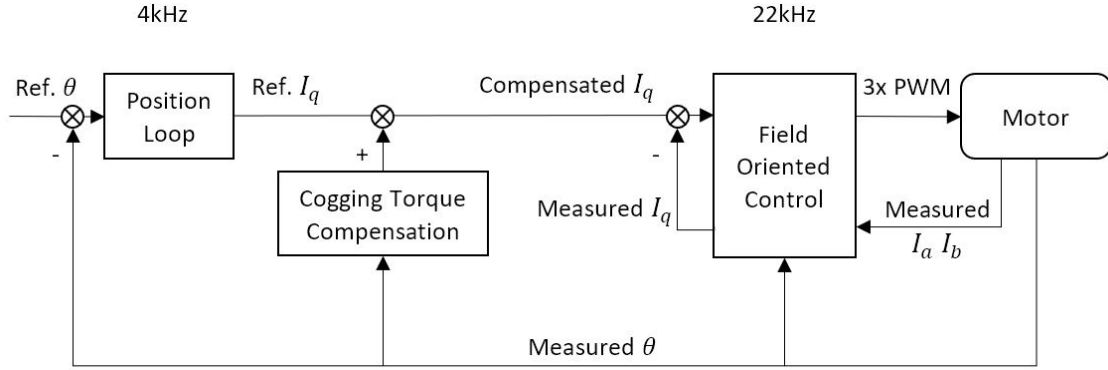


Figure 2.9: Motor driver control loop diagram.

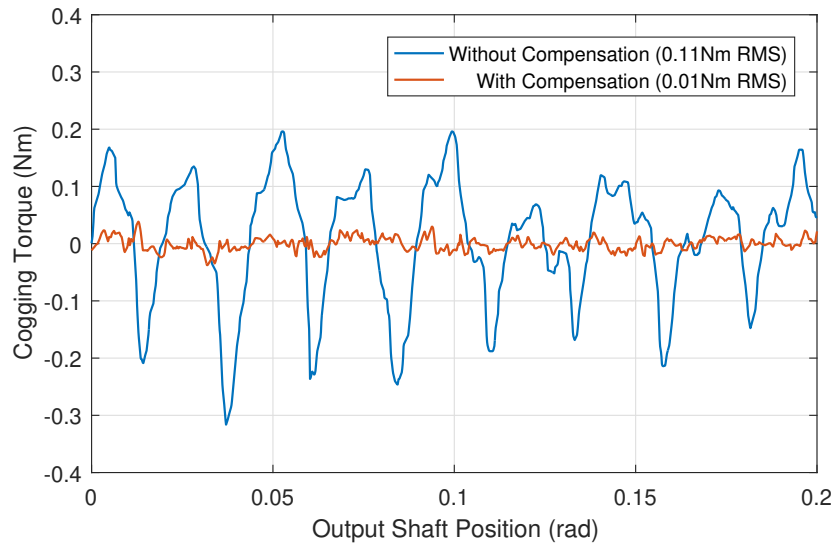
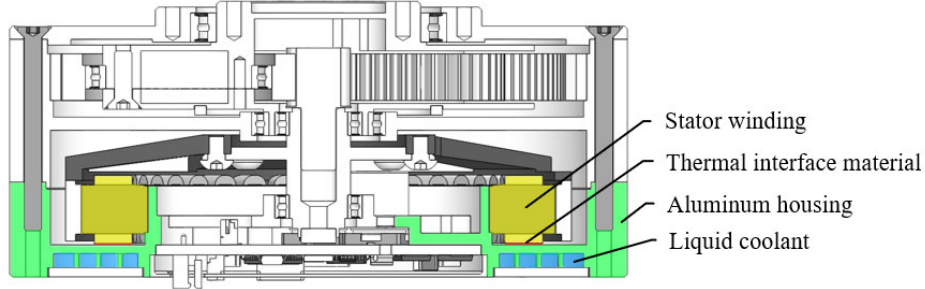


Figure 2.10: Compensated cogging torque compared to uncompensated cogging torque.

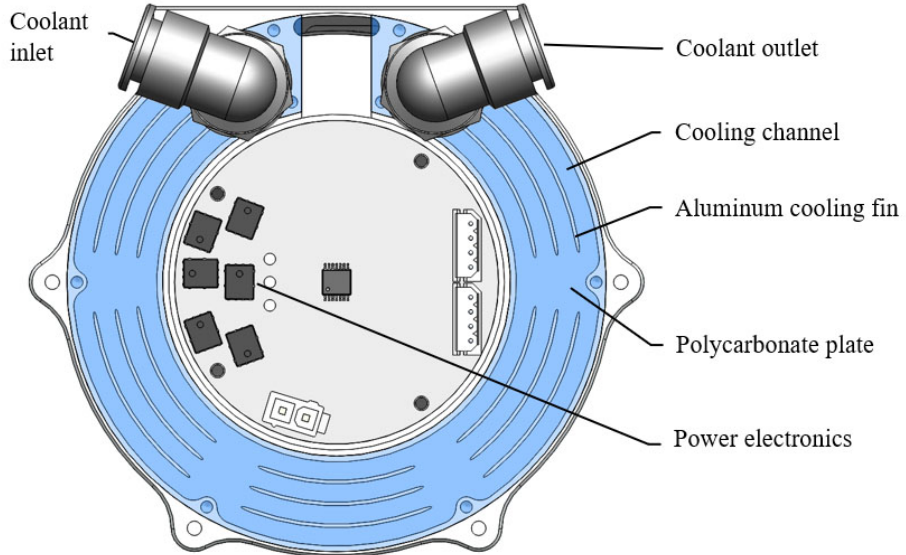
2.5 Actuator Cooling

One significant drawback of using proprioceptive actuators is that the actuators can not sustain peak load for extended periods of time due to excessive joule heating. To combat this, the robot requires extensive cooling system for uninterrupted operations. Built-in coolant channels on the actuator housing allows them to be liquid-cooled using a centralized cooling system.

To model the thermal transfer of the whole robot system, a lumped mass model was



(a) Cross section view



(b) back view

Figure 2.11: Early prototype actuator with liquid cooling.

developed to capture both the air cooling and water cooling of the whole system.

$$\frac{dT_W}{dt} = \frac{1}{C_W} \left[P_e - \frac{T_W - T_H}{R_1} \right] \quad (2.7)$$

$$\frac{dT_H}{dt} = \frac{1}{C_H} \left[\frac{T_W - T_H}{R_1} - \frac{T_H - T_L}{R_4} - \frac{T_H - T_a}{R_2 + R_3} \right] \quad (2.8)$$

$$\frac{dT_L}{dt} = \frac{1}{C_L} \left[\frac{T_H - T_L}{R_4} - \frac{T_L - T_a}{R_5} \right] \quad (2.9)$$

$$T_{HM} = T_H - \frac{R_2(T_H - T_a)}{R_2 + R_3} \quad (2.10)$$

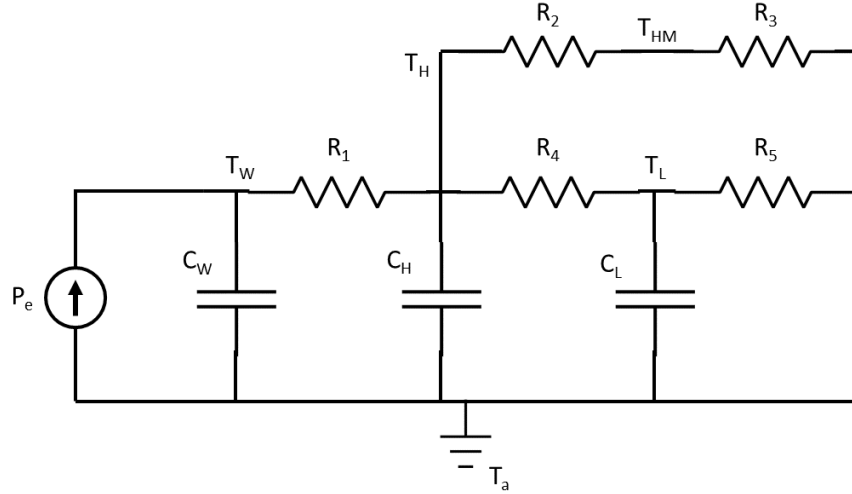


Figure 2.12: Lumped mass model of liquid cooling system.

Table 2.2: Notations for liquid cooling thermal model.

Variable	Description
P_e	Heating power
T_W	Winding temperature
T_H	Housing temperature
T_{HM}	Measured housing temperature
T_L	Liquid temperature
T_a	Ambient temperature
R_1	Thermal resistance from winding to housing
R_2	Thermal resistance from housing to thermal couple
R_3	Thermal resistance from thermal couple to ambient
R_4	Thermal resistance from housing to liquid
R_5	Thermal resistance from liquid to ambient
C_W	Thermal capacitance of winding
C_H	Thermal capacitance of housing
C_L	Thermal capacitance of liquid

The model was verified by experimental data on NABi V2, which has 6 liquid-cooled actuators and one radiator. The model can then be used to inform the design decisions for a whole robot system.

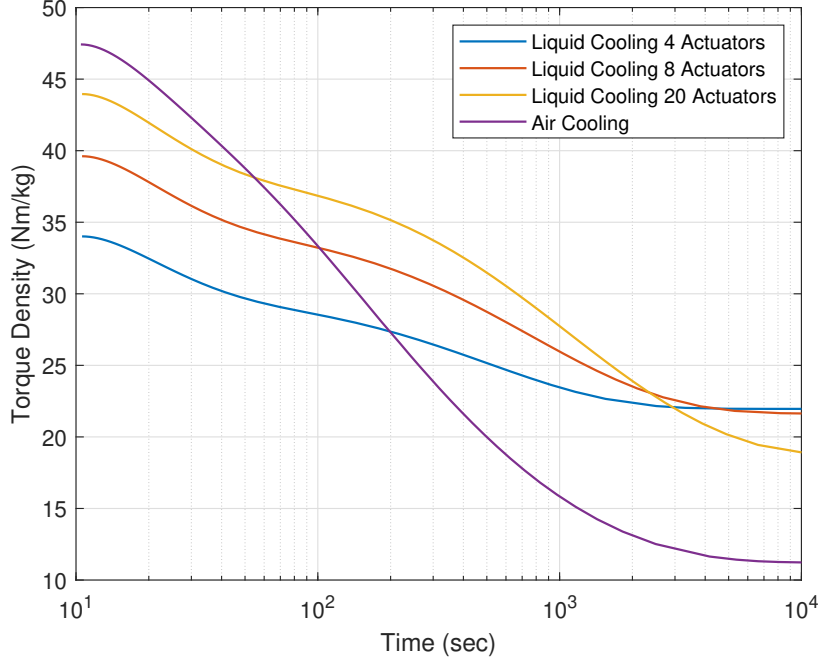


Figure 2.13: Actuator torque density with respect to duration.

From the liquid-cooled actuator design, we concluded that the main bottleneck for thermal transfer is in fact from the stator winding to the housing. In order to further improve cooling performance, direct thermal transfer from winding to working fluid can be achieved with a wet stator design. Conventional wet stator design uses sleeve to encapsulate the assembly, or in some cases allows leakage into the air gap leads to inefficiencies. The proposed design used epoxy resin to bridge the gap between the stator teeth, thus accomplished direct thermal transfer to liquid without compromising the air gap.

Experiment setup was devised to compare the thermal performance across all cooling methods. This includes actuator module in still air, actuator with forced air cooling, actuator with liquid cooled housing and actuator with immersion cooling. The results show that with just forced air cooling, the thermal resistance can drop by almost 4 times, in turn almost

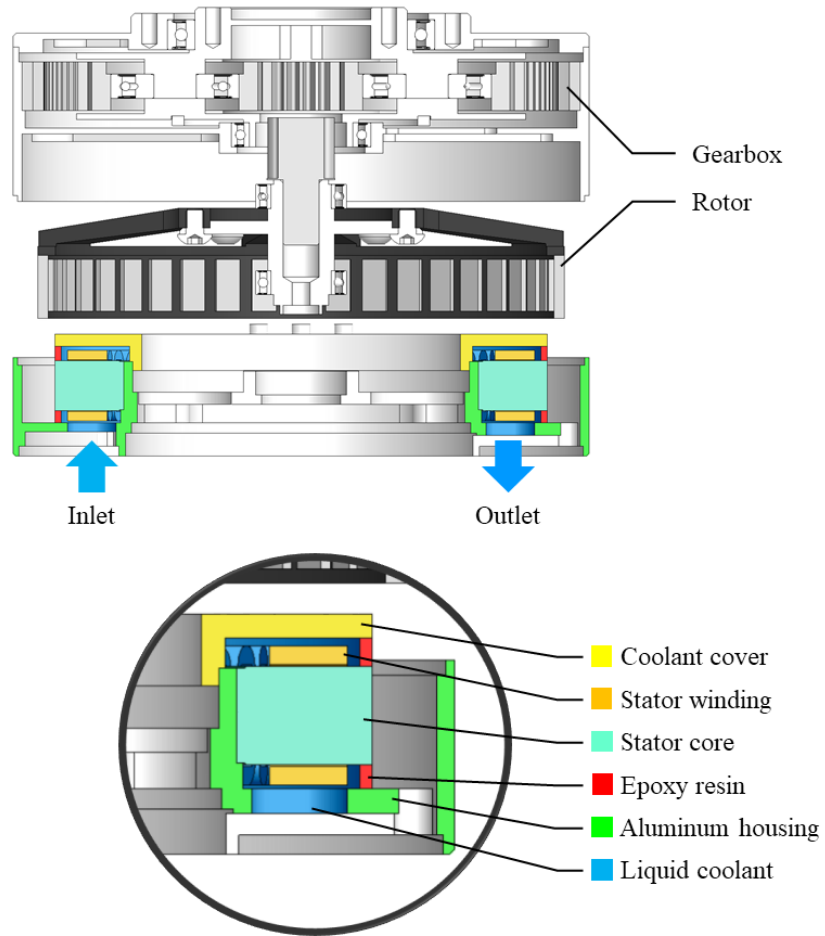


Figure 2.14: Section view of prototype immersion cooling.

double the continuous torque. Thermal resistance can be reduced further by 2.8 times when liquid cooling is introduced. When tested with immersion cooling, the thermal resistance was further reduced by 3.7 times, an order of magnitude better than forced air cooling.

As observed from fig. 2.15, the continuous torque value hit diminishing in return when moving from liquid cooling to immersion cooling. This is because the high current used during immersion cooling experiment is saturating the stator core, torque can not be increased further. Due to this, as well as the system complexity associated with immersion cooling, liquid cooling has been ultimately chosen for the system.

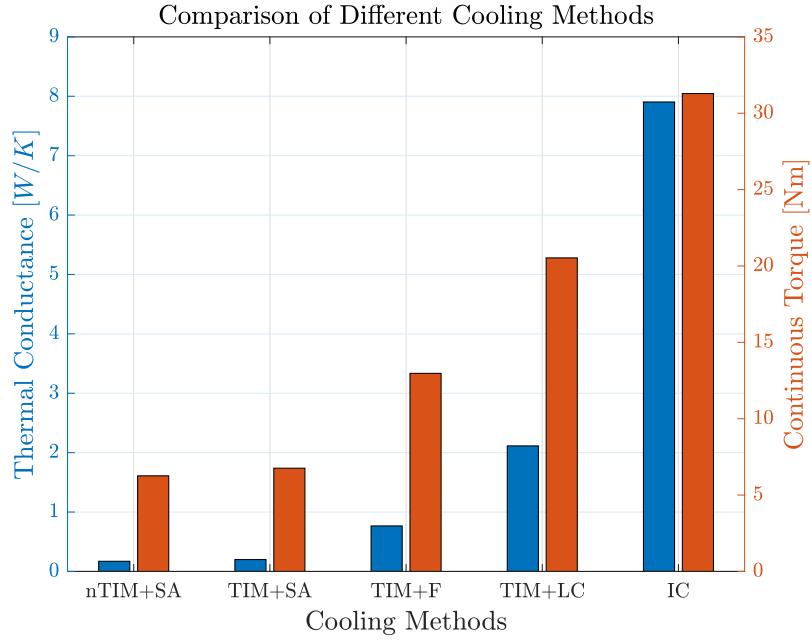


Figure 2.15: Different cooling method actuator torque density comparison.

Table 2.3: Torque density with the different cooling approaches.

	R_{WA} (K/W)	Continuous Torque (Nm)	Weight (g)	Torque Density (Nm/kg)
nTIM+SA	5.84	6.3	646	9.7
TIM+SA	4.99	6.8	668	10.1
TIM+F	1.31	13.0	713	18.2
TIM+LC	0.473	20.5	751 ^a	27.3
IC	0.127	31.3	823 ^a	38.0

nTIM+SA: no thermal interface material, still air.

TIM+SA: potting thermal compound, still air.

TIM+F: potting thermal compound, forced air cooling.

TIM+LC: potting thermal compound, liquid cooling.

IC: immersion cooling.

^a 83 g and 167 g cooling system weight distributed for LC and IC respectively.

2.6 Actuator Variants

For a complex system such as a humanoid robot, ideally each actuator would be tailored to its own torque and power requirements. Due to resource limitations and for better parts consolidation, a total of 5 different variants of the actuators were designed.

Table 2.4: Actuator Specifications

	Hip roll and yaw	Hip and ankle pitch	Ankle pitch	Arms	Head
Approximate weight (g)	850	3000	350	300	250
Gear reduction	14.5	5.9	50.3	19.2	9
Peak torque (Nm)	85	250	25	32	12
Continuous torque (Nm)	30	80	8	8	3
Velocity (rad/s)	25	23	30	30	50
Reflected inertia (kgm ²)	0.049	0.088	0.020	0.008	0.001

CHAPTER 3

Mechanical Design

3.1 Lower Body Kinematics and Structure

Traditionally humanoid robots are designed with 6 degrees of freedom (DoF) legs. They are hip yaw, hip roll, hip pitch, knee pitch, ankle pitch, and ankle roll, which is analogous to traditional 6-DoF robotic arm design. The three hip degrees of freedom intersect at one point and form a ball joint to orient the leg. The knee is used for leg extension and flexion, which changes the leg length and provides most of the force when walking and running.

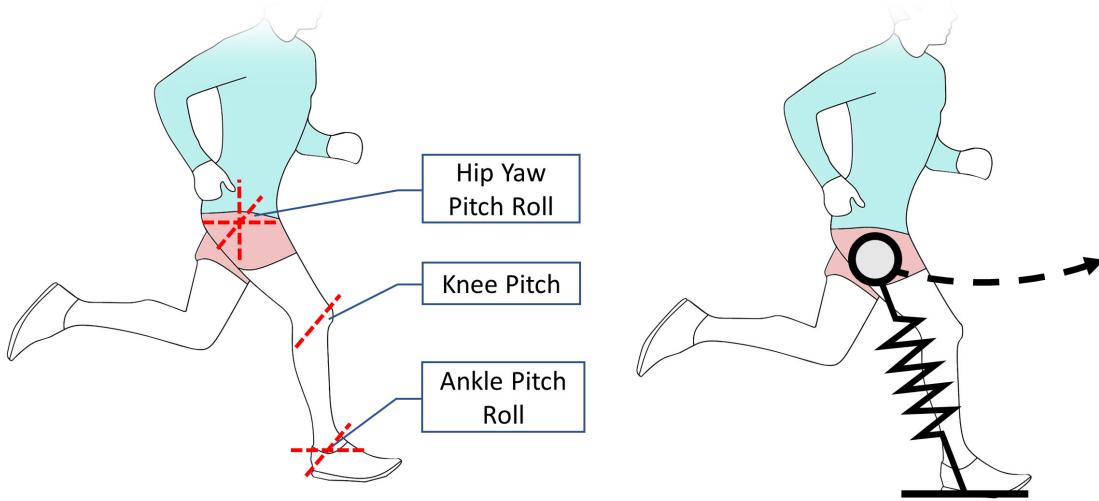


Figure 3.1: Human lower body joints and spring-loaded inverted pendulum model.

The ankle pitch and roll, however, defer in functionality to that of human counterpart. When we are walking, ankle pitch provides significant energy input at toe-off. This extends the effective length of our leg and in return benefits energy efficiency. On the contrary, due to rigid flat foot design of a humanoid robot, toe-off is generally not utilized, therefore

reduce the requirements for ankle torque. Additionally, when walking especially at speed, the system closely resembles a spring-loaded inverted pendulum. This indicates ankle pitch and roll are mostly unutilized when walking and running, thus resembles the point feet assumption.

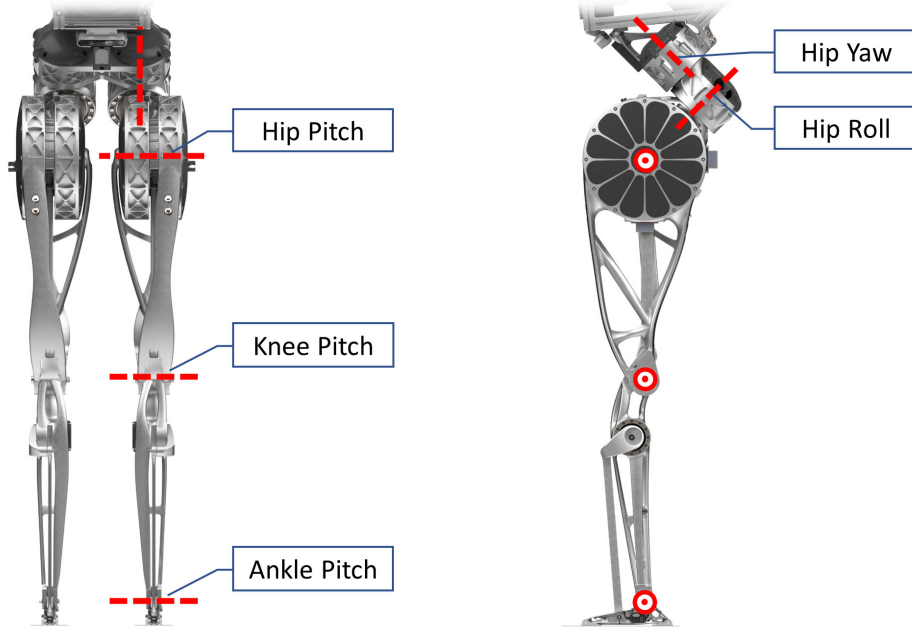


Figure 3.2: Lower body joints.

Another factor to consider is the added weight of ankle actuator at distal position. At speed, it is critical to minimize the moving mass and inertia, which affects the dynamics of the robot. Higher distal mass makes impact and touchdown more violent as well. Altogether, it is decided to make the leg consists of only 5 degrees of freedom. The ankle roll degree of freedom is omitted to minimize distal mass of the leg.

The benefit of such design is that the leg can accelerate much faster during swing phase, which is beneficial to fast walking and running as well as disturbance rejection. The downside is that without ankle roll, the robot will not be able to balance on one leg due to the missing degree of freedom. This is a worthwhile trade off for designing the robot for highly dynamic maneuvers.

Traditionally, hip yaw and hip roll degrees of freedom would be aligned with the human

Table 3.1: Lower Body Joints Specifications

	Range of motion (°)	Peak torque (Nm)	Joint Velocity (rad/s)
Hip yaw	-90 – 45	85	25
Hip roll	-45 – 45	85	25
Hip pitch	-133 – 78	250	23
Knee pitch	19 – 160	250	23
Ankle pitch	-70 – 50	25	30

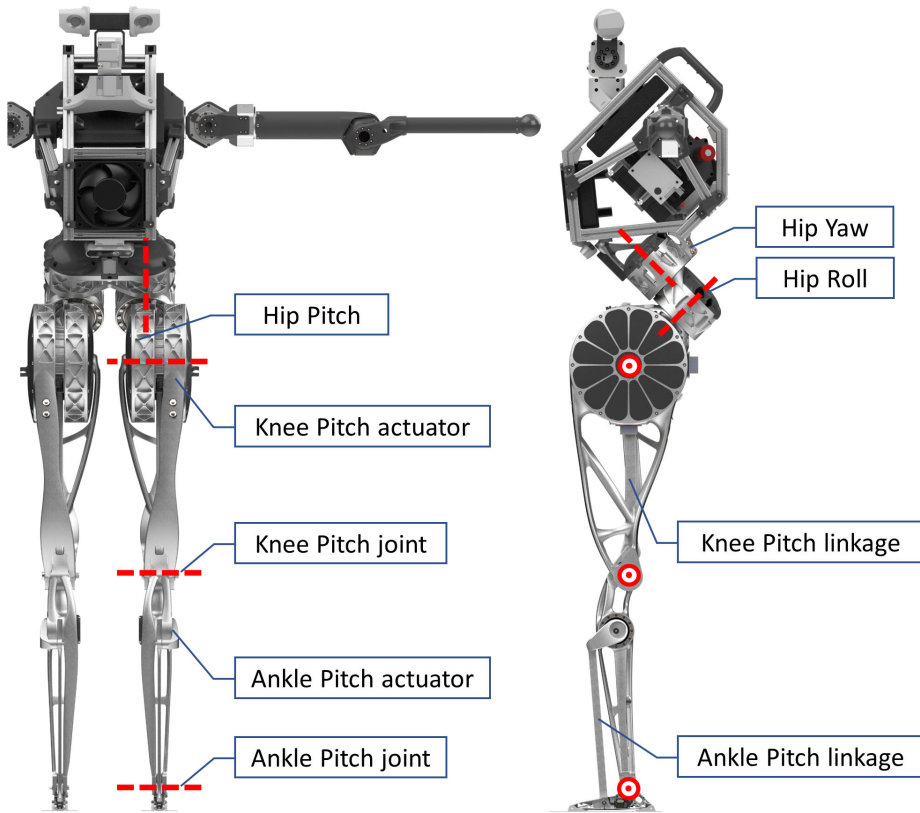


Figure 3.3: Lower body joints and actuator locations.

body main axes, which means hip yaw would align with longitudinal axis and hip roll would align with sagittal axis. The torque and power requirements for hip yaw and roll is very different, that walking and running requires much higher hip roll torque. Consequently, to optimize the design, two different sized actuators would be required.

One solution is to simply tilt both hip yaw and hip roll axes forward by 45 degrees. By doing so, the torque is much more equally distributed between the two actuators while walking. As a result, same actuator module can be utilized for both actuators without special customization. An added benefit of such design is that the hip yaw and roll actuators are now tucked away to the backside of the pelvis structure. This gives femur much better clearance for the hip pitch range of motion, which is beneficial for moving in the knee closer to the chest such as squatting motion.

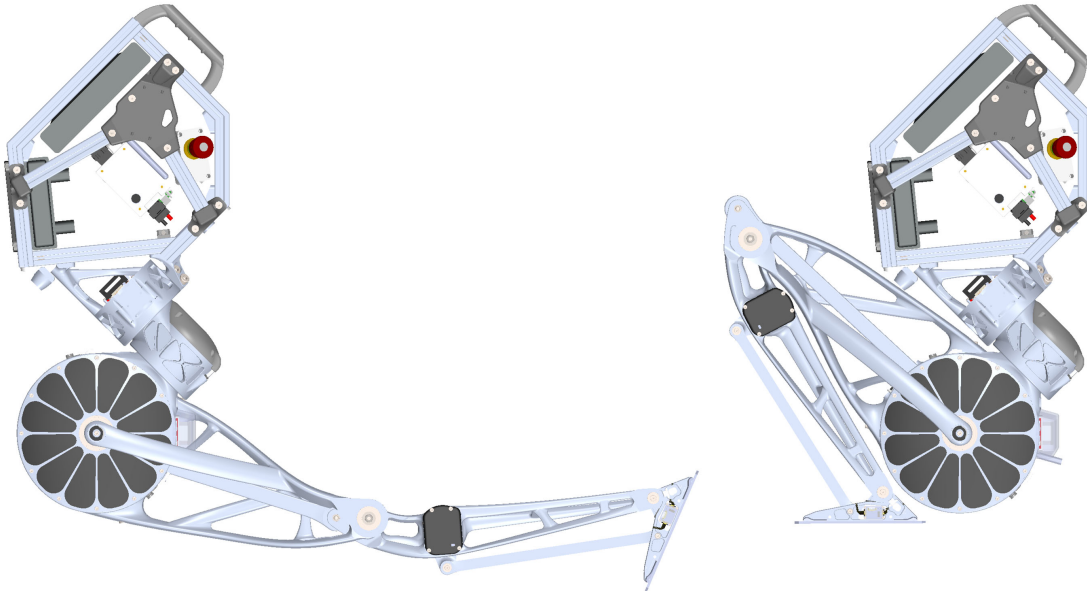


Figure 3.4: Hip pitch range of motion.

Figure 3.4 shows the large workspace of the hip pitch from -133 degree to 78 degrees due to the pelvis configuration. Figure 3.5 demonstrates different poses the robot can achieve with the wide range of motion the hip can provide.

As mentioned previously, reducing distal mass is a critical part of the design process. A common way of reducing distal mass is to relocate the actuator away from the joints to a more proximal location.

Belt or chain can be used to transmit rotation from the actuator to the joint with high efficiency. However, chains suffer from variable transmission ratio while belts are much

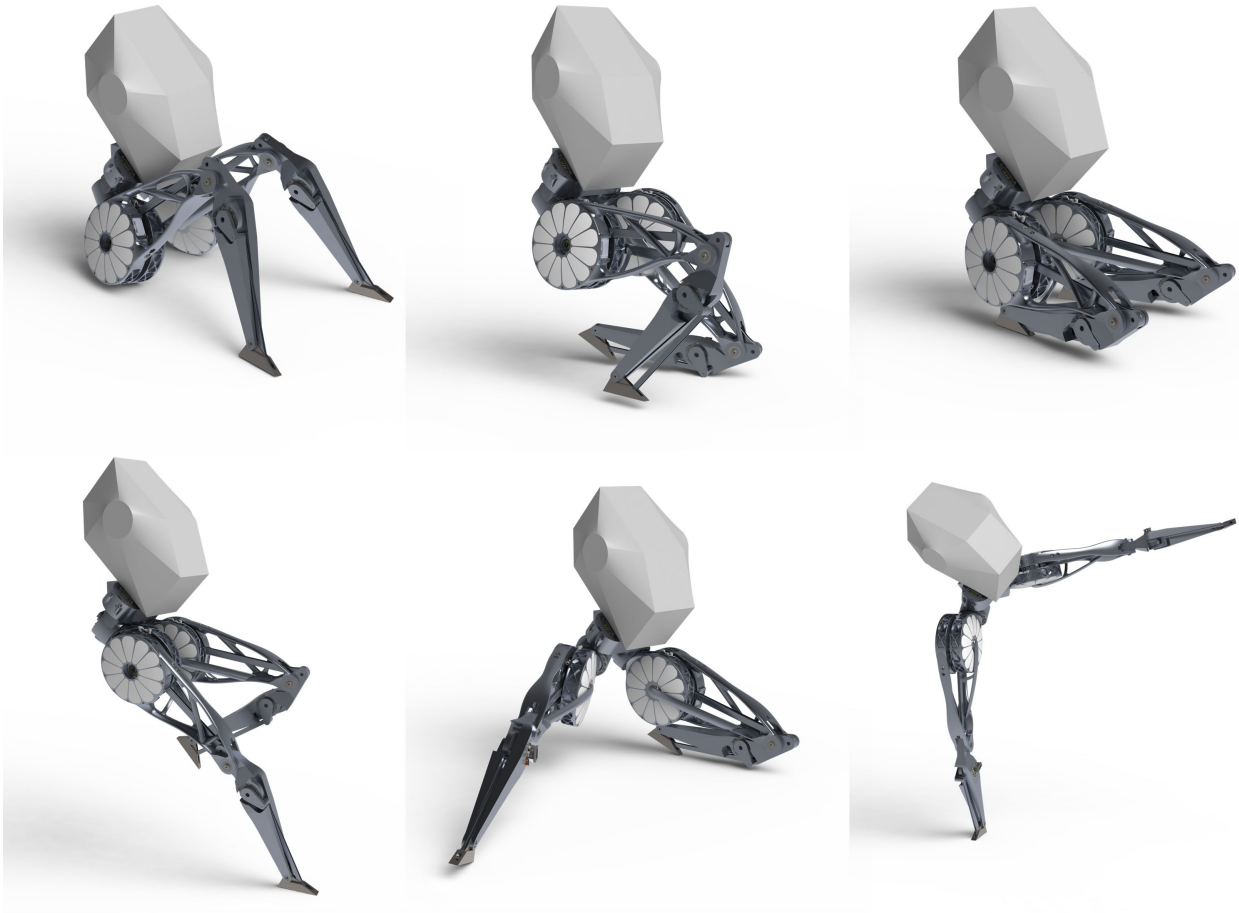


Figure 3.5: Lower body range of motion in different poses.

less stiff causing excessive deflection. It should be noted that stiffness issue can be largely remediated by using belt before the reducer. But such solution would increase the complexity of the over all system.

Instead of locating the actuator at the joint, linkages are used to move actuators proximally and transfer the motion down to the actual joint. The knee actuator has been moved up to be coaxial to the hip pitch actuator, while ankle pitch has been relocated much closer to the knee.

Figure 3.6 attempts to show the difference between the ARTEMIS lower body design compared to a traditional humanoid design in terms of mass distribution. Accumulated mass from the feet has been plotted as a percentage of the entire leg weight.

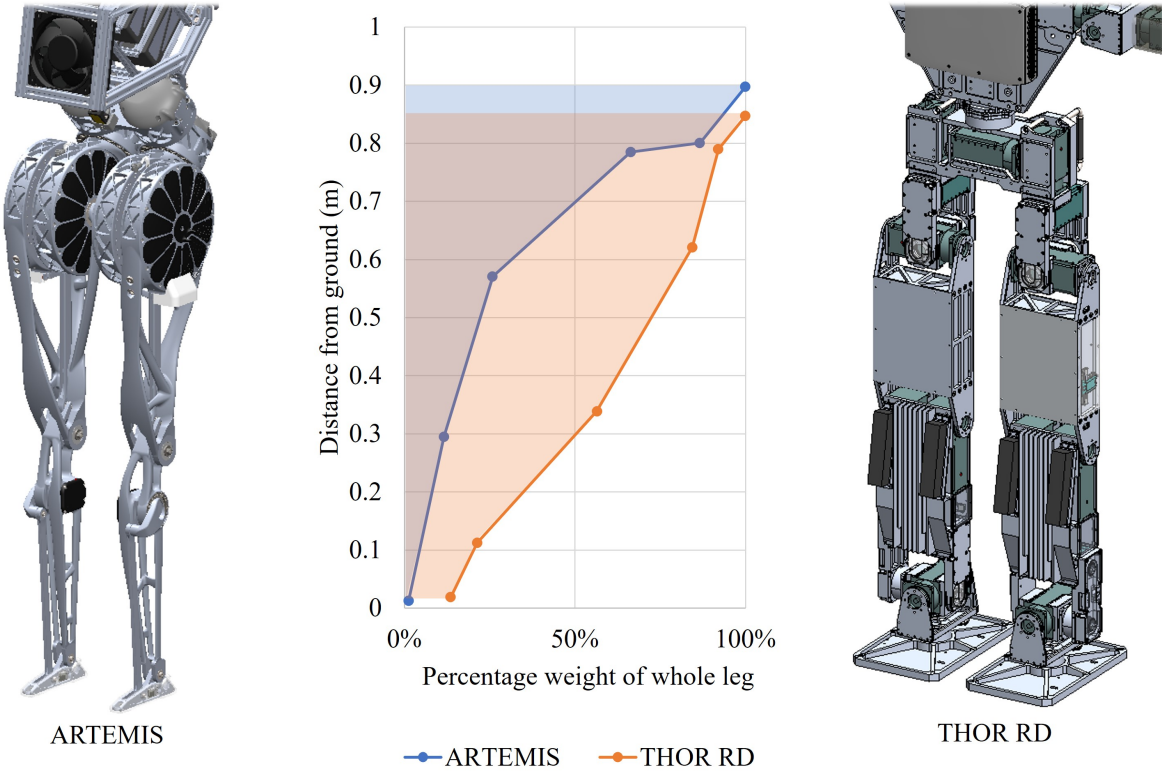


Figure 3.6: Mass distribution of the lower body.

Table 3.2: Robot weight distribution comparison

	ARTEMIS	THOR RD
Torso and head (kg)	13.16	15.72
Arm (kg)	1.22	7.10
Hip roll (kg)	1.44	0.94
Hip pitch (kg)	2.19	0.91
Femur (kg)	5.90	3.32
Tibia (kg)	1.12	4.16
Foot (kg)	0.14	2.53

THOR RD's mass distribution plot shows that, in fact, over half of the weight of the leg is below the knee. This unwanted mass distribution is due to a multitude of factors.

The wide foot plate together with the F/T sensor adds to the already bulky 2 degrees of freedom ankle design. Knee actuators are located in the tibia, which increases distal mass significantly. Hollow femur structure has been used as battery compartment, housing the 2kg lithium battery in each leg.

In contrast, the majority of the weight of ARTEMIS leg is around the hip area, which is more than 60% of the whole leg weight. Considering the leg inertia about the hip joint, ARTEMIS design allows for much higher acceleration of the leg, contributing to the robustness of the robot.

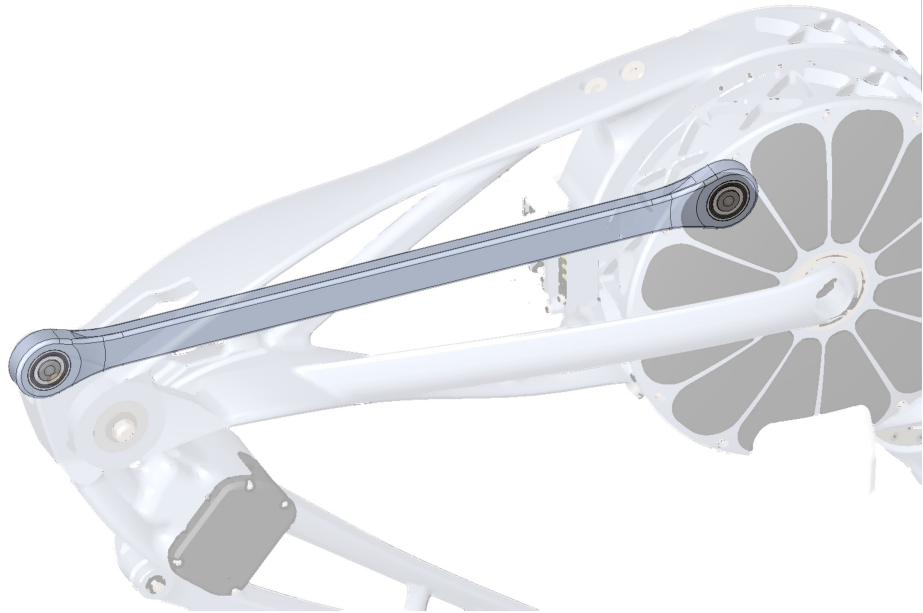


Figure 3.7: Knee linkage within the femur structure.

Parallel four-bar linkage has been used for simplicity at the expense of reduced range of motion. This is because when the joint approaches singularity, linkage force increases drastically, limiting the available torque. As shown in Figure 3.8, a designed linkage force of 15kN has been used to size the linkage. Approximately 140 degrees range of motion can be achieved without compromising peak torque at the knee joint.

Linkage buckling is another concern. As a result, linkage cross section has been optimized to minimize the chance of buckling. Linkage is also placed in a location such that the

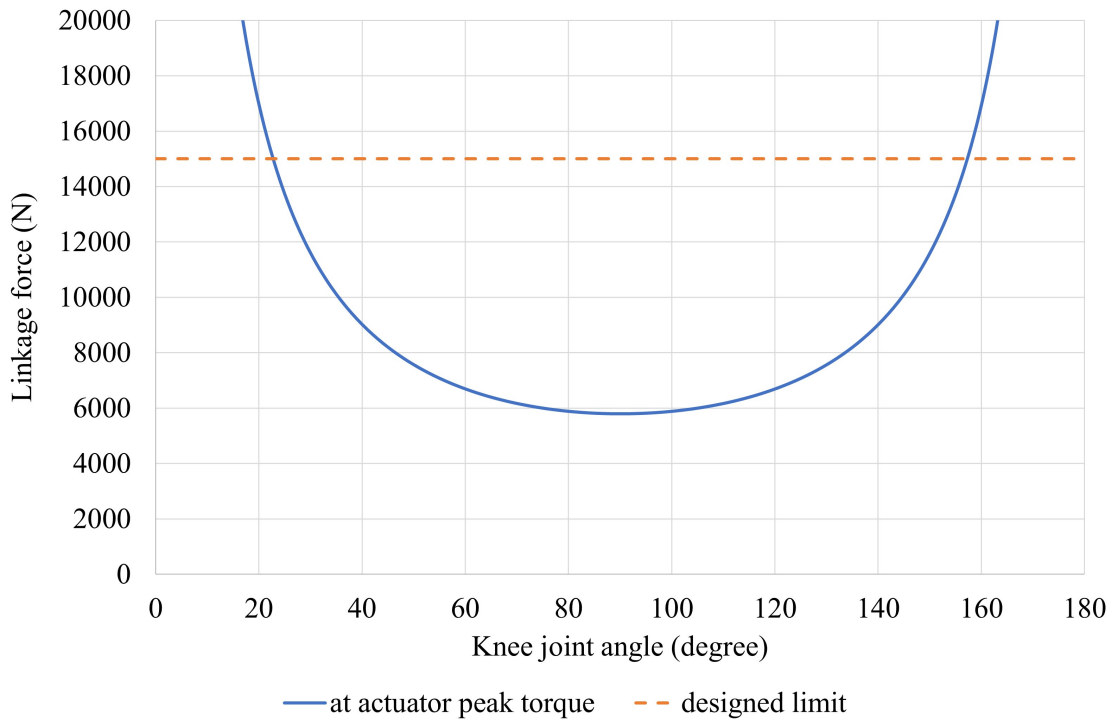


Figure 3.8: Linkage force with varying knee joint position.

maximum knee extension force occurs when linkage is in tension.

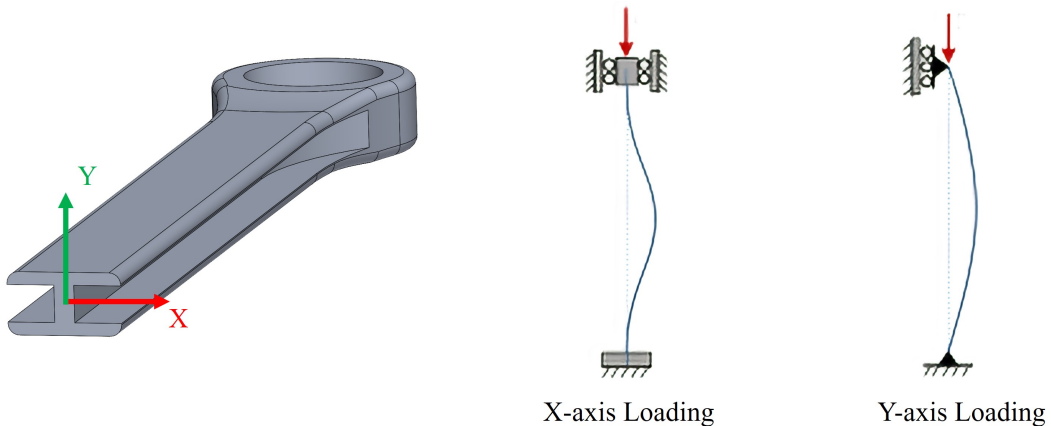


Figure 3.9: Linkage buckling condition.

To minimize transmission loss, full complement roller bearings (IKO NAG4901UU) have been used as rod ends. Compared to plain bearings, roller bearings have much lower friction as well as backlash, at the expense of slightly heavier weight. Roller bearing also constrains

Table 3.3: Knee linkage buckling analysis

	X-Axis	Y-Axis
Column length (mm)	375	375
Cross-sectional area (mm ²)	112	112
Second moment of area (mm ⁴)	1840	3023
Modulus of Elasticity (GPa)	71	71
Yield strength (MPa)	430	430
End conditions	Fixed-Fixed	Pined-Pined
Critical load for failure (N)	21700	15000

the motion to be in-plane, making buckling less likely to happen.

A common way of designing high degrees of freedom robot is to design actuators as modules. The benefit of modular actuator design is that the same actuator can be reused for multiple joints. Additionally, individual actuator can also be exchanged or even upgraded independent of the structure. However, the downside of such design is that more material would be wasted on the actuator housing and fasteners used to assemble actuator module to the robot, thus reduce the torque density of the overall system.

Figure 3.10 shows the construction of THOR RD, a humanoid robot who participated in the DRC finals. All joints are done using off-the-shelf dynamixel pro modular actuators. Brackets and horns are used to connect each individual actuators together to form the lower body. While this construction method made the design process much easier and straightforward, much of the weight is wasted on brackets and fasteners. Each actuator housing would also have to be designed to withstand the maximum load throughout the robot, thus wasting material.

To minimize wasted structure weight, the robot is designed to have integral structures that minimize the number of bolted connections. For instance, the proximal actuator would have its output shaft be the same structural part as the housing of the adjacent distal

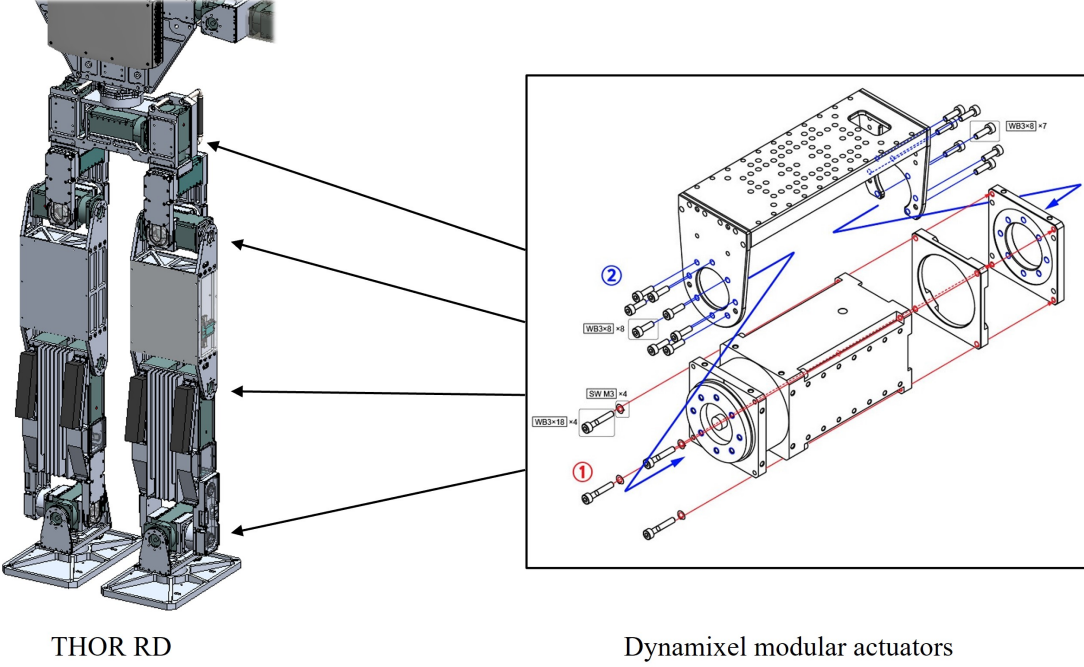


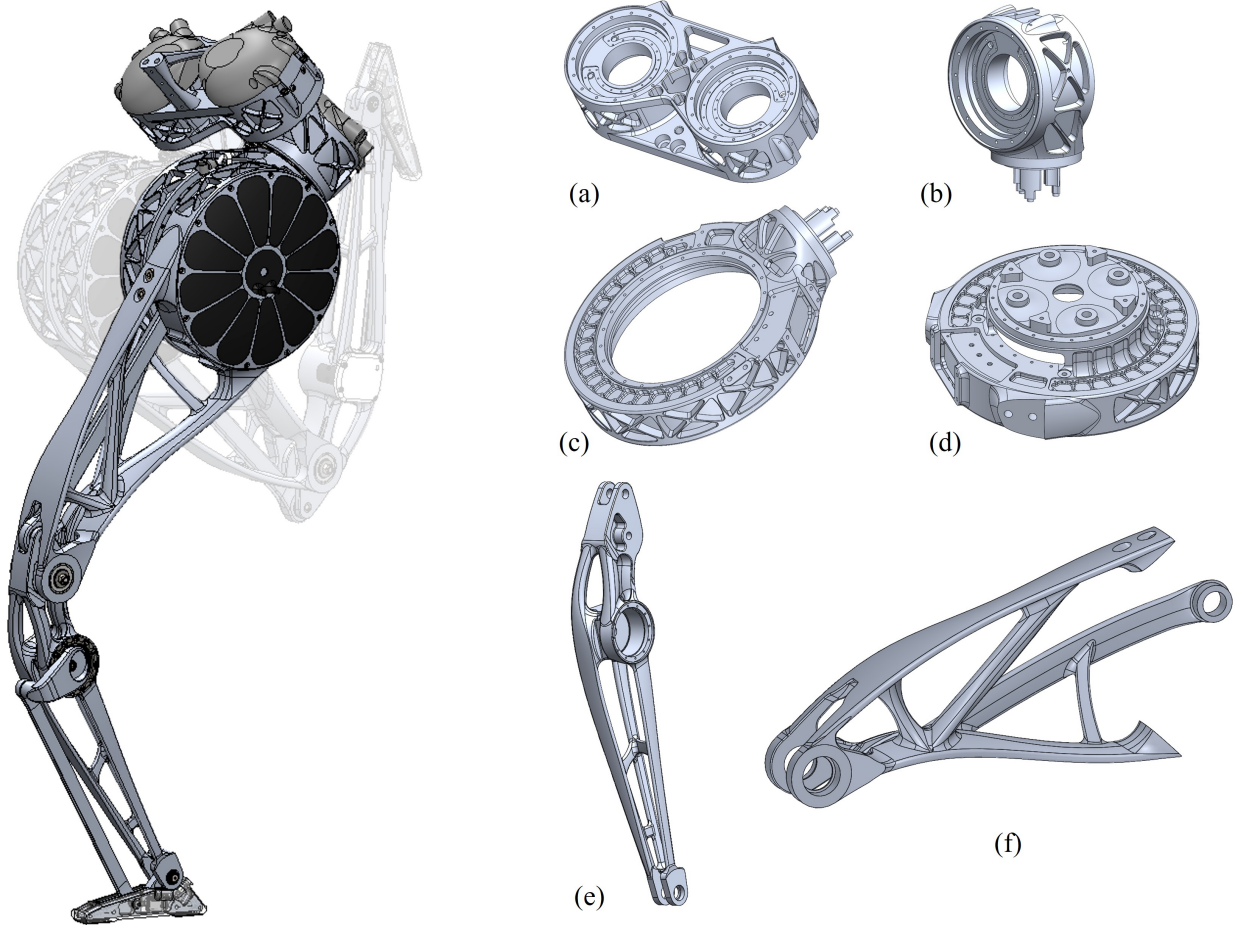
Figure 3.10: THOR RD with dynamixel actuator modules.

actuator, which eliminates the need for fasteners and alignment features. Another way of eliminating redundant parts is that all actuator housings are designed as part of the robot structure, thus decreasing the unnecessary amount of weight dedicated to actuators.

For all structural parts of the robot, such as femur and tibia, the goal is to design them as light weight as possible, while maintaining certain rigidity. For this reason, topology optimization has been utilized during the design process.

First step of the design process is to identify the maximum part envelop and boundary conditions of the part as shown in fig. 3.12 (a). For femur, connection points to the hip actuator as well as the knee bearing are defined as boundary conditions. Connection points to the hip housing are set as fixed boundary, while the bearing surface has been used to load the structure. Femur part envelop also excludes the center clearance needed for the knee linkage. For tibia, additional constraints are added for the ankle actuator housing embedded in the structure.

Secondly, topology optimization study is conducted based on minimum deflection and



(a) Pelvis structure for two hip yaw actuators. (b) Hip yaw output and housing for hip roll actuator. (c) Hip roll output and housing for hip pitch actuator. (d) Hip pitch output and housing for knee actuator. (e) Tibia structure with ankle actuator housed in. (f) Femur structure connecting hip actuators to knee.

Figure 3.11: Lower body structures.

maximum rigidity goal. Multiple load cases are included in the study, including maximum torque load from the actuators and internal force caused by the linkage design. Based on the mass reduction goal, mesh geometry can be generated representing the optimal structure, which is shown in fig. 3.12 (b).

However, in most cases, the result would not be suitable for subtractive manufacturing methods, i.e. CNC machining. The topology study could not take into account constraints

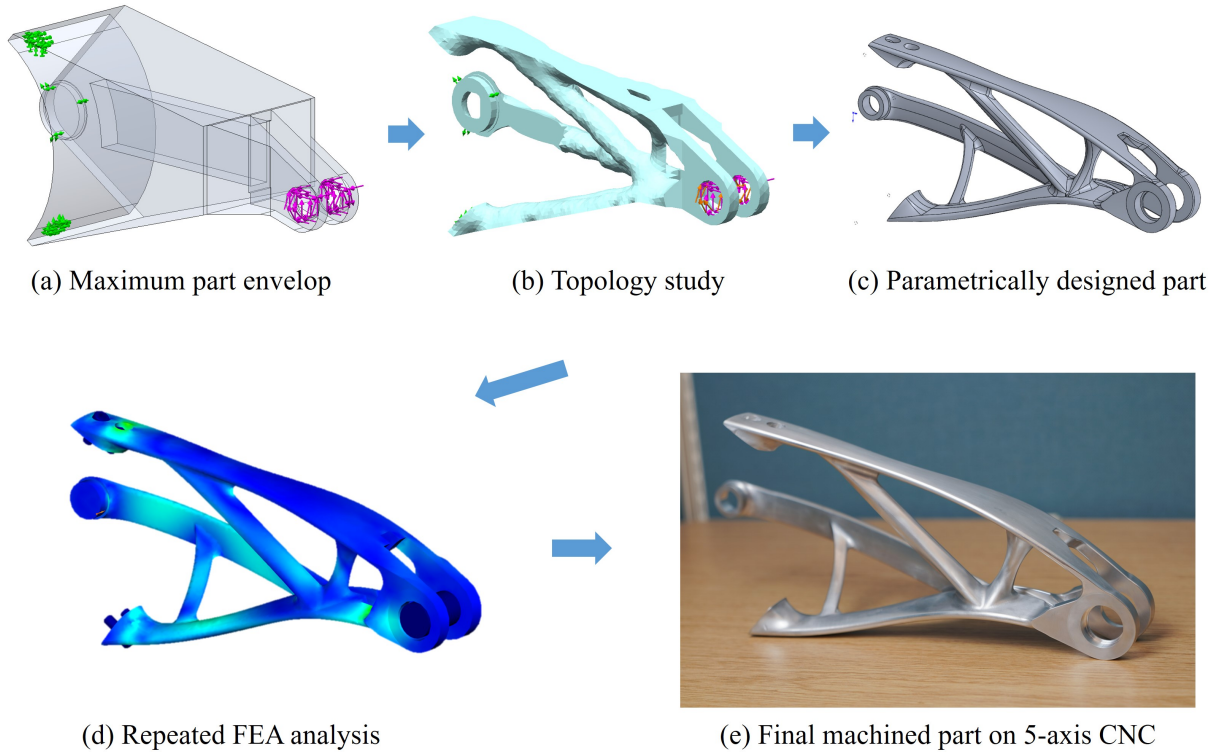


Figure 3.12: Structure topology optimization procedure.

like over-hang, minimum feature dimension, tool accessibility etc. In addition, the resultant mesh can not be further modified parametrically. As a result, parts are then manually remade in parametrical environment following the topology study results as presented in fig. 3.12 (c). The benefit of the parametrical approach is that the part can then iterate through FEA analysis as illustrated in fig. 3.12 (d) and further refine the design. Finally, the distinctively curved and organic parts are machined from solid billet aluminum using 5-axis CNC milling machine as displayed in fig. 3.12 (e).

3.2 Torso Structure

The design goal of the torso is to house all the electronics and batteries while maintaining flexibility to future design changes. As a result, T-slotted aluminum framing (20mm x 20mm) has been used to form the main structure of the torso. Computers and batteries are well

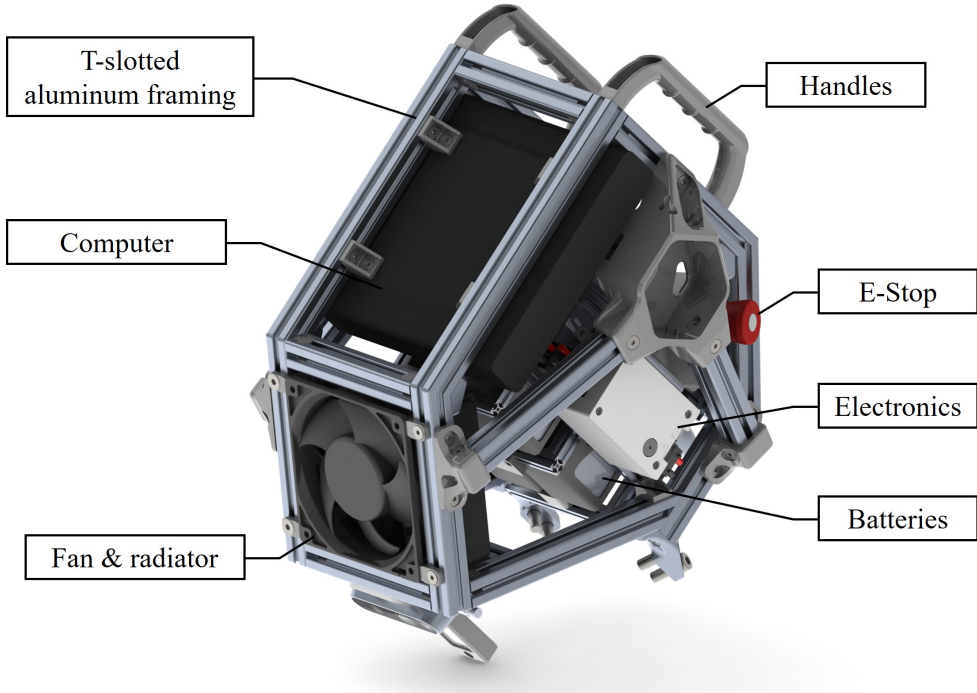


Figure 3.13: Torso structure and components.

protected inside the roll cage built using T-slotted rails, in case the robot falls on its torso. The benefit of using T-slotted framing instead of welded tube structure is that mounting features can be easily added or modified if new instruments were to be added at a later point in time. Off the shelf brackets, fasteners and hardware also made it easy to design with minimum machining requirement. Handles are mounted on the top back of the torso for easy transportation as well as proving mounting points for gantry slings.

The front of the torso houses the radiator and fan for the liquid cooling setup of the actuators. The 120mm fan (Noctua NF-F12 industrialPPC-24V-3000) draw fresh air from the front side of the robot and pushes air up and through both the computer and batteries. This helps to cool the batteries as well, since heat could build up with-in the torso, causing over-heat issue. Fan speed can optionally be controlled by the controller that constantly monitors the coolant temperature of the loop.

The computer has been mounted towards the top of the torso in an up-side-down config-

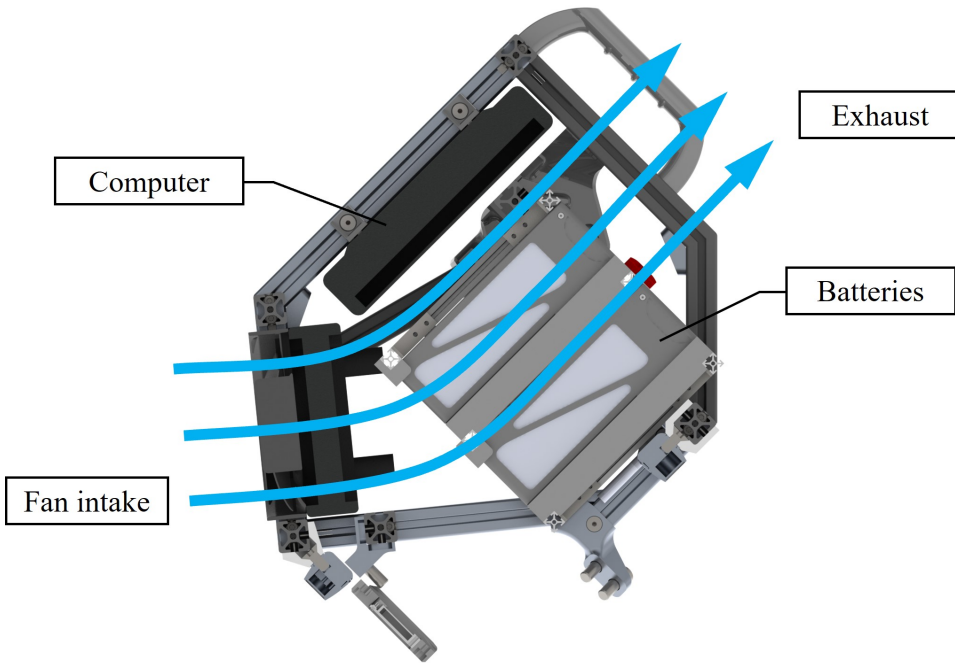


Figure 3.14: Torso internal cooling air flow.

uration. Standard VESA mount has been used to attach the computer to the torso frame. 3D-printed nylon mounting brackets also provides some vibration isolation from the torso to the computer.

The battery cage is a separate mechanically isolated structure within the torso. It is designed to withstand larger impact to prevent battery catastrophic failures under extreme conditions. Four battery slots are designed to accept custom RB56100 batteries which detailed in section 4.3.1. Retention clips are used to ensure the battery does not disconnect under vibration. DC-DC converter, wireless emergency stop, as well as other miscellaneous electronics modules are mounted to the sides of the battery, underneath the armpit.

For ease of transportation, the entire robot is designed to be easily disassembled from the pelvis, separating the torso with the lower body. With only the lower body or the upper body, when packed in a standard sized pelican case, the weight does not exceed commercial airline's baggage limit of 45kg. The upper body and lower body are located with three orthogonal planes that are all at 45 degrees to horizontal. This allows for quick self-alignment without

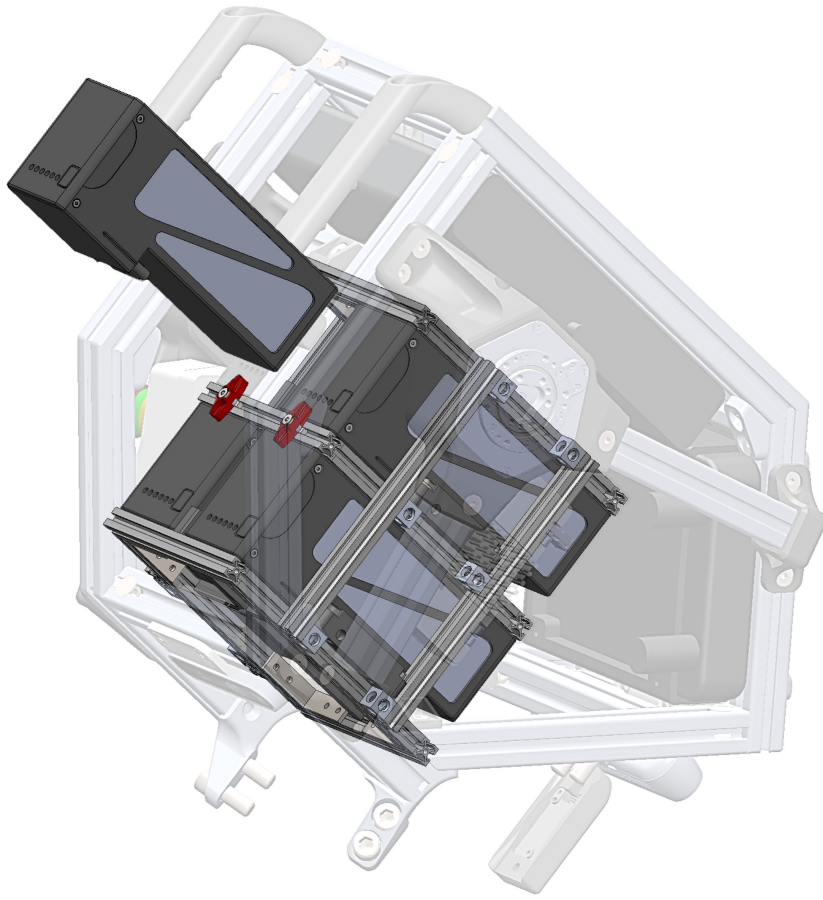


Figure 3.15: Battery cage within the torso structure.

any locating pins or jigs, making it much easier to assemble and disassemble in the field.

Figure 3.16 illustrates how when the torso is lowered onto the pelvis, the three mounting planes locates and secures the two halves of the robot.

3.3 Arm Design

While the upper body of a humanoid robot is often not the focus for most locomotion studies, argument can be had that the arm swinging motion can help the robot balancing especially when running at high speed. Not too different from us human, the swinging arm can provide a counteracting moment for the swinging leg on the opposite side. In essence, the upper

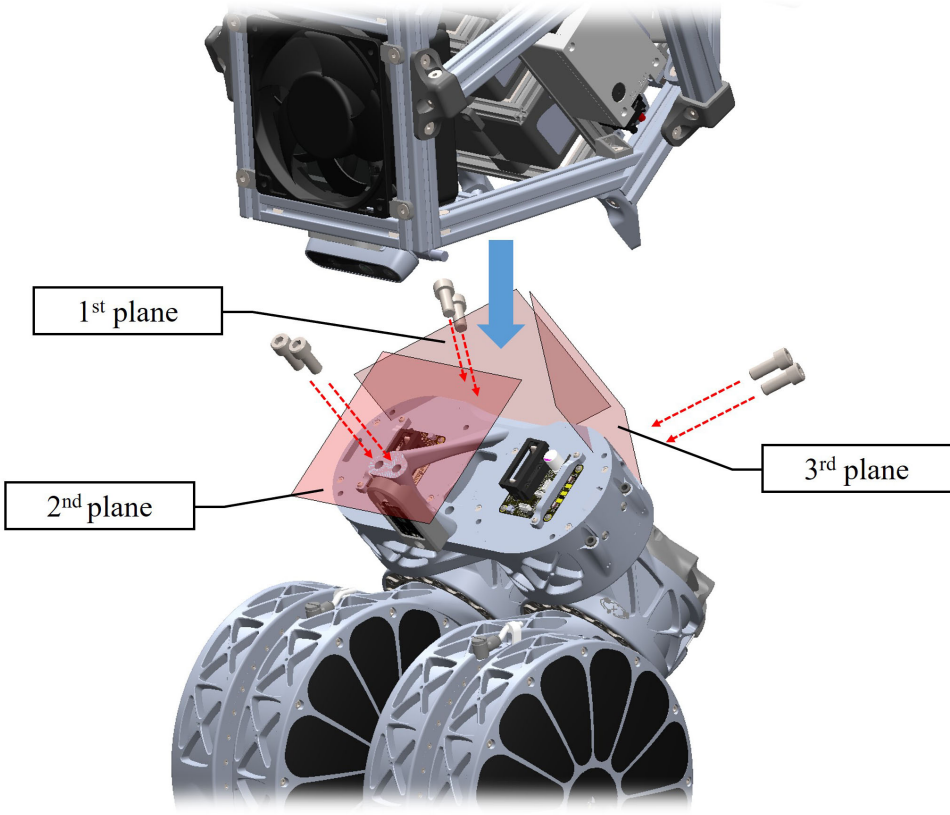


Figure 3.16: Torso to pelvis mating features.

body design will be focused on providing counterbalance for locomotion and less emphasis will be put on manipulation capabilities of the upper body. In addition, the upper body also serves as a way for the robot to get up from the ground in an event when the robot falls.

As a result, the arms will be designed with four degrees of freedom to minimize the weight of the limbs, a 3 degrees of freedom shoulder joint and a 1 degree of freedom elbow joint. Actuators are sized to be able to support the weight of the body in a fallen position and be able to swing fast enough to generate counteracting momentum.

To consolidate and reduce part count, all four actuators of each arm are of the same type. The shoulder joint has three intersecting axes in a pitch-roll-pitch configuration, which correlates to shoulder flexion/extension, abduction/adduction and shoulder internal/external rotation. Both pitch joints have output shaft in single support configuration, while the roll actuator has the output in a double support clevis configuration. The elbow pitch actuator

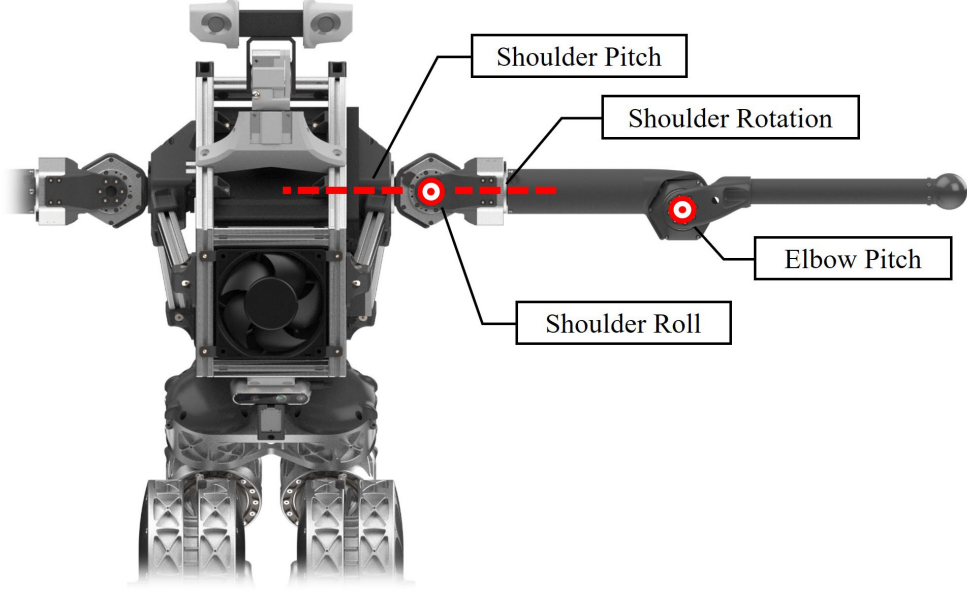


Figure 3.17: upper body joints and actuator locations.

Table 3.4: Arm Joints Specifications

	Range of motion (°)	Peak torque (Nm)	Joint Velocity (rad/s)
Shoulder pitch	-180 – 90	32	15/30*
Shoulder roll	-100 – 75	32	15/30*
Shoulder rotation	-180 – 90	32	15/30*
Elbow pitch	-176 – 0	32	15/30*

* When operated with a single battery or two batteries in series.

is located at the joint with slight offset to allow increased elbow flexion range of motion so that the end effector could touch the shoulder.

In order to minimize the weight of the design, carbon fiber tubes are used as the structural members of the arm. One end of the carbon fiber tube has been bonded onto the structure with epoxy, while the other end of the tube is fixed with fasteners on the perimeter. Spherical rubber balls are used as end effectors, since there is no wrist degree of freedom. Mounting features are designed at the wrist for future possible hand or end effector designs.

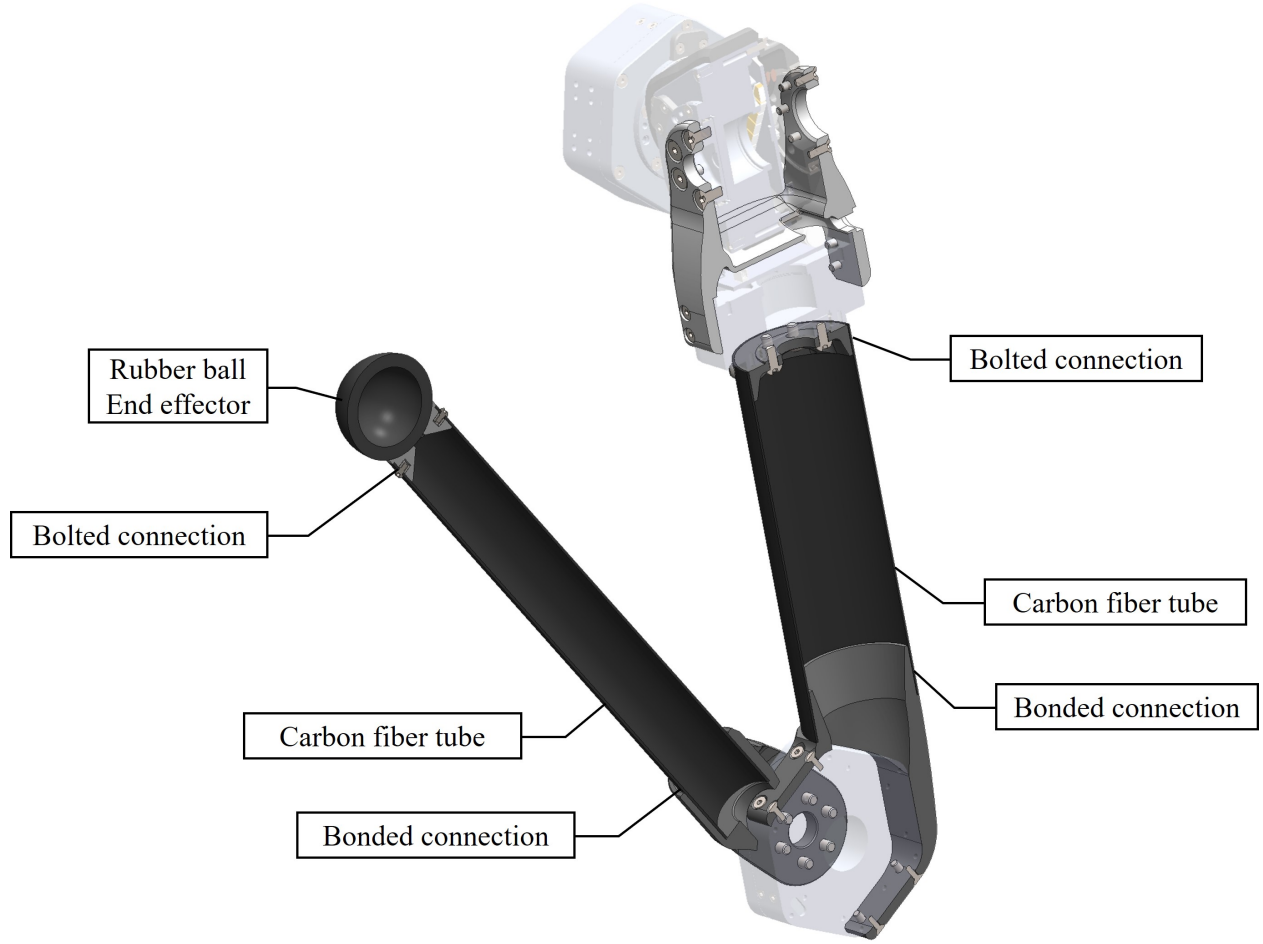


Figure 3.18: Cross section of arm structures.

3.4 Head Design

For the head design of the robot, focus has been on how to better support the sensors required for localization. An integrated stereo camera sensor with inertia measurement unit was chosen for its compactness and the ability to utilize visual simultaneous localization and mapping (vSLAM).

A pan and tilt two degree of freedom neck design has been adopted for its simplicity. For better visibility of the environment, the neck has been pushed towards front of the robot. When the head tilts down, the ground environment adjacent to the feet are fully visible with the stereo camera.

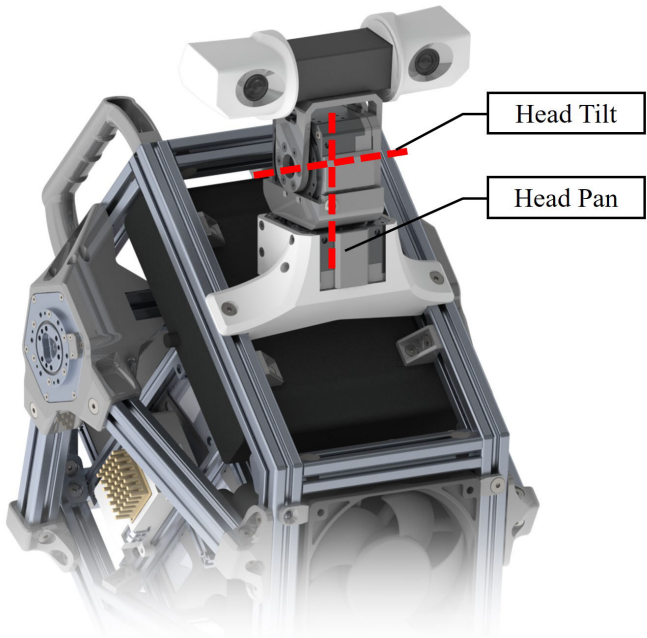


Figure 3.19: Head joints and actuator locations.

CHAPTER 4

System Design

The proposed robot has been named ARTEMIS, after the Greek goddess of hunt and nature. ARTEMIS is also an acronym for Advanced Robotic Technology for Enhanced Mobility and Improved Stability.

Table 4.1: ARTEMIS Robot Specification

Degrees of Freedom	20
	5 DoF per leg
	4 DoF per arm
	2 DoF neck
Height	1.42m
Weight	37kg
Battery	4x 100Wh Lithium battery
Sensors	ZED 2 stereo camera
	2x Intel RealSense D435i
	Microstrain CV7 IMU
	Custom foot loadcell

4.1 Sensors

A wide array of sensors is used to measure and estimate the robot states, contact information as well as global position relative to the world. In addition to the joint current sensors and joint angle encoders, the main sensors being used are stereo vision camera, inertial

measurement unit (IMU) and contact force sensors at the feet.

4.1.1 Cameras

Stereo vision camera is chosen over LiDAR for its relatively affordable pricing and robustness over indoor and outdoor environments. ZED 2 from Stereolabs has been selected for its wide field of view (FoV), integrated IMU and complete SDK with depth sensing, positional tracking and object detection. ZED 2 is mounted on the head of the robot with pan and tilt 2-DoF neck joints for positioning the camera.



(a) Stereolabs ZED 2



(b) Intel RealSense D435i

Figure 4.1: Cameras used on ARTEMIS.

In addition to the ZED 2 camera, two Intel RealSense D435i are provisioned to be mounted at both front and back of the robot, providing high-fidelity ground information near the robot.

4.1.2 Inertial Measurement Unit

IMU is a critical sensor for being able to balance and walk stably. A typical IMU sensor includes both 3-axis accelerometer and 3-axis gyroscope. Optionally, triaxial magnetometer is also included for true-north reference, often referred to as attitude and heading reference system (AHRS). Microelectromechanical system (MEMS) based IMU 3DM-GX5 from Parker LORD Microstrain was initially selected for its size and price point. Compared to fiber optic gyroscope (FOG) based IMU, MEMS sensors are much smaller and lower cost, but typically with worse noise and bias-stability performance. As MEMS based IMU rapidly progressing, we switched to MicroStrain 3DM-CV7 tactical grade IMU and its performance is approaching

Table 4.2: Stereolabs ZED 2 camera specifications

ZED 2	
Baseline	120mm
Field of View	110°(H) x 70°(V) x 120°(D) 2208x1242 @15fps
Stereo Output	1920x1080 @30fps
Resolution	1280x720 @60fps 672x376 @100fps
Depth Range	0.3m to 20m
Depth Accuracy	< 1% up to 3m < 5% up to 15m
Embedded Sensors	Gyroscope, Accelerometer, Magnetometer, Barometer, Temperature

Table 4.3: Intel RealSense D435i camera specifications

D435i	
Baseline	50mm
Depth Field of View	87°(H) x 58°(V) x 95°(D)
Depth Output	1280x720 @30fps
Resolution	848x480 @90fps
Depth Range	0.2m to 3m
Depth Accuracy	2% up to 2m
Color Field of View	69°(H) x 42°(V) x 77°(D)
Color Output	1920x1080 @30fps
Resolution	1280x720 @30fps 960x540 @60fps
Embedded Sensors	Gyroscope, Accelerometer, Temperature

that of FOG.

The Microstrain series IMU have built-in Extended Kalman Filter (EKF) for fusing acceleration and angular rate data, producing attitude and heading data. In practice,

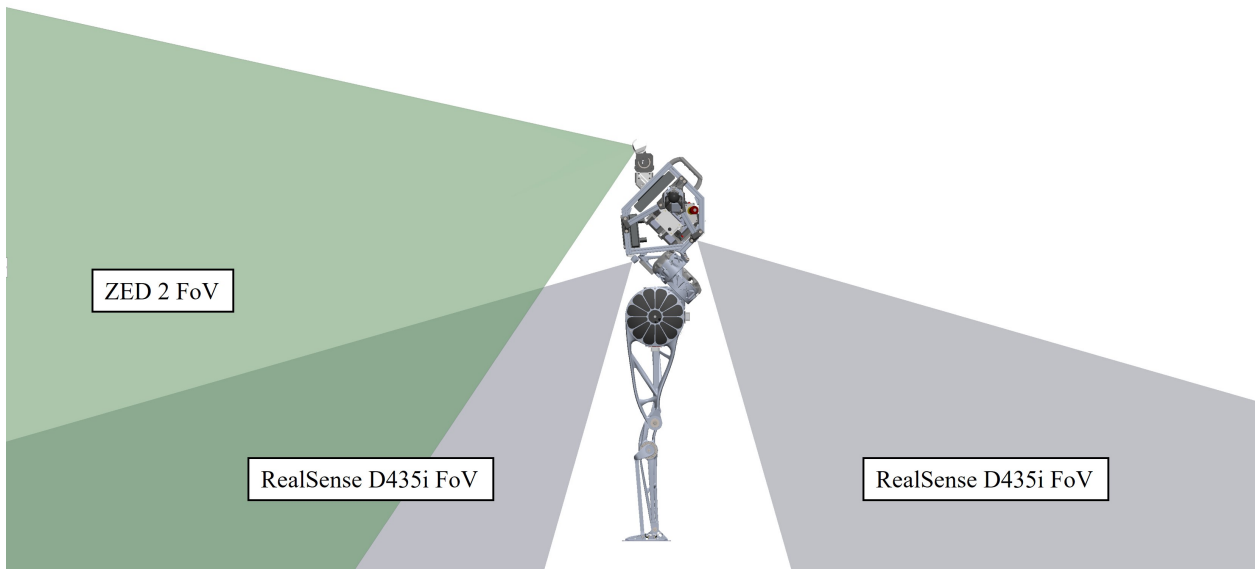


Figure 4.2: Camera field of view.



Figure 4.3: Microstrain IMUs.

magnetometer-based heading reference was ignored due to large amounts of hard and soft iron interference. Heading data has been purely gyro-based and would rely on external sensor such as camera or Global Navigation Satellite System (GNSS) for heading compensation.

As shown in fig. 4.4, a side-by-side comparison between 3DM-GX5 and 3DM-CV7 also revealed that the new generation sensor has lower latency, which contributes to the better

Table 4.4: IMU Specification Comparison

	3DM-GX5	3DM-CV7
System Performance		
Roll, Pitch (static, °)	0.25	0.25
Heading (static, °)	0.8	0.5
Data Rate (Hz)	500	1000
Gyroscope		
Bias Instability (°/h)	8	1.5
Noise Density (°/h/ \sqrt{Hz})	18	8.5
Bias Error Over Temperature	0.04%	0.03°/s
Gain Error Over Temperature	0.03%	0.1%
Accelerometer		
Bias Instability (μg)	40	18
Noise Density ($\mu g/\sqrt{Hz}$)	20(2g)	30
Bias Error Over Temperature	0.06%	0.75mg
Gain Error Over Temperature	0.03%	0.06%

accuracy of the state estimator.

4.1.3 Foot Sensor

For traditional humanoid systems, 6-axis force torque (F/T) sensor have been used for ground reaction force and contact state feedback. However, they are often fragile and could not handle large impact or over-load.

As a result, custom foot sensor has been designed for the specific task. The goal is to design a robust foot sensor that can reliably detect ground contact. Instead of full 6-axis force and torque sensing, the custom foot sensor can only measure two perpendicular ground reaction forces which are located at the heel and toe of the foot.

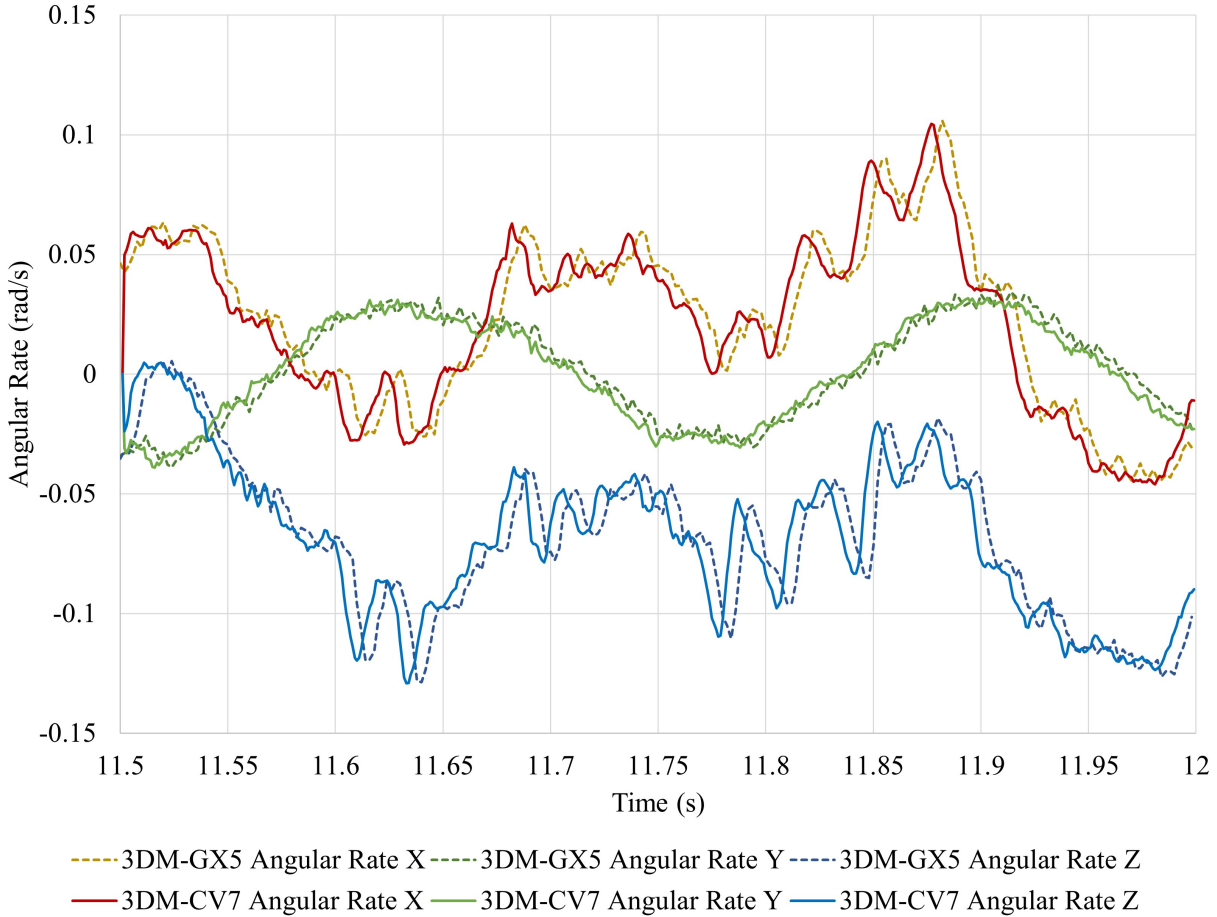


Figure 4.4: IMU data comparison.

In order to have more robust force sensing, displacement-based measurement is used instead of strain gauges. Two cantilevered beams are machined into the aluminum foot's heel and toe. Displacements are then measured using hall-effect linear encoders with 0.4um resolution. The measured values are then collected and returned to the computer with the same RS-485 data bus as all the actuators.

For over-load condition protection, retention features are machined with wire EDM as part of the beam. When force exceeds the allowable range of the cantilevered beam, the flexure would simply bottom out on the retention feature, preventing it from breaking.

Compared to F/T sensors, such custom design trades robustness with accuracy, since the resolution of the sensor is much lower than the F/T sensor. This is however worthwhile

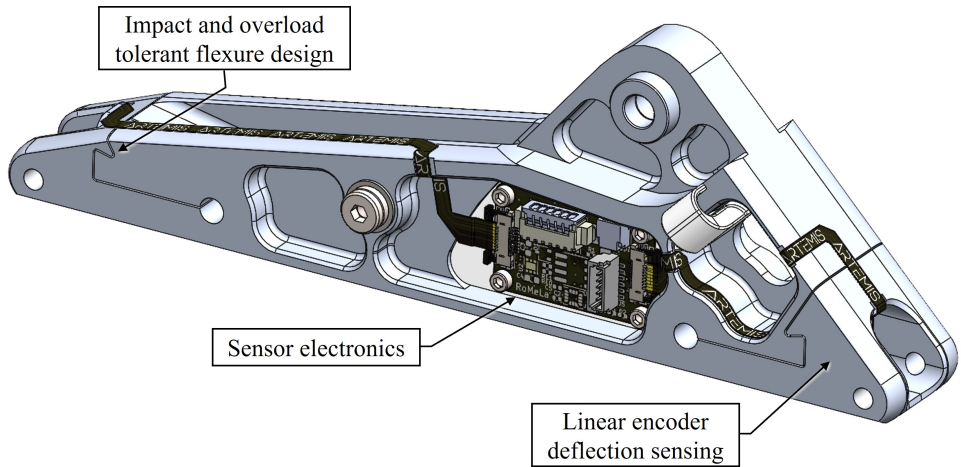
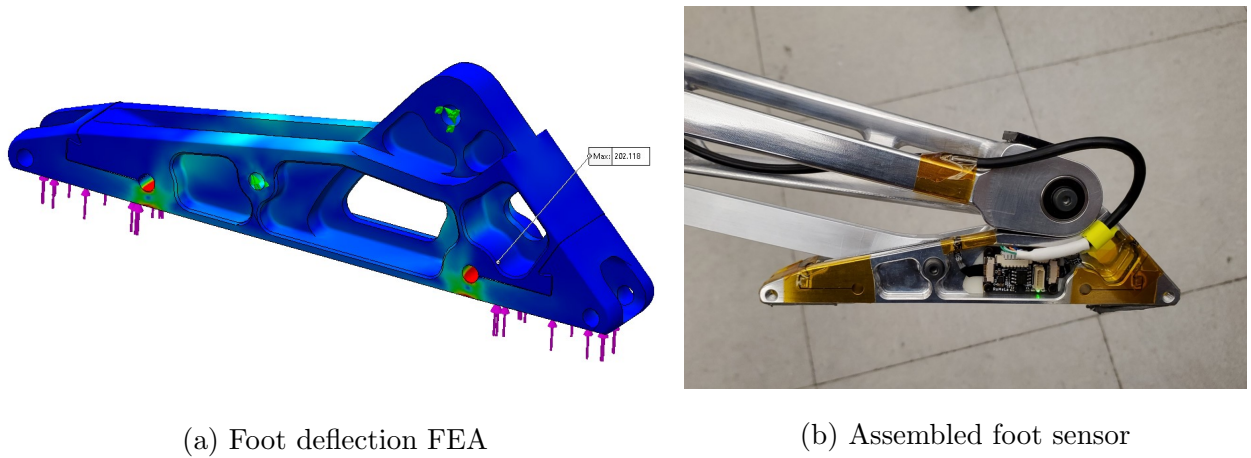


Figure 4.5: Foot with custom sensor.



(a) Foot deflection FEA

(b) Assembled foot sensor

Figure 4.6: Foot sensor analysis and assembly.

because the exact force values are not being used as part of the feedback, instead a set threshold with hysteresis has been used to determine the robot ground contact status.

As an additional sensor, a 6-axis IMU is also included on the integrated foot sensor PCB. Gyroscope and accelerometer data can be used to further enhance the state estimator performance, or to aid touch down sensing for future research.

4.2 Computer

In order to leverage modern optimization-based control algorithms, high performance yet compact computer hardware is required. Nvidia graphics processing unit(GPU) is also required due to ZED 2 camera needing Nvidia CUDA Toolkit for stereo vision as well as visual simultaneous localization and mapping(vSLAM) processing.

Based on past experience, Intel Next Unit of Computing(NUC) was the go-to choice of computer hardware to be mounted on the robot platforms. Intel NUC are often the most compact hardware for its performance and closely resembles a laptop without the screen, keyboard and battery. For this reason, Intel NUC11PHKi7C was initially selected as the main computer for the robot platform. The NUC utilizes a 11th Gen Intel processor with 4 cores and 8 threads together with NVIDIA Geforce RTX 2060 GPU.



Figure 4.7: Alternative computer options.

However, during the course of the project, faster and more capable computer hardware have come out and it is decided that HP Elite Mini 800 G9 would be used instead. The Elite Mini is a series of ultra-compact desktop computer, the specific model chosen is equipped with 12th Gen Intel processor with 12 cores and 20 threads, as well as NVIDIA Geforce RTX 3050 Ti graphics processor.

As an added benefit, each year's new Elite Mini would have the same general form factor

and mounting feature, making it possible to easily upgrade the computer down the line.

Table 4.5: Computer Specification Comparison

	Intel NUC11PHKi7C	HP Elite Mini 800 G9
CPU	Intel Core i7-1165G7	Intel Core i7-12700T
Total Cores/Threads	4/8	12/20
Max Turbo Frequency	4.7GHz	4.7GHz
Memory Types	2x DDR4-3200	2x DDR5-4800
Memory Size	32GB	32GB
GPU	NVIDIA RTX 2060	NVIDIA RTX 3050 Ti
Weight	1.4kg	1.4kg

4.3 Electronics

Tailored towards the system, a series of electronics modules have been developed. All power electronics including battery and power management systems are fully custom to satisfy the power density requirements.

4.3.1 Battery

Custom lithium battery pack has been designed out of necessity. Previous robots that are developed in the lab utilizes RC car or drone lithium batteries for their excellent power density and availability. The downside of using such batteries is that they do not have built-in protection and requires specialized charger for charging and balancing the cells.

For the safety of the robot and operators, the first requirement of the battery pack design is to have built-in safety protections against over-current, over-voltage, under-voltage and over-temperature conditions. Integrated battery state of charge monitoring and charger charging control allows for much easier user experience. Battery packs are designed to be



Figure 4.8: Custom RB56100 lithium battery.

easily swappable and not charged on the robot because lithium batteries are often the most dangerous when it is charging. For international airline travel purposes, each individual battery pack is designed to be under the 100Wh FAA limit.

For the battery cells, off the shelf drone batteries are purchased and repackaged to fit the battery management system (BMS) PCB. The BMS constantly monitors the cell voltage, current and temperature to ensure battery safety and functionality. The battery pack uses the industry standard SMBus 1.1 protocol for communication with the robot or the charger.

Custom receptacles for the battery pack are designed for ease of use and compatibility. Samtec EXTreme LPHPower connectors are chosen for the battery pack power and signal.

Accompanying battery charger has been designed to provide seamless charging experience. When using traditional drone batteries, charging voltage and current needs to be manually adjusted, which is tedious and prone to human error. With both the battery and the charger being SMBus compliant, all charging parameters can be negotiated automatically without any user intervention.

For the robot system, a total of four battery modules are designed to be mounted within the torso of the robot. Depending on the use case, battery modules can be connected

Table 4.6: Battery module Specification

RB56100	
Battery chemistry	LiCoO ₂
Cell in Series	6
Nominal Voltage	22.2V
Rated Capacity	4500mAh
	99.9Wh
Maximum Discharge Rate	10Sec @90A 2Sec @150A
Weight	650g



Figure 4.9: Custom SMBus compliant battery charger.

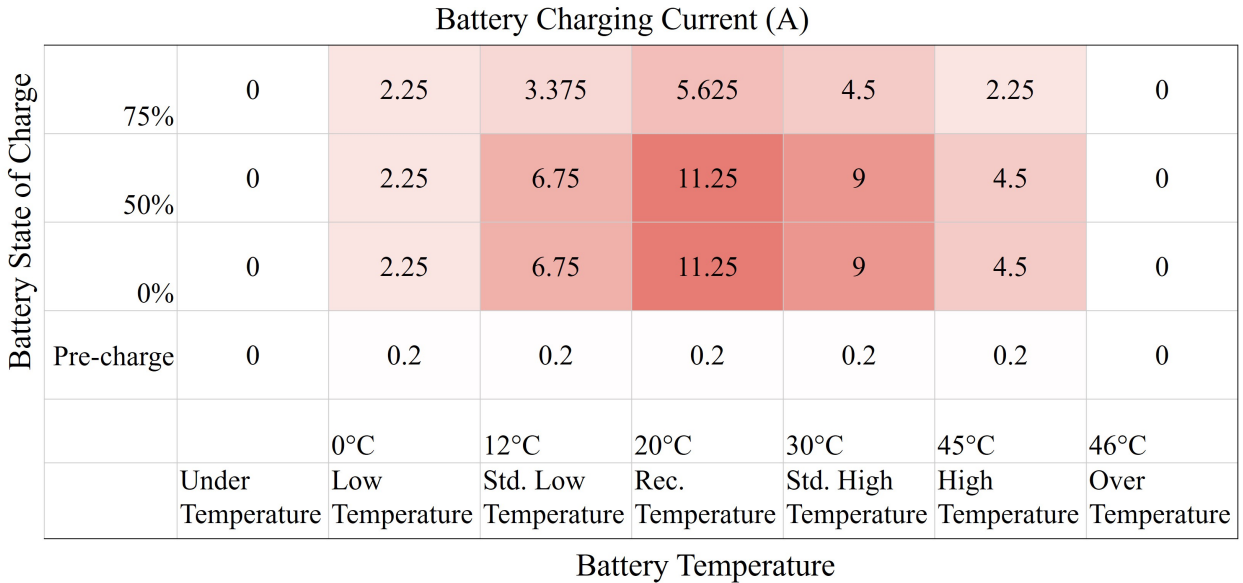


Figure 4.10: Battery charging current based on SoC and temperature.

in series to double the voltage, in turn increase the velocity of the actuators. A typical configuration consists of one battery module for the computer, one battery module for upper-body actuators and one or two modules for lower-body actuators.

4.3.2 Wireless E-Stop

Emergency stop buttons are critical safety devices that all autonomous machines should be equipped with. E-Stops are used to de-energize the system, ensuring operator's safety. In the context of mobile robots, E-Stops often need to be remotely controlled since the operator cannot always be within the vicinity of the robot.

A custom wireless emergency stop system has been developed to quickly de-energize the robot at a safe distance. The wireless E-Stop system consists of two main parts, the receiver that resides on the robot and the transmitter that the operator holds onto.

The receiver power input connects directly to the battery and the main output is connected to all the actuators. At idle, main output is disconnected from power via high-side MOSFET switch. When E-Stop button is reset, main output switches on and actuators are

initialized.

Due to the back-drivable nature of the actuators, if the power is cut when the robot is standing, it would collapse under gravity and potentially damage the robot itself. Similarly, if the robot joints are moving at some significant velocity, cutting the power would not apply brake to the joints. For this reason, a secondary button has been added to the transmitter and when the button is pressed, all actuators would apply three-phase short across all windings, effectively putting the actuators into a safe damping mode. Energy is dissipated through winding as heat and there would be much lower chance of damaging the robot itself.

The transmitter and receiver communicates with off-the-shelf XBee wireless transceiver modules, which offers either 2.4GHz or 900MHz transmission. Low-level wireless protocols as well as message encryption are handled by the XBee firmware.

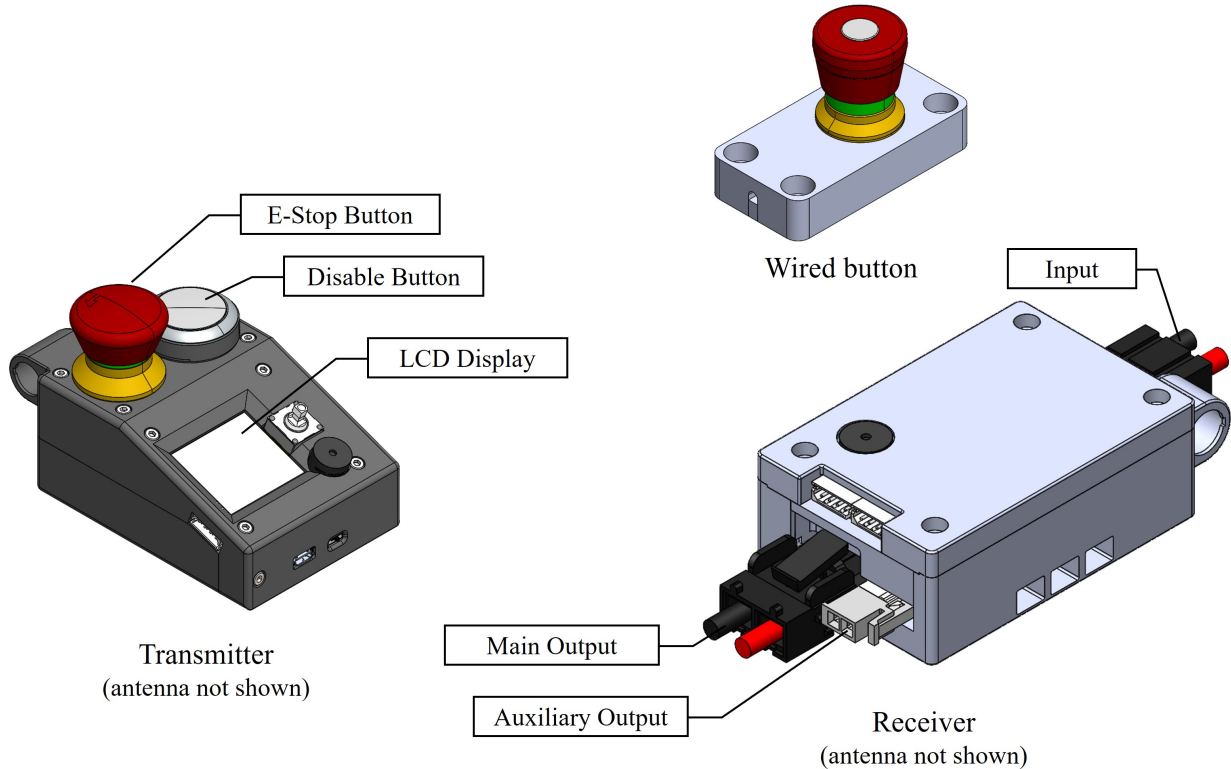


Figure 4.11: Wireless E-Stop system.

An added benefit of custom E-Stop module and battery is that the E-Stop firmware can read battery status whenever the batteries are plugged in. As a result, E-Stop transmitter

screen also displays all battery information. When the batteries are low, the E-Stop module would also alert the operator and eventually cut power to save on battery.

Special attention has been put into the transmitter electronics design for low-power operation. The transmitter uses STM32L4 ultra-low-power microcontroller that is put into sleep mode at idle. The microcontroller as well as the XBee transceiver only wake up at certain intervals or with interrupt when buttons are pressed. Sharp memory-in-pixel LCD screen has been used to minimize the screen power consumption. As a result, the transmitter can last months without changing the three on-board AA batteries.

4.3.3 DC-DC Converter

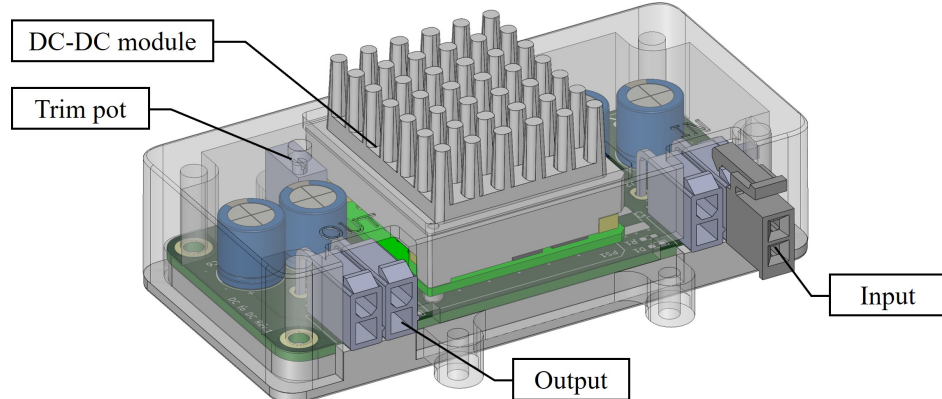


Figure 4.12: DC-DC Converter.

DC-DC converters are required to provide the computer with 19.5V power. The converter module is designed to take advantage of the “1/16th Brick” standardized power modules. 200W buck converter module with adjustable output range and heatsink has been used to convert battery voltage to stable computer input voltage.

4.3.4 USB to RS-485 Adapter

In order to communicate with the actuators, an adapter is required to convert RS-485 serial data to and from the USB bus. From early on, it is recognized that the conversion between

USB and RS-485 could become the communication bottle neck. FTDI FT232H USB to serial conversion chip has a minimum latency timer of 1ms. Meaning for each data packet, the chip would hold incoming data in a buffer before the 1ms timer elapses and then transmits back to the computer. This would mean the communication between the PC and the actuators can not reliably reach 1kHz, which is the target communication rate.

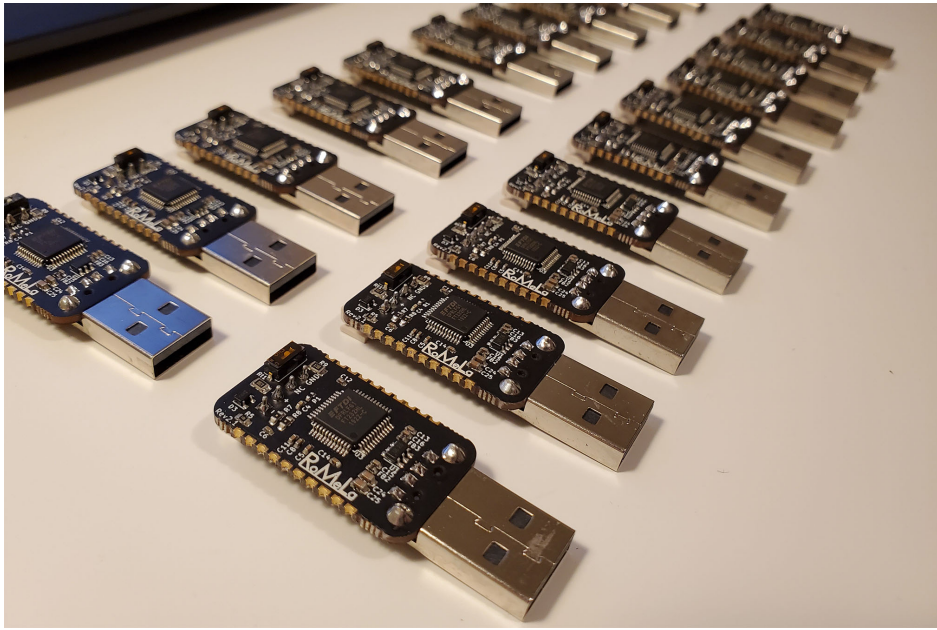


Figure 4.13: Custom USB to RS-485 converter.

Custom USB to RS-485 adapter has been developed for this specific reason. An on-board microcontroller constantly monitors the outgoing and incoming messages. When the microcontroller detects an end of a return packet, it will signal the FT232H conversion chip to immediately return all buffered data. Tests show that for individual actuator communication, data rate can reach 8kHz, which is the minimum time frame for USB communication. By utilizing bulk read and write commands, 12 actuator lower body communication can reliably be done at over 1kHz.

Communication latency test has been conducted comparing off-the-shelf USB adapter to the custom adapter. From the histogram shown in fig. 4.14, regular adapter averages around 1ms latency, which matches up with the aforementioned latency timer. Notice the few 2ms and 3ms data points, this points to data coming in at discretized 1ms increments. As for the

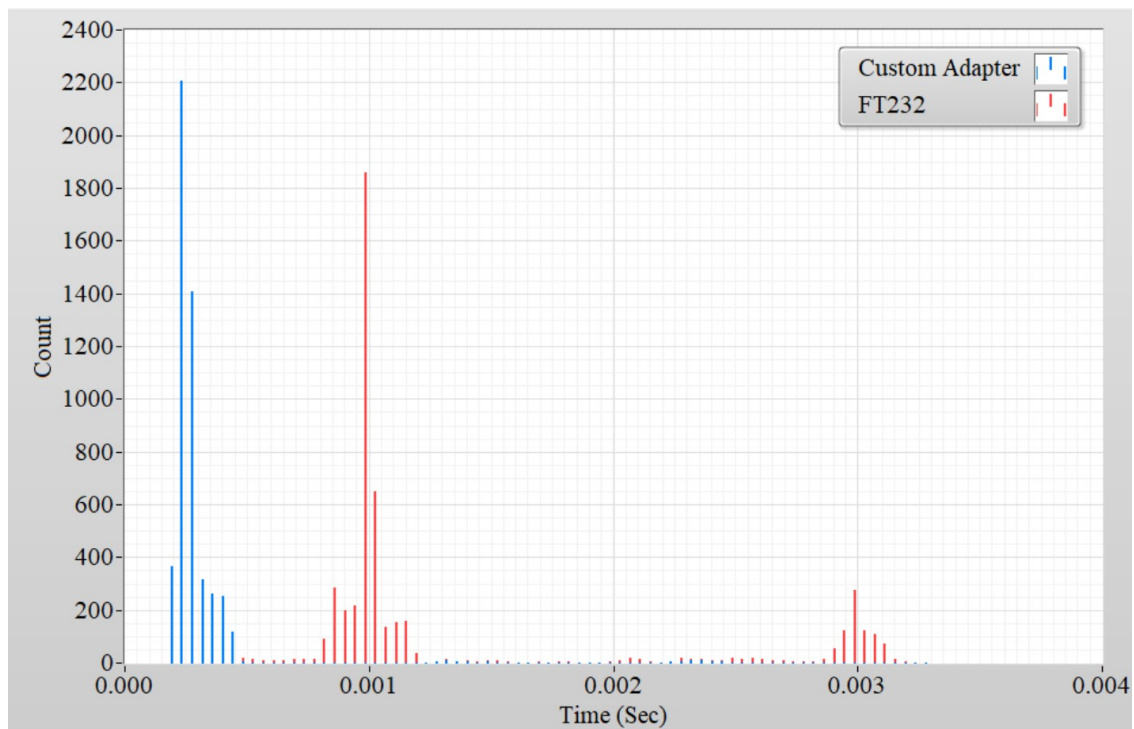


Figure 4.14: USB round trip latency comparison.

custom adapter, average communication rate approaches 8kHz and almost all data packets are returned within the 1ms window.

CHAPTER 5

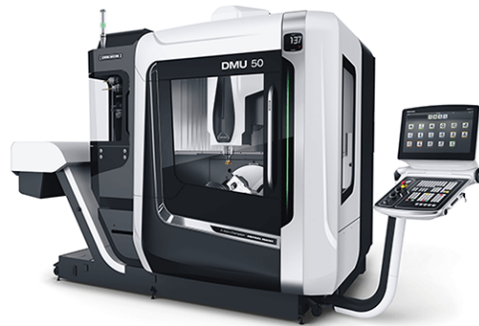
Testing and Results

5.1 Parts Manufacturing

All parts of the robot are manufactured in-house with the exception of motor windings and magnets. Custom gears have been manufactured for the actuator gearbox with wire EDM machine and all custom aluminum structures are done using 5-axis CNC milling machine. Functional prototype parts have been made with SLS nylon.



(a) GF AgieCharmilles Cut 200 SP



(b) DMG MORI DMU50

Figure 5.1: Machining equipment used for manufacturing.

Figure 5.2 illustrates how various parts are machined with the 5-axis CNC milling machine. Coolant channel caps are machined from sheet aluminum stock with fixturing around the perimeter, since they are simple 2D parts. Hip pitch structure machining involves milling out the majority of the features in the first operation and flip to the back side, finishing the coolant channels. Knee linkages can technically be machined easily on a regular 3-axis mill, using positional 5-axis ensures the absolute positional accuracy of the parts. The actuator

rotor has been machined using a technique typically known as window machining, during which the remaining stock “window” acts as the fixture, keeping the positional tolerance of the part.

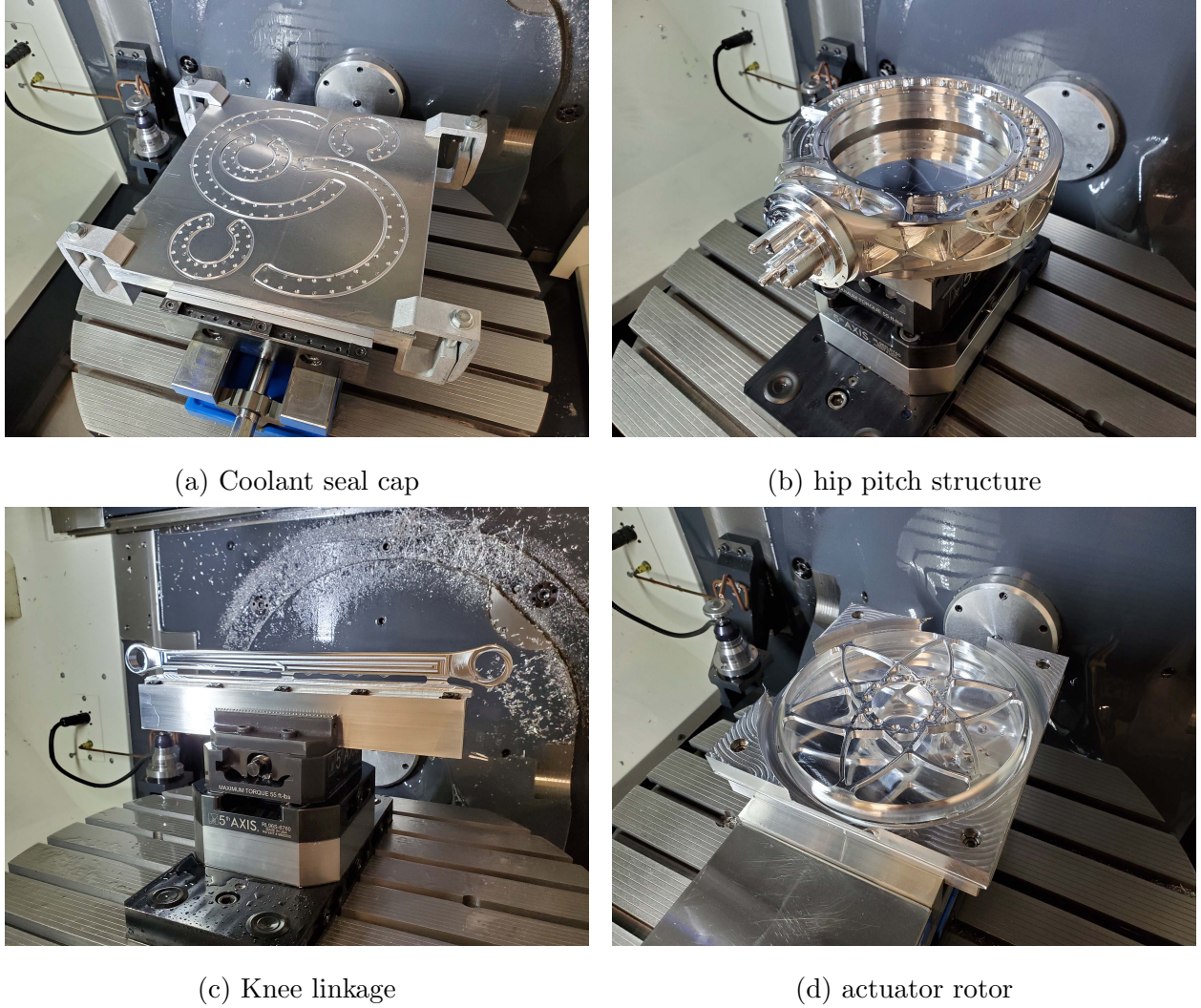


Figure 5.2: Parts being machined in CNC mill.

Figure 5.3 demonstrates the process of machining the femur structure detailed in section 3.1. Since it is an entirely subtractive manufacturing process, the whole part was machined starting from a 17in x 8in x 5in block of 6065 aluminum that weighs over 30kg. Stock is first roughed out from all sides, leaving about 1mm material to be finished. Since the bearing arm structure was not well supported, extra care was taken to only remove material

one section at a time, reducing unwanted vibration. Finishing of the surfaces was done using ball endmill from all different orientation. Extra long stick-out tools have been used to clean out the underside of the structure. Figure 5.3d shows the stock material compared to the finished part that is only 1.1kg in weight.



(a) Initial roughing from billet stock



(b) Finishing section by section



(c) Tight clearance 5-axis tool path



(d) Finished part compared to stock

Figure 5.3: Femur structure machining sequence.

Figure 5.4 shows more structural parts that are machined on 5-axis milling machine.



(a) pelvis structure



(b) hip roll structure



(c) Knee output carrier to linkage



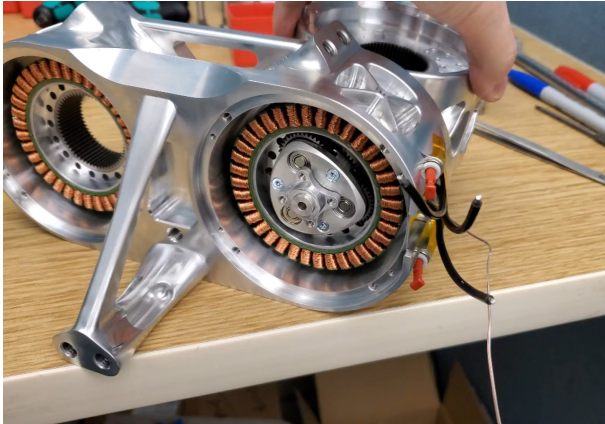
(d) hip actuator housing

Figure 5.4: Machined parts for lower body structure.

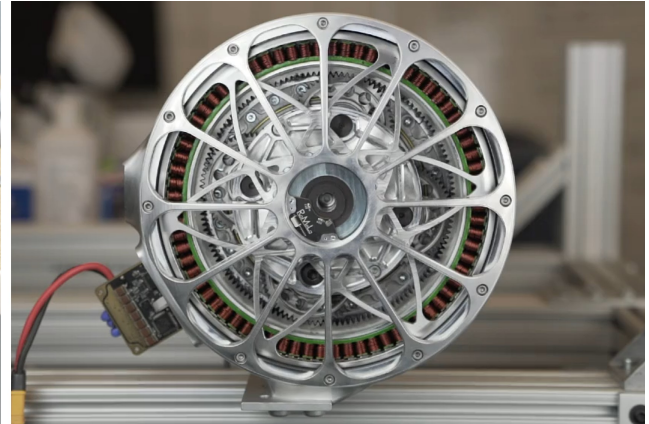
5.2 Assembly and Robot Bring-up

The robot assembly process has been done section by section, starting by assembling all actuator sub-assemblies. The difficulty has been that since the output shaft of the previous actuator is the same structural part as the next actuator, the entire leg can only be assembled in order and actuators can not be tested individually. Figure 5.5 shows partially assembled hip yaw actuator and knee actuator.

After the lower body was assembled, electronics are wired, and all motor drivers are



Assembled hip yaw actuator



Assembled knee actuator

Figure 5.5: Assembled actuators.

programed with unique motor IDs. As is typical to all mechanical systems, a certain run-in period was needed for the system to settle in. Friction in the gearbox had come down as the gears wear in and as expected, slightly larger backlash has been observed throughout the system. All motor drivers are tested for abnormal temperature rise as well as encoder sensor noise level.

Initial range of motion test has been carried out on gantry as shown in fig. 5.6.

The robot being a very intricate system, accidentally falling over can be detrimental. Various strategies have been used to protect the robot from damaging itself. As seen in fig. 5.7, shoulder and knee pads have been installed to minimize the impact from falling. As mentioned in section 4.3.2, wireless E-Stop can also put all joints of the robot into damping model, passively absorbing the impact.

5.3 Results

Walking tests have been conducted to validate the dynamic performance of the robot platform. A state estimator has been implemented to estimate the center of mass position, velocity, orientation, angular rate and angular momentum about the stance foot, based on the joint feedback, IMU and contact sensor states. Based on a set cadence, gait is gener-

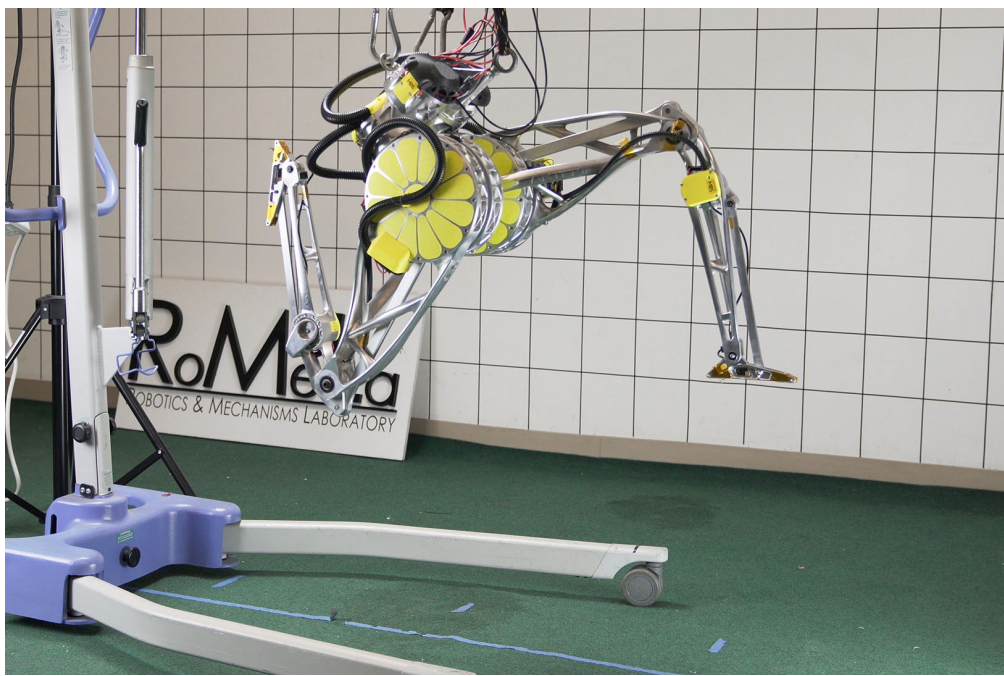


Figure 5.6: ARTEMIS lower body on gantry.

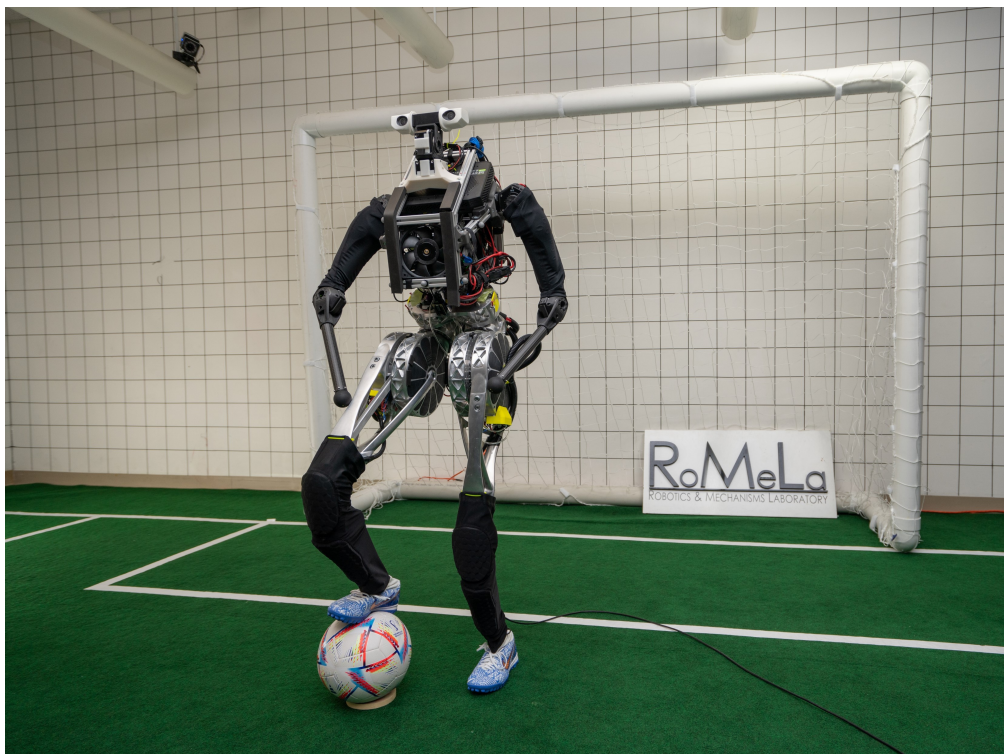


Figure 5.7: ARTEMIS with padding fitted.

ated for the left and right foot to come in contact with the ground in an alternating pattern. Based on the robot angular momentum, footstep placement is calculated to keep the robot in balance. Whole body controller is then being used to track center of mass position, velocity, orientation as well as foot position and orientation all at once.

The robot exhibits exceptional robustness when walking in place. When the robot is perturbed by external forces, it constantly changes its swing foot trajectory and foot placement so that the robot always stays dynamically stable. Figure 5.8 illustrates one second of the robot walking in 0.1s intervals.

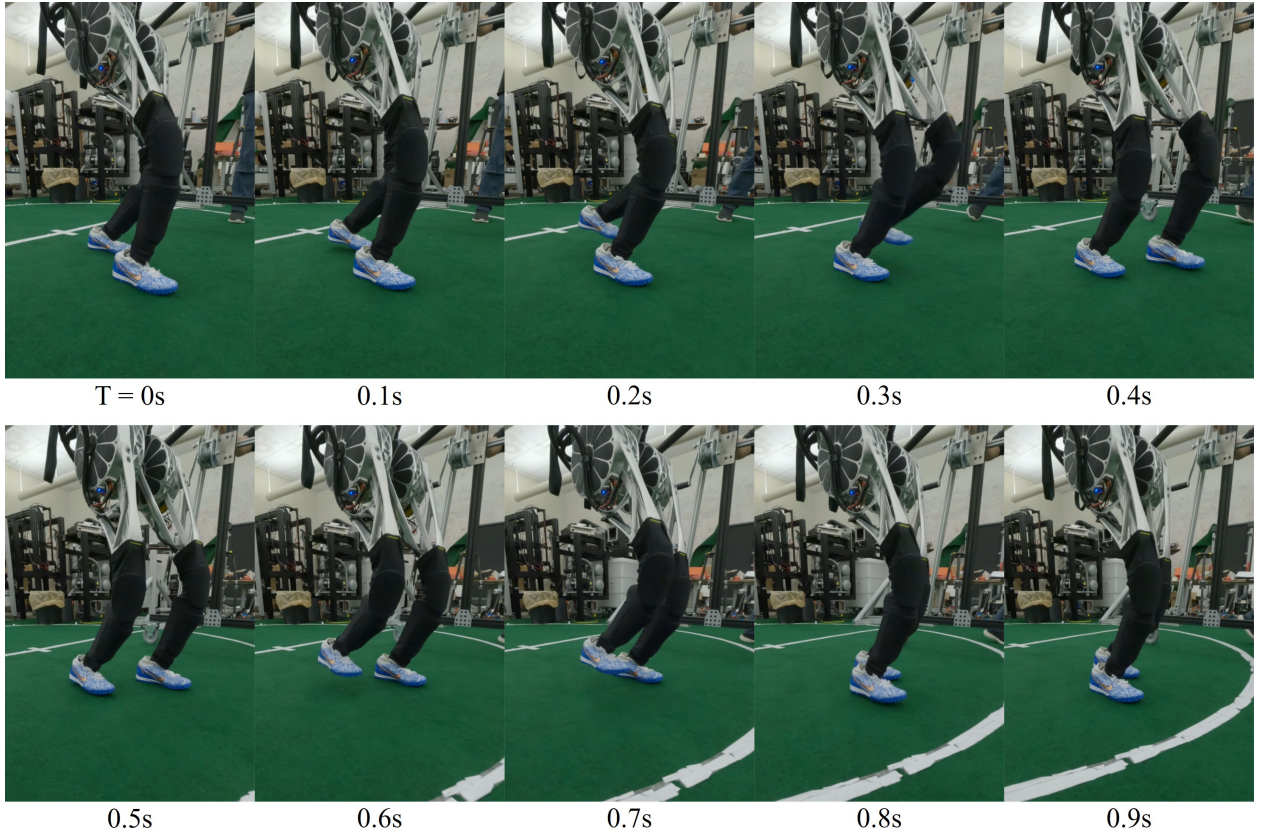


Figure 5.8: ARTEMIS walking sequence.

Figure 5.9 and fig. 5.10 shows all joints position, velocity, torque and foot contact sensor force data during a walking experiment. The robot began with stepping in place and at around 9 second mark started walking forward at 1m/s till around 16 second mark. Notice the high spike in the joint velocity graph for the ankle joints, it is likely due to the high

impact when the foot initially touches the ground.

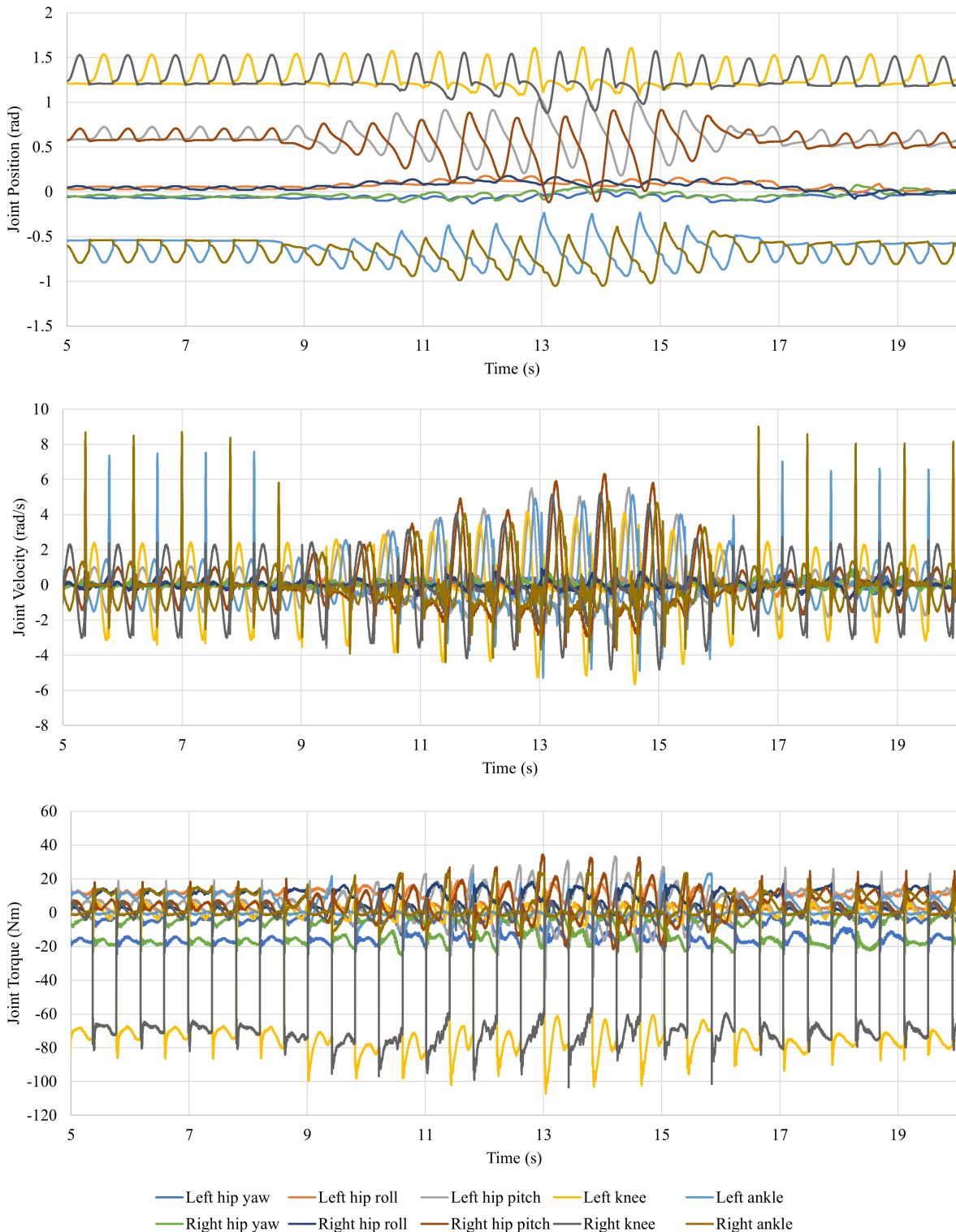


Figure 5.9: Joint position, velocity and torque during walking.

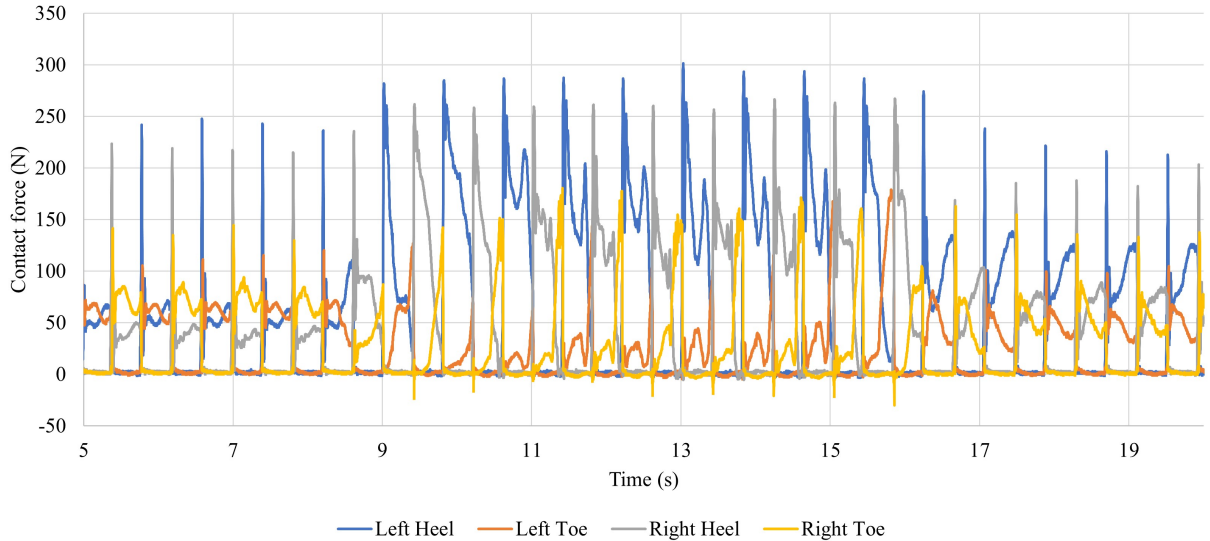


Figure 5.10: Foot contact sensor reading during walking.

The contact sensor reading shows that when the robot is stepping in place, the force is roughly even across the foot. When the robot starts to walk forward, you can clearly see the heel-toe pattern as the robot progress through the stance phase.

With no additional tuning, only by changing the step frequency and target speed, the robot can reliably walk up to 2m/s.

To really demonstrate the dynamic capability of the robot, running controller has been implemented by introducing flight phase as well as parabolic center of mass trajectories when robot is in stance phase. fig. 5.11 shows the trajectories for center of mass height as well as the vertical velocity. The slight drift of the center of mass is due to the accumulated error during the flight phase in which the robot can only rely on the on-board accelerometer for estimating the position. This can be mitigated by introducing vision sensors to correct drift. The vertical velocity graph shows how gravity is pulling the robot during the flight phase while during stance phase, the robot bounces back following the commanded trajectory. The joint torque graph indicates that even with running, it is still well within the limit of the knee actuator.

Experiment illustrated in fig. 5.12 demonstrates the robustness of the controller. The

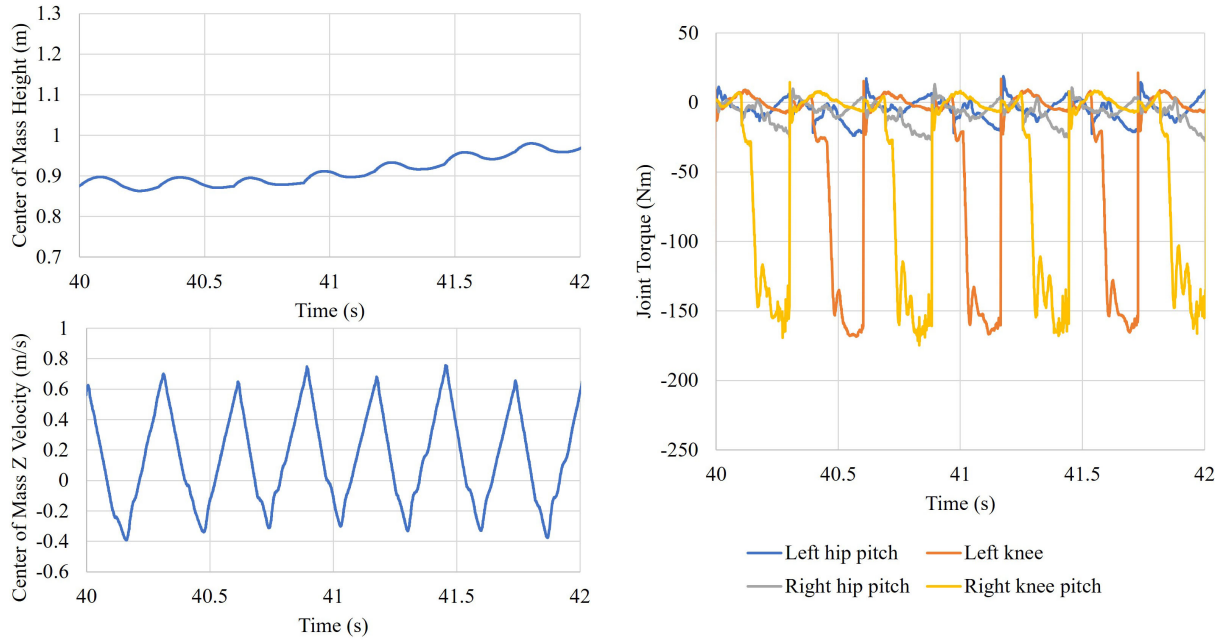


Figure 5.11: Center of Mass Height, velocity and joint torque during running.

robot was kicked from behind during right leg swing phase. Within 250ms, the robot was able to quickly react and modify the foot placement, preventing it falling over.

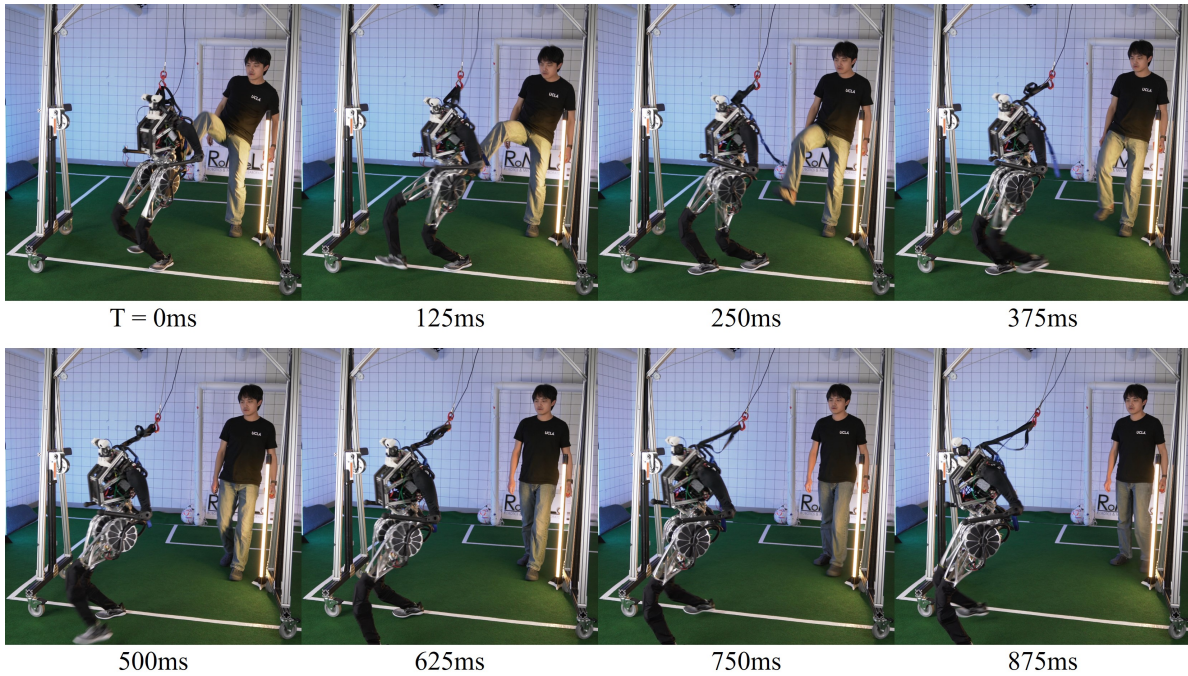


Figure 5.12: ARTEMIS kicked and recovery sequence.

Extended range walking experiments have been conducted on the third floor of Engineering IV building. The robot was untethered, with power and computer fully on-board, wirelessly controlled by the operator. Due to the narrow corridors and slippery floor surface, the robot was only able to hit its top speed in small sections of the course. The map shown in fig. 5.13 has been directly extracted from the robot state estimator. The slight yaw drift is due to vision sensor not being used and only relaying on kinematics and IMU based state estimator.

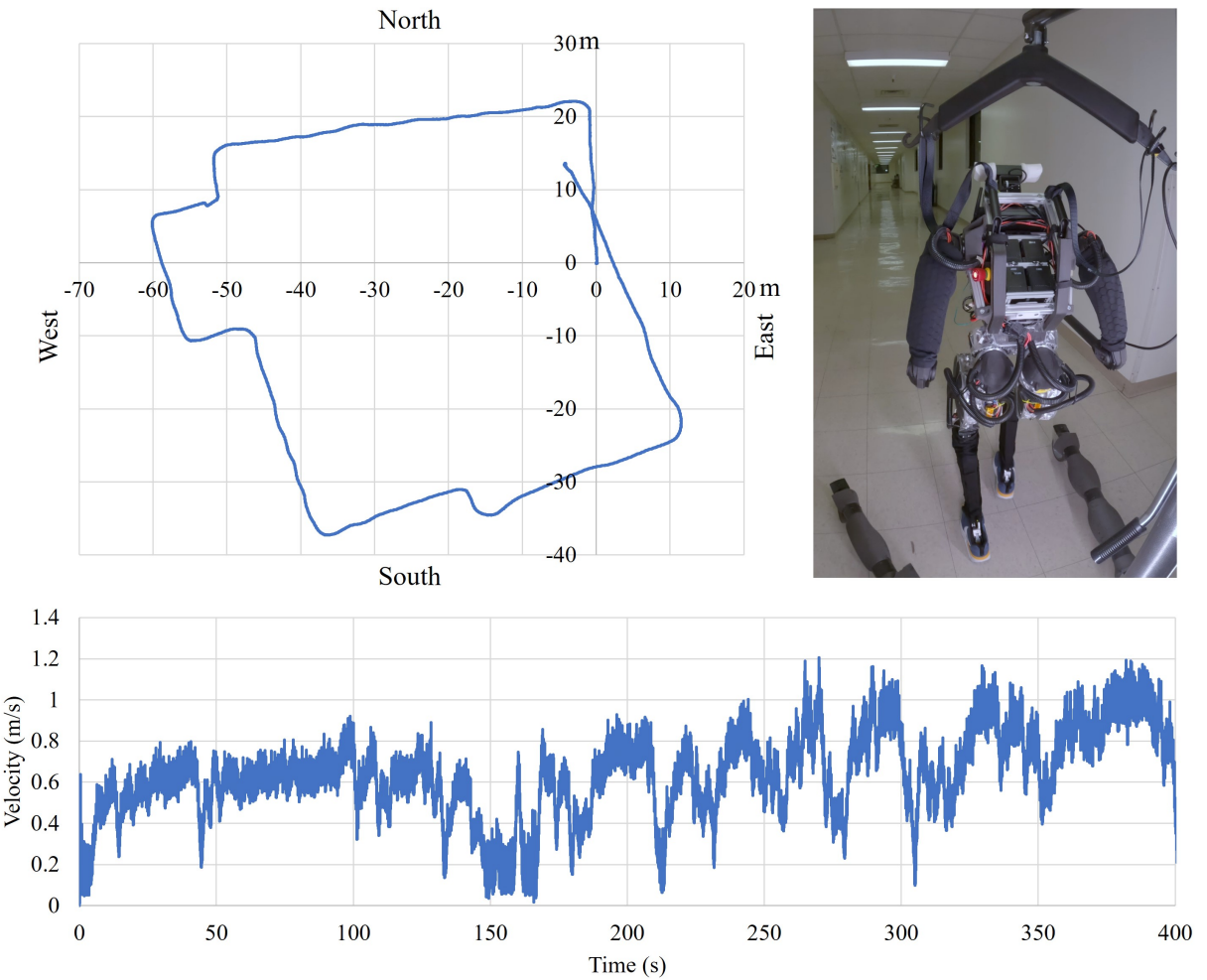


Figure 5.13: ARTEMIS walking on Engineering IV 3rd floor.

As a show case for its robust walking capability, ARTEMIS was walking outside of the lab untethered. Various terrain including pavement and grass was tested. Online video of

ARTEMIS can be accessed via <https://youtu.be/gTkupawAG6w>.

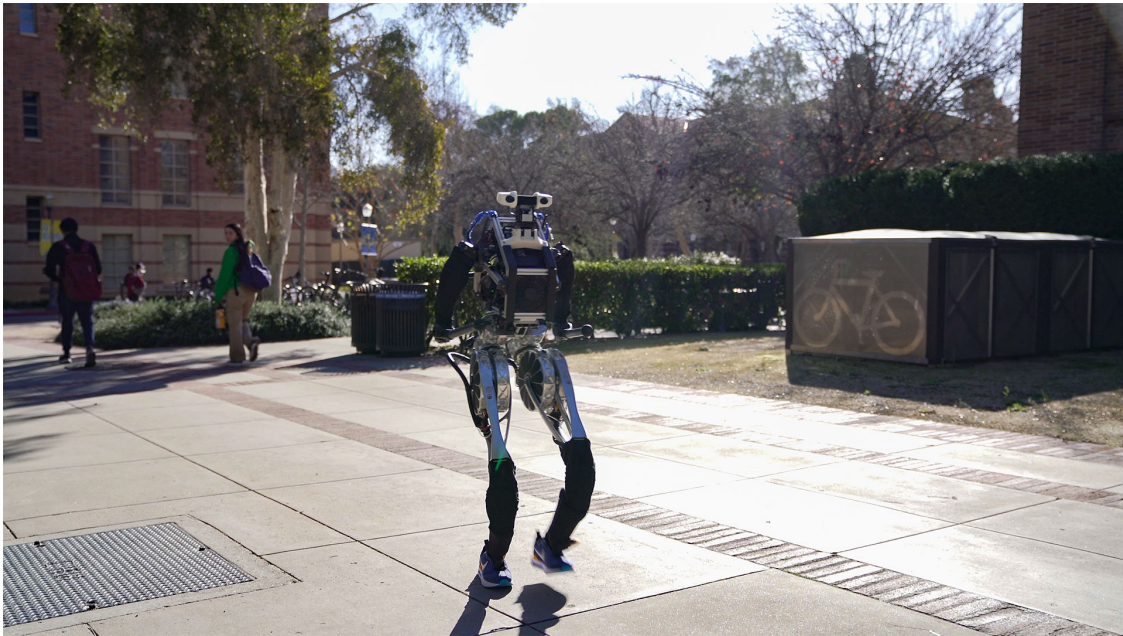


Figure 5.14: ARTEMIS untethered outdoor walking.

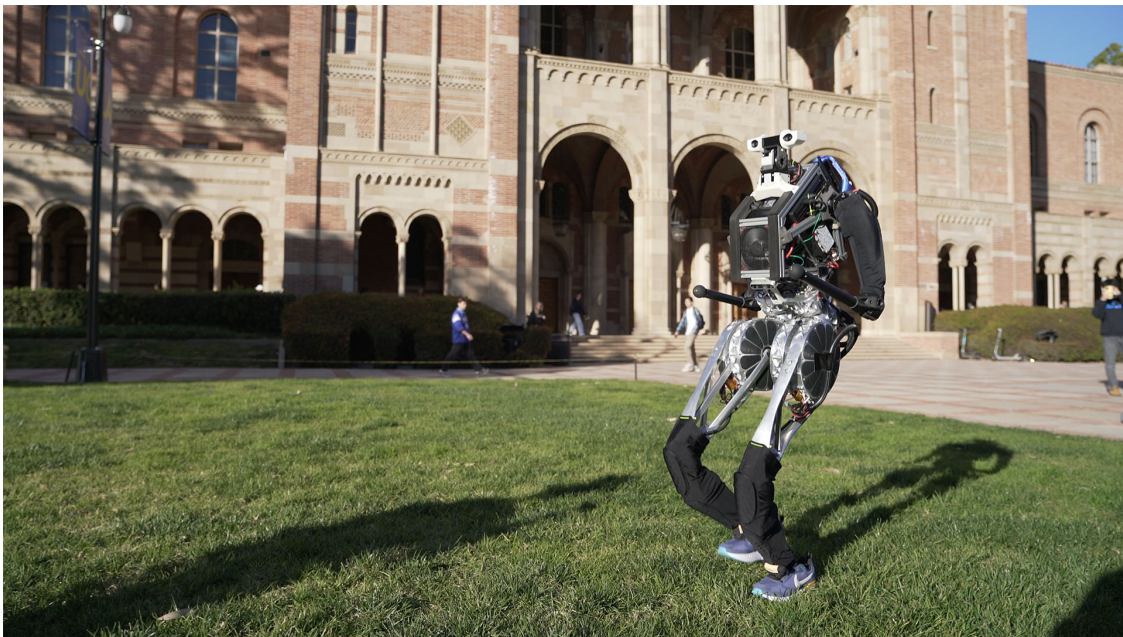


Figure 5.15: ARTEMIS untethered walking on grass.

CHAPTER 6

Conclusion and Future Work

6.1 Conclusions

In this work, based on the limitations of the current generation of robots post DARPA Robotics Challenge, we set out to design and build the next generation of highly dynamic humanoid robot that is capable of running and jumping. The goal of the research is to move away from the quasi-static, slow-moving humanoid design, to a more dynamic robotic platform that is closer to how us human walk and run.

In order to achieve this goal, it was recognized at an early stage that actuator performance is a bottleneck. The general consensus in the robotics community was that in order to achieve human level locomotion performance, compliance and force-control are needed. However, the approach of using F/T sensor as feedback for high-reduction actuators resulted in slow response and poor performance against impact. The use of series elastic actuator has proven to solve the issue of impact and compliance by modulating the apparent reflected inertia, but at the cost of bandwidth limitation.

The new-found popularity of proprioceptive actuator concept amongst the quadrupeds showed the possibility of extending similar concept to biped and humanoids. High torque density proprioceptive actuators were designed and fabricated specifically for the requirements of a humanoid robot. Different cooling methods, including liquid-cooling were explored to mitigate the over-heating issue associated with low reduction ratio.

For the lower body kinematics of the robot, thoughts were put into maximizing the range of motion while minimizing leg inertia. This was done to ensure that the robot could exhibit

dynamic behaviors and be robust against disturbance. Linkages were used to relocate knee and ankle actuators away from the joint to a more proximal position.

The torso structure was designed to house all batteries and electronics while being easy to transport. To further optimize the weight of the robot, no torso degree of freedom was included in the design. The primary focus during the design of the robot's arms was to provide counter-momentum for arm swinging during running, with manipulation not being a strict requirement. As a result, 4-degrees-of-freedom arms were designed with only ball contact as the end effector.

Stereo vision cameras as well as inertial measurement units have been equipped to provide the necessary feedback for the robot system. All systems including the computer and batteries are all onboard the robot. Custom battery packs, motor drivers and other electronics were designed to meet the specific high-performance requirements of the robot.

The entire robot was manufactured and assembled in-house. Custom motor winding and rotor magnets were commissioned. Gears used in all actuator transmissions were done by wire EDM while all structural parts are machined from aluminum billets using 5-axis CNC milling machine.

Through countless hours of testing and debugging the controllers, we achieved extremely robust untethered walking. The robot can traverse through rough terrain and walk over obstacles without requiring vision feedback, as well as withstand getting kicked and recover to a stable gait. The robot has been recorded walking at over 2m/s, making it one of the fastest humanoid robots in the world.

We further demonstrated that the robot can simply transition into running with the same underlying controller and was jogging at 1.5m/s without much further tuning. This highlights the robot's capabilities to execute highly dynamic maneuvers and moving towards the eventual goal of matching or even exceeding human capabilities.

6.2 Limitations and Future Research

While we already achieved impressive results in the one short year since the robot was built, the potential for such humanoid robot platform is near endless.

On the hardware side, the research has been solely focused on the locomotion capabilities of the robot. As a result, the torso and arm design are less refined. For a humanoid robot to be truly useful to the society, the manipulation capabilities are equally or even more important. Torso degrees of freedom can be added to increase the workspace of the robot. An actuated wrist with dexterous end effector can greatly expand the capabilities of the robot.

One notable improvement that could be made to the system is that due to manufacturing capabilities, the gearbox exhibits significant amount of backlash. This leads to worse tracking performance as well as unwanted clicking noise when the actuator reverses direction. As mentioned previously, all the gears used on the robot are custom wire EDM machined, this could be easily fixed by adjusting the tolerance, or switch to ground hardened gears.

It should be noted that even though the leg's over all backlash at the foot can be larger than 15mm due to hip and knee actuator backlash, the overall stability and robustness of the robot has not been affected. To the robot controller, any amount of leg length that is not accounted for would be analogous to unmodeled obstacle on the ground that is of similar height. From the experimental results, such amount of disturbance is clearly within the capabilities of the robot. Similarly, the relatively low stiffness of the leg can be treated by the controller as soft and bouncy floor, which it can handle without any issue.

On the controller side, with some more tuning, it is conceivable that the robot would be able to run at much higher speed. With higher speed and more time in the air, the inclusion of a model predictive controller is believed to improve the performance and robustness of the system.

With walking and running controller working, higher level controllers and more complex behaviors can be researched and implemented on the platform. So far, the stereo vision

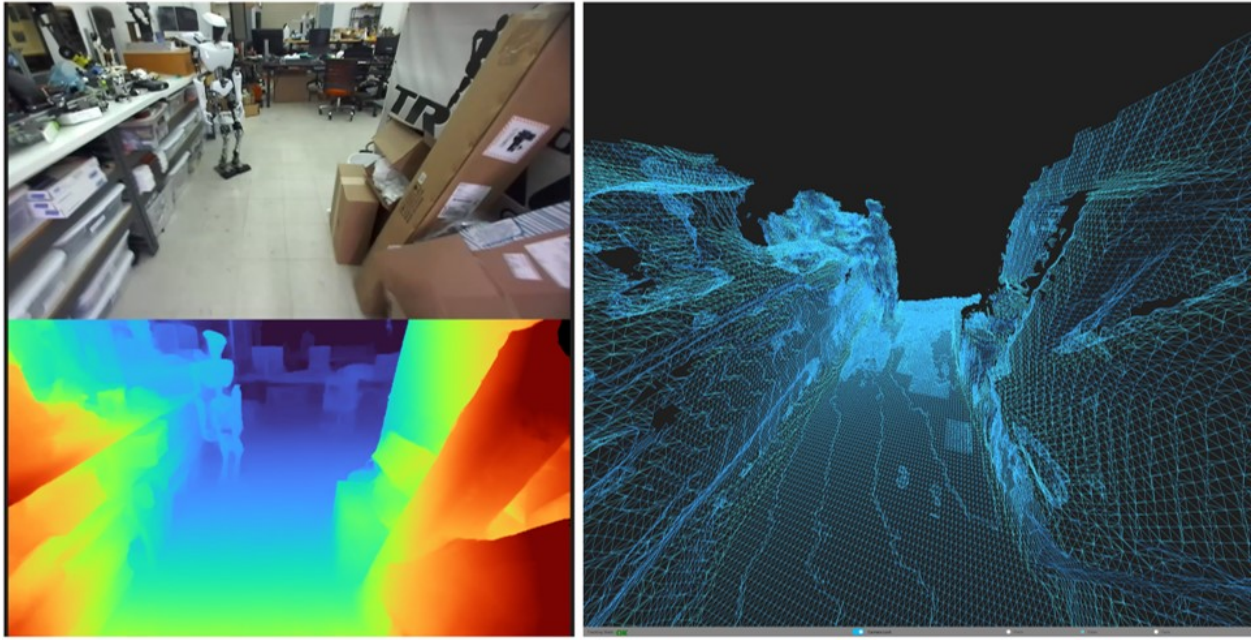


Figure 6.1: Depth data extracted from stereo image reconstructing the environment.

cameras are not being used as feedback for state estimation or localization. With the inclusion of vision, locomotion can be further improved by means of obstacle avoidance and path planning.

Figure 6.1 demonstrates the process of taking stereo video stream from the ZED 2 camera and extract depth map from it. From the depth image, 3D map of the environment can be reconstructed for further navigation and path planning.

RoboCup is an international robot soccer competition where the goal is to beat the human world champion by the year 2050. While achieving such an ambitious goal may seem distant, participating in this competition offers an opportunity to make valuable contributions to the robotics community.



Figure 6.2: ARTEMIS in soccer kicking pose.

BIBLIOGRAPHY

- [1] Andy Abate, Jonathan W Hurst, and Ross L Hatton. Mechanical antagonism in legged robots. In *Robotics: Science and Systems*, volume 6. Ann Arbor, MI, 2016.
- [2] Alessandro Acquaviva, Stefan Skoog, and Torbjörn Thiringer. Design and verification of in-slot oil-cooled tooth coil winding pm machine for traction application. *IEEE Transactions on Industrial Electronics*, 68(5):3719–3727, 2021.
- [3] Agility Robotics. Meet digit, 2023. <https://agilityrobotics.com/robots>, Last accessed on 2023-03-23.
- [4] Junhyeok Ahn, Donghyun Kim, Seunghyeon Bang, Nick Paine, and Luis Sentis. Control of a high performance bipedal robot using viscoelastic liquid cooled actuators. In *2019 IEEE-RAS 19th International Conference on Humanoid Robots (Humanoids)*, pages 146–153. IEEE, 2019.
- [5] Adamantios Arampatzis, Gert-Peter Brüggemann, and Verena Metzler. The effect of speed on leg stiffness and joint kinetics in human running. *Journal of Biomechanics*, 32(12):1349–1353, 1999.
- [6] Christopher G Atkeson, PW Babu Benzun, Nandan Banerjee, Dmitry Berenson, Christoper P Bove, Xiongyi Cui, Mathew DeDonato, Ruixiang Du, Siyuan Feng, Perry Franklin, et al. What happened at the darpa robotics challenge finals. *The DARPA robotics challenge finals: Humanoid robots to the rescue*, pages 667–684, 2018.
- [7] Gerardo Bledt, Matthew J. Powell, Benjamin Katz, Jared Di Carlo, Patrick M. Wensing, and Sangbae Kim. Mit cheetah 3: Design and control of a robust, dynamic quadruped robot. In *2018 IEEE/RSJ International Conference on Intelligent Robots and Systems (IROS)*, pages 2245–2252, 2018.
- [8] Boston Dynamics. AtlasTM, 2023. <https://www.bostondynamics.com/atlas>, Last accessed on 2023-03-23.
- [9] Johannes Englsberger, Alexander Werner, Christian Ott, Bernd Henze, Maximo A Roa, Gianluca Garofalo, Robert Burger, Alexander Beyer, Oliver Eiberger, Korbinian Schmid, et al. Overview of the torque-controlled humanoid robot toro. In *2014 IEEE-RAS International Conference on Humanoid Robots*, pages 916–923. IEEE, 2014.
- [10] Yaohui Gai, Mohammad Kimiabeigi, Yew Chuan Chong, James D Widmer, Xu Deng, Mircea Popescu, James Goss, Dave A Staton, and Andrew Steven. Cooling of automotive traction motors: schemes, examples, and computation methods. *IEEE Transactions on Industrial Electronics*, 66(3):1681–1692, 2018.
- [11] Erico Guizzo and Evan Ackerman. The hard lessons of darpa’s robotics challenge [news]. *IEEE Spectrum*, 52(8):11–13, 2015.

- [12] Clinton G Hobart, Anirban Mazumdar, Steven J Spencer, Morgan Quigley, Jesper P Smith, Sylvain Bertrand, Jerry Pratt, Michael Kuehl, and Stephen P Buerger. Achieving versatile energy efficiency with the wanderer biped robot. *IEEE Transactions on Robotics*, 36(3):959–966, 2020.
- [13] Michael A. Hopkins, Stephen A. Ressler, Derek F. Lahr, Alexander Leonessa, and Dennis W. Hong. Embedded joint-space control of a series elastic humanoid. In *2015 IEEE/RSJ International Conference on Intelligent Robots and Systems (IROS)*, pages 3358–3365, 2015.
- [14] Christian Hubicki, Jesse Grimes, Mikhail Jones, Daniel Renjewski, Alexander Spröwitz, Andy Abate, and Jonathan Hurst. Atrias: Design and validation of a tether-free 3d-capable spring-mass bipedal robot. *The International Journal of Robotics Research*, 35(12):1497–1521, 2016.
- [15] Yoshito Ito, Shunich Nozawa, Junichi Urata, Takuya Nakaoka, Kazuya Kobayashi, Yuto Nakanishi, Kei Okada, and Masayuki Inaba. Development and verification of life-size humanoid with high-output actuation system. In *2014 IEEE International Conference on Robotics and Automation (ICRA)*, pages 3433–3438, 2014.
- [16] Yoshito Ito, Shunich Nozawa, Junichi Urata, Takuya Nakaoka, Kazuya Kobayashi, Yuto Nakanishi, Kei Okada, and Masayuki Inaba. Development and verification of life-size humanoid with high-output actuation system. In *2014 IEEE International Conference on Robotics and Automation (ICRA)*, pages 3433–3438. IEEE, 2014.
- [17] Taejin Jung, Jeongsoo Lim, Hyoin Bae, Kang Kyu Lee, Hyun-Min Joe, and Jun-Ho Oh. Development of the humanoid disaster response platform drc-hubo+. *IEEE Transactions on Robotics*, 34(1):1–17, 2018.
- [18] Kenji Kaneko, Kensuke Harada, Fumio Kanehiro, Go Miyamori, and Kazuhiko Akachi. Humanoid robot hrp-3. In *2008 IEEE/RSJ International Conference on Intelligent Robots and Systems*, pages 2471–2478, 2008.
- [19] Kenji Kaneko, Hiroshi Kaminaga, Takeshi Sakaguchi, Shuuji Kajita, Mitsuharu Morisawa, Iori Kumagai, and Fumio Kanehiro. Humanoid robot hrp-5p: An electrically actuated humanoid robot with high-power and wide-range joints. *IEEE Robotics and Automation Letters*, 4(2):1431–1438, 2019.
- [20] Kenji Kaneko, Fumio Kanehiro, Mitsuharu Morisawa, Kazuhiko Akachi, Go Miyamori, Atsushi Hayashi, and Noriyuki Kanehira. Humanoid robot hrp-4 - humanoid robotics platform with lightweight and slim body. In *2011 IEEE/RSJ International Conference on Intelligent Robots and Systems*, pages 4400–4407, 2011.
- [21] Benjamin Katz, Jared Di Carlo, and Sangbae Kim. Mini cheetah: A platform for pushing the limits of dynamic quadruped control. In *2019 International Conference on Robotics and Automation (ICRA)*, pages 6295–6301, 2019.

- [22] Gavin Kenneally, Avik De, and D. E. Koditschek. Design principles for a family of direct-drive legged robots. *IEEE Robotics and Automation Letters*, 1(2):900–907, 2016.
- [23] Donghyun Kim, Junhyeok Ahn, Orion Campbell, Nicholas Paine, and Luis Sentis. Investigations of a robotic test bed with viscoelastic liquid cooled actuators. *IEEE/ASME Transactions on Mechatronics*, 23(6):2704–2714, 2018.
- [24] Kunio Kojima, Tatsushi Karasawa, Toyotaka Kozuki, Eisoku Kuroiwa, Sou Yukizaki, Satoshi Iwaishi, Tatsuya Ishikawa, Ryo Koyama, Shintaro Noda, Fumihiro Sugai, Shunichi Nozawa, Yohei Kakiuchi, Kei Okada, and Masayuki Inaba. Development of life-sized high-power humanoid robot jaxon for real-world use. In *2015 IEEE-RAS 15th International Conference on Humanoid Robots (Humanoids)*, pages 838–843, 2015.
- [25] Toyotaka Kozuki, Hirose Toshinori, Takuma Shirai, Shinske Nakashima, Yuki Asano, Yohei Kakiuchi, Kei Okada, and Masayuki Inaba. Skeletal structure with artificial perspiration for cooling by latent heat for musculoskeletal humanoid kengoro. In *2016 IEEE/RSJ International Conference on Intelligent Robots and Systems (IROS)*, pages 2135–2140. IEEE, 2016.
- [26] Eric Krotkov, Douglas Hackett, Larry Jackel, Michael Perschbacher, James Pippine, Jesse Strauss, Gill Pratt, and Christopher Orlowski. The darpa robotics challenge finals: Results and perspectives. *The DARPA Robotics Challenge Finals: Humanoid Robots To The Rescue*, pages 1–26, 2018.
- [27] A La Rocca, Z Xu, P Arumugam, SJ Pickering, CN Eastwick, C Gerada, and S Bozhko. Thermal management of a high speed permanent magnet machine for an aeroengine. In *2016 XXII International Conference on Electrical Machines (ICEM)*, pages 2732–2737. IEEE, 2016.
- [28] Sebastian Lohmeier, Thomas Buschmann, and Heinz Ulbrich. Humanoid robot lola. In *2009 IEEE International Conference on Robotics and Automation*, pages 775–780. IEEE, 2009.
- [29] Anirban Mazumdar, Steven J Spencer, Clinton Hobart, Jonathan Salton, Morgan Quigley, Tingfan Wu, Sylvain Bertrand, Jerry Pratt, and Stephen P Buerger. Parallel elastic elements improve energy efficiency on the steppr bipedal walking robot. *IEEE/ASME Transactions on mechatronics*, 22(2):898–908, 2016.
- [30] Yu Ogura, Hiroyuki Aikawa, Kazushi Shimomura, Hideki Kondo, Akitoshi Morishima, Hun-ok Lim, and Atsuo Takanishi. Development of a new humanoid robot wabian-2. In *Proceedings 2006 IEEE International Conference on Robotics and Automation, 2006. ICRA 2006.*, pages 76–81. IEEE, 2006.
- [31] Aiman Musa M Omer, Yu Ogura, Hideki Kondo, Akitoshi Morishima, Giuseppe Carbone, Marco Ceccarelli, Hun-ok Lim, and Atsuo Takanishi. Development of a humanoid robot having 2-dof waist and 2-dof trunk. In *5th IEEE-RAS International Conference on Humanoid Robots, 2005.*, pages 333–338. IEEE, 2005.

- [32] Nicholas Paine and Luis Sentis. Design and comparative analysis of a retrofitted liquid cooling system for high-power actuators. In *Actuators*, volume 4, pages 182–202. Multidisciplinary Digital Publishing Institute, 2015.
- [33] Ill-Woo Park, Jung-Yup Kim, Jungho Lee, and Jun-Ho Oh. Mechanical design of the humanoid robot platform, hubo. *Advanced Robotics*, 21(11):1305–1322, 2007.
- [34] Gill A Pratt and Matthew M Williamson. Series elastic actuators. In *Proceedings 1995 IEEE/RSJ International Conference on Intelligent Robots and Systems. Human Robot Interaction and Cooperative Robots*, volume 1, pages 399–406. IEEE, 1995.
- [35] Yoann Quérel, Thomas Boussey, Lauric Garbuio, Afef Kedous-Lebouc, Olivier Savinois, Jean-Claude Mipo, Sophie Personnaz, Julie Llado, and Abel Ebongue. Evaluation of an evaporative cooling solution for hybrid and electrical vehicles motors. In *2018 IEEE International Conference on Industrial Technology (ICIT)*, pages 395–400, 2018.
- [36] Nicolaus A Radford, Philip Strawser, Kimberly Hambuchen, Joshua S Mehling, William K Verheyen, A Stuart Donnan, James Holley, Jairo Sanchez, Vienny Nguyen, Lyndon Bridgwater, et al. Valkyrie: Nasa’s first bipedal humanoid robot. *Journal of Field Robotics*, 32(3):397–419, 2015.
- [37] Marc Raibert, Kevin Blankespoor, Gabriel Nelson, and Rob Playter. Bigdog, the rough-terrain quadruped robot. *IFAC Proceedings Volumes*, 41(2):10822–10825, 2008.
- [38] Marc H Raibert. *Legged robots that balance*. MIT press, 1986.
- [39] Wesley Roozing, Jörn Malzahn, Navvab Kashiri, Darwin G Caldwell, and Nikos G Tsagarakis. On the stiffness selection for torque-controlled series-elastic actuators. *IEEE Robotics and Automation Letters*, 2(4):2255–2262, 2017.
- [40] Y. Sakagami, R. Watanabe, C. Aoyama, S. Matsunaga, N. Higaki, and K. Fujimura. The intelligent asimo: system overview and integration. In *IEEE/RSJ International Conference on Intelligent Robots and Systems*, volume 3, pages 2478–2483 vol.3, 2002.
- [41] Sangok Seok, Albert Wang, Meng Yee Chuah, David Otten, Jeffrey Lang, and Sangbae Kim. Design principles for highly efficient quadrupeds and implementation on the mit cheetah robot. In *2013 IEEE International Conference on Robotics and Automation*, pages 3307–3312, 2013.
- [42] Sangok Seok, Albert Wang, David Otten, and Sangbae Kim. Actuator design for high force proprioceptive control in fast legged locomotion. In *2012 IEEE/RSJ International Conference on Intelligent Robots and Systems*, pages 1970–1975, 2012.
- [43] Matthew Spenko, Stephen Buerger, and Karl Iagnemma. *The DARPA robotics challenge finals: humanoid robots to the rescue*, volume 121. Springer, 2018.

- [44] N. G. Tsagarakis, D. G. Caldwell, F. Negrello, W. Choi, L. Baccelliere, V.G. Loc, J. Noorden, L. Muratore, A. Margan, A. Cardellino, L. Natale, E. Mingo Hoffman, H. Dallali, N. Kashiri, J. Malzahn, J. Lee, P. Kryczka, D. Kanoulas, M. Garabini, M. Catalano, M. Ferrati, V. Varicchio, L. Pallottino, C. Pavan, A. Bicchi, A. Settimi, A. Rocchi, and A. Ajoudani. Walk-man: A high-performance humanoid platform for realistic environments. *Journal of Field Robotics*, 34(7):1225–1259, 2017.
- [45] Junichi Urata, Toshinori Hirose, Yuta Namiki, Yuto Nakanishi, Ikuo Mizuuchi, and Masayuki Inaba. Thermal control of electrical motors for high-power humanoid robots. In *2008 ieee/rsj international conference on intelligent robots and systems*, pages 2047–2052. IEEE, 2008.
- [46] Daiki Wakabayashi, Qiang Yu, and Yoshmobu Nakamura. Development of the high efficiency cooling structure of the liquid immersion cooling sr motor. In *2017 IEEE 19th Electronics Packaging Technology Conference (EPTC)*, pages 1–4, 2017.
- [47] Takahide Yoshiike, Mitsuhide Kuroda, Ryuma Ujino, Yoshiki Kanemoto, Hiroyuki Kaneko, Hirofumi Higuchi, Satoshi Komura, Shingo Iwasaki, Minami Asatani, and Takeshi Koshiishi. The experimental humanoid robot e2-dr: A design for inspection and disaster response in industrial environments. *IEEE Robotics & Automation Magazine*, 26(4):46–58, 2019.